

Winter 2014

Plasmon-Enhanced Raman and Fluorescence Spectroscopy with Gold and Silver Nanoparticles

Ariel Rodrigo Guerrero Hernandez
University of Windsor

Follow this and additional works at: <http://scholar.uwindsor.ca/etd>

 Part of the [Chemistry Commons](#)

Recommended Citation

Guerrero Hernandez, Ariel Rodrigo, "Plasmon-Enhanced Raman and Fluorescence Spectroscopy with Gold and Silver Nanoparticles" (2014). *Electronic Theses and Dissertations*. Paper 5026.

This online database contains the full-text of PhD dissertations and Masters' theses of University of Windsor students from 1954 forward. These documents are made available for personal study and research purposes only, in accordance with the Canadian Copyright Act and the Creative Commons license—CC BY-NC-ND (Attribution, Non-Commercial, No Derivative Works). Under this license, works must always be attributed to the copyright holder (original author), cannot be used for any commercial purposes, and may not be altered. Any other use would require the permission of the copyright holder. Students may inquire about withdrawing their dissertation and/or thesis from this database. For additional inquiries, please contact the repository administrator via email (scholarship@uwindsor.ca) or by telephone at 519-253-3000ext. 3208.

**Plasmon-Enhanced Raman and Fluorescence
Spectroscopy with Gold and Silver
Nanoparticles**

by

Ariel Rodrigo Guerrero Hernández

A Dissertation

submitted to the Faculty of Graduate Studies
through Chemistry and Biochemistry
in partial fulfillment of the requirements for the
degree of Doctor of Philosophy
at the University of Windsor

Windsor, Ontario, Canada

2013

© 2013 Ariel R. Guerrero H.

Plasmon-Enhanced Raman and Fluorescence Spectroscopy with Gold and Silver Nanoparticles

by

Ariel Guerrero

APPROVED BY:

P. Mc Breen, External Examiner
University of Laval

D. Northwood
Mechanical, Automotive & Materials Engineering

J. Wang
Department of Chemistry & Biochemistry

J. Gauld
Department of Chemistry & Biochemistry

R. Aroca, Advisor
Department of Chemistry & Biochemistry

October 11, 2013.

Declaration of Co-Authorship/Previous Publication

I. Declaration of Co-Authorship.

I hereby declare that this thesis incorporates material that is the result of joint research, as follows:

- Chapter 5 incorporates the outcome of joint research efforts undertaken in collaboration with Haider Mohan, Geok Yi Teo, Pablo Albella and Fernando Moreno. Geok Yi Teo and Haider Mohan provided the experimental research with spherical nanoparticles, based on my own previous work described in Chapter 4. Pablo Albella and Fernando Moreno (Universidad de Cantabria, Spain) provided the theoretical calculations to support the experimental data. I performed the experiments with silica-coated gold nanorods showing spectral profile modification.
- Chapter 6 incorporates research performed in close collaboration with Yun Zhang, where she performed part of the wet chemistry experiments leading to the synthesis of the nanostructures.

I am aware of the University of Windsor Senate Policy on Authorship and I certify that I have properly acknowledged the contribution of other researchers to my thesis, and have obtained written permission from each of the co-authors to include the above materials in my thesis.

I certify that, with the above qualification, this thesis, and the research to which it refers, is the product of my own work.

II. Declaration of Previous Publication.

This thesis includes 4 original papers that have been either published or submitted for publication in peer-reviewed journals:

Ch.	Title	Status
3	Surface-Enhanced Raman Scattering of Hydroxyproline. Guerrero, A. R.; Aroca, R. F. <i>J. Raman Spectrosc.</i> 2012 , <i>43</i> , 478.	Published
4	Surface-Enhanced Fluorescence with Shell-Isolated Nanoparticles (SHINEF). Guerrero, A. R.; Aroca, R. F. <i>Angew. Chem. Int. Edit.</i> 2011 , <i>50</i> , 665.	Published

5	Plasmon-Enhanced Fluorescence and Spectral Modification in SHINEF. Aroca, R. F.; Teo, G. Y.; Mohan, H.; Guerrero, A. R.; Albella, P.; Moreno, F. J. <i>Phys. Chem. C</i> 2011 , <i>115</i> , 20419.	Published
6	Experimental Confirmation of Local Field Enhancement Determining Far Field Measurements with Shell-Isolated Silver Nanoparticles. Guerrero, A. R.; Zhang, Y.; Aroca, R. F. <i>Small</i> 2012 , <i>8</i> , 2964.	Published

I certify that I have obtained a written permission from the copyright owners to include the above published material in my thesis.* I certify that the above material describes work completed during my registration as a graduate student at the University of Windsor.

I declare that, to the best of my knowledge, my thesis does not infringe upon anyone's copyright nor violate any proprietary rights, and that any ideas, techniques, quotations, or any other material from the work of other people included in my thesis, published or otherwise, are fully acknowledged in accordance with the standard referencing practices. Furthermore, to the extent that I have included copyrighted material that surpasses the bounds of fair dealing within the meaning of the Canada Copyright Act, I certify that I have obtained a written permission from the copyright owners to include such materials in my thesis.

I declare that this is a true copy of my thesis, including any final revisions, as approved by my thesis committee and the Graduate Studies Office, and that this thesis has not been submitted for a higher degree to any other university or institution.

* The full text of these permissions is included in the *Permissions Obtained for Published Copyrighted Materials* section, page 154.

Abstract

This thesis contains five major contributions to the field of plasmon-enhanced spectroscopy. We start with the report of a unique SERS study of the amino acid hydroxyproline and a deuterated analogue. Later, we move on to the exploration of a major new research path known as *shell-isolated nanoparticle-enhanced fluorescence* (SHINEF), consisting in the application of silica-shelled noble metal nanoparticles to achieve surface-enhanced fluorescence. The proof of concept of this technique is explained in one chapter. The two following chapters are devoted to the exploration of the plasmonic properties of SHINEF: spectral profile modification showing the close relationship between the observed enhanced fluorescence and the nanoparticle scattering. The SHIN particles are employed to experimentally prove the relationship between the SEF and SERS enhancement factors, theoretically predicted before, but never verified experimentally until now. The thesis ends with an investigation, in aqueous solutions, of several different factors that play a role in the origin of SEF, showing greater enhancement for SHINEF after inducing nanoparticle aggregation.

*To my mother
Rosa H. Hernández González
and to the memory of my father,
Luis Roberto Guerrero Quero
(R.I.P. October 31, 2012)*

Acknowledgements

First, I express my gratitude to my supervisor, Professor Dr. Ricardo Aroca. From him I have learnt many things about science that are detailed in the rest of this volume, but I have also learnt values from him and from his wife Mrs. Patricia, and received great affection. I consider myself privileged to have received the invitation to work at Dr. Aroca's group and contribute my efforts to the knowledge base of mankind.

I also express my gratitude to past and present members of the Materials and Surface Science Group, including the "old guard": Nicholas Pieczonka, Daniel Ross, Golam Moula, Paul Goulet and Igor Osorio, and the "new guard": Haider Mohan, Aisha Alsaleh, and special thanks to Yun Zhang ("Kate") and her husband Xiaodong Zhang ("Jack") for their help especially in the most difficult moments. Also to the people who stayed temporarily with us: Anna Maeva, Adam Skarbek, Artur Jarosz, Joel Almasi, Teo Geok Yi, Stefan Zalanca, Wenhao Chen ("Andrew") and the international visitors that enriched my life: José Cárcamo, Pedro Aoki, Elena del Puerto, María Rosa López, Flávio Cabrera, Rosana Resende, Diogo Volpati, Gabriel Espírito Santo and Felipe Bellucci.

I have also to thank Pablo Encina and Mirtha Osorio, my "compadres", who have offered me their corner of my homeland here in Canada, and their help when I needed it most. Also to Ernesto Clavijo, and also to María Eugenia and Garr Winters for their help in my early days in Windsor, and to my friend Yassine Beldjoudi with whom I shared many an interesting conversation.

Thanks also to the staff in the Department of Chemistry and Biochemistry, especially Marlene Bezaire (thank you times a thousand!), Catherine Wilson, Beth Kickham and Una Lee, and also to Sharon Lackie from the GLIER institute.

Thanks also to my committee members, Drs. Jichang Wang, James Gauld, Derek Northwood and Peter McBreen for reading and correcting my thesis.

Finally, and most deep-heartedly, I have to thank my mother Rosa Hernández and to my father Luis Roberto Guerrero, and also to my closest family, especially my uncle Jorge and his wife, and to my aunts and cousin for their daily and continuous support, especially

when I needed it the most. Daddy, you had to leave us while I was working on this Ph.D. thesis but you'll never go away from our hearts. I'm pretty sure you're proud like you've always been, aren't you?

Thank you very much

Muchas gracias

Muito obrigado

Merci beaucoup

شكرا جزيلا

非常感謝

God bless you all



Table of Contents

Declaration of Co-Authorship/Previous Publication	iii
Abstract	v
Dedication.....	vi
Acknowledgements.....	vii
List of Tables	xiii
List of Figures.....	xiv
List of Abbreviations.....	xviii
1. Theoretical Background of Plasmon-Enhanced Raman and Fluorescence	1
1.1. Fluorescence Spectroscopy.....	1
1.1.1. History and Definition.....	1
1.1.2. Fluorescence Spectra	3
1.1.3. Quantum Yield and Lifetime	4
1.2. Raman Spectroscopy	5
1.2.1. Molecular Vibrations	5
1.2.2. Raman Scattering	8
1.2.3. Raman Spectra	11
1.2.4. Resonance Raman Scattering.....	12
1.3. Nanoparticles	14
1.4. Plasmons	16
1.5. Surface-Enhanced Raman Scattering.....	20
1.5.1. SERS Theory	20
1.5.2. Interpretation of SERS spectra	24
1.5.3. SERRS and Single-Molecule Detection.....	25
1.6. Surface-Enhanced Fluorescence.....	26
1.6.1. Theoretical Model.....	27
1.7. References	29
2. Experimental Methods and Instrumentation.....	33

2.1. Colloidal Wet Chemistry Methods.....	33
2.1.1. Synthesis of Gold Nanospheres	33
2.1.2. Synthesis of Silver Nanospheres	34
2.1.3. Nanoparticles with different shapes.....	35
2.1.4. Coating with Silica.....	36
2.1.5. Other experimental details	38
2.2. Electron Microscopy.....	38
2.2.1. Transmission Electron Microscopy	39
2.2.2. Scanning Electron Microscopy.....	40
2.3. Atomic Force Microscopy.....	43
2.4. Langmuir-Blodgett Filmmaking.....	46
2.4.1. Theory	46
2.4.2. Mixed LB films.....	48
2.5. Spectroscopy Instrumentation	50
2.5.1. Raman and Fluorescence Microscope.....	50
2.5.2. Lasers.....	51
2.5.3. UV-visible Absorption Spectrometer	52
2.6. Computational Resources	52
2.6.1. Computational Chemistry	52
2.6.2. Other Software	54
2.7. References	54
3. Surface-Enhanced Raman Scattering of Hydroxyproline.....	57
3.1. Introduction	57
3.2. Materials and Methods	59
3.3. Results and Discussion	60
3.4. Conclusions	76
3.5. References	76
4. Surface-Enhanced Fluorescence with Shell-Isolated Nanoparticles: SHINEF.....	78
4.1. Introduction	78

4.2. Materials and Methods	80
4.2.1. SHIN Particle Synthesis	80
4.2.2. Electron Microscopy	80
4.2.3. LB Filmmaking	81
4.2.4. Spectroscopic measurements	81
4.3. Results and Discussion	82
4.4. Conclusions	90
4.5. References	90
5. Plasmon-Enhanced Fluorescence and Spectral Modification in SHINEF	92
5.1. Introduction	92
5.2. Materials and Methods	93
5.3. Results and Discussion	96
5.3.1. Spherical Particles: Effect of the Core and Shell Sizes	97
5.3.2. Nanorods and Spectral Profile Modification	102
5.4. Conclusions	106
5.5. References	106
6. Plasmon Enhanced Raman-Fluorescence Ratio with Shell-Isolated Silver Nanoparticles	
.....	108
6.1. Introduction	108
6.2. Materials and Methods	110
6.3. Results and Discussion	112
6.3.1. Ag-SHINs	112
6.3.2. Local field enhancement in SHINERS and SHINEF	115
6.4. Conclusions	121
6.5. References	121
7. Exploring the Origin of the Observed SEF: A Study in Aqueous Solutions	123
7.1. Introduction	123
7.1.1. Properties of the Fluorophore	124
7.1.2. Role of the nanostructure	127

7.2. Materials and Methods	128
7.3. Results and Discussion	130
7.3.1. Characterization of the SHINs and absorption of MG and CV.....	130
7.3.2. Local field SERS/SEF relationship	131
7.3.3. Excitation power	135
7.3.4. Quantum Yield and Absorption Enhancement	135
7.3.5. High Quantum Yield Dyes.....	140
7.3.6. Enhancement by Nanoparticle Aggregates.....	142
7.4. Conclusions	146
7.5. References	146
8. Concluding Remarks.....	151
References.....	152
Permissions Obtained for Published Copyrighted Materials.....	154
Vita Auctoris.....	161
List of Publications	161
Awards.....	163

List of Tables

Table 1.1. Typical cross-sections of processes for various possible interactions of molecules with incident electromagnetic radiation	7
Table 1.2. Dielectric function values for silver and gold	19
Table 2.1. Probe molecule to fatty acid ratio with the approximate number of molecules	49
Table 2.2. List of lasers and their wavelength and power	52
Table 3.1. Band assignment for the normal, non-protonated Raman spectra.	64
Table 3.2. Assignment for the SERS spectra of Hyp	66
Table 3.3. Assignment for the spectra of d-Hyp in solid and solution	70
Table 3.4. Assignment for the spectra of d-Hyp in solid and solution	74
Table 6.1. Calculations for different repetitions of the SHINERS/SHINEF experiment.	117
Table 7.1. SHINERS and SHINEF enhancement factors and local field calculations for CV. LL=514.5 nm.....	132
Table 7.2. SHINERS and SHINEF enhancement factors and local field calculations for MG. LL=514.5 nm.....	133
Table 7.3. SHINERS and SHINEF enhancement factors and local field calculations for MG. LL=632.8 nm.....	134
Table 7.4. SHINEF EF as a function of the amount of SHINs added and excitation power.	135
Table 7.5. CV SHINEF EF, quantum yields and QY enhancement factors with increasing amounts of SHINs added.....	138
Table 7.6. MG SEF EF, quantum yields and QY EFs with increasing amounts of SHINs added.	140
Table 7.7. Enhancement factors for CV with 100 μ L of SHINs and increasing concentrations of NaCl.....	143

List of Figures

Figure 1.1. Jablonski diagram for fluorescence.....	2
Figure 1.2. Fluorescence spectrum of octabutoxyphthalocyanine.....	3
Figure 1.3. Potential energy diagram for a molecular vibration.	6
Figure 1.4. Jablonski diagram for Raman scattering processes.....	11
Figure 1.5. Complete Raman spectrum of carbon tetrachloride.	12
Figure 1.6. SEM image of nanoparticles of different shapes and sizes.....	15
Figure 1.7. Plasmon absorption of silver and gold colloids.	17
Figure 1.8. Simple diagram illustrating SERS.	22
Figure 1.9. The theoretical distance dependence in SEF.....	29
Figure 2.1. Citrate-reduced gold colloid.....	34
Figure 2.2. Silica-coated gold nanorods, coated using the Stöber method.	37
Figure 2.3. FEI Titan 800B transmission electron microscope.	40
Figure 2.4. FEI Quanta 200 Environmental scanning electron microscope.....	42
Figure 2.5. Nanoscope IV scanning probe microscope.....	45
Figure 2.6. Surface pressure-area isotherm for arachidic acid	46
Figure 2.7. Z-deposition to a glass slide.....	47
Figure 2.8. Nima 302M LB film balance.....	49
Figure 2.9. Renishaw inVia Raman microscope	50
Figure 2.10. Varian Cary 50 UV-vis spectrometer.....	53
Figure 3.1. Absorption spectrum and AFM image of the particles.	60
Figure 3.2. Optimized conformations for Hyp.....	61
Figure 3.3. Calculated and experimental Raman spectra for Hyp.	62
Figure 3.4. Calculated and experimental SERS spectra.	63
Figure 3.5. Optimized conformation for Hyp with one Au ⁺ ion.....	63
Figure 3.6. Optimized conformations for d-Hyp.....	69
Figure 3.7. Calculated and experimental Raman spectra for d-Hyp.....	69
Figure 3.8. Additional calculations for d-Hyp compared to experiment.	72

Figure 3.9. SERS spectra of d-Hyp.....	73
Figure 4.1. Absorption spectra of the SHINs' plasmon, R18 and nBPTCD dyes, and SEM and TEM images of the SHINs.	82
Figure 4.2. Reference fluorescence spectra of R18 and nBPTCD in solution and of one LB monolayer on glass.....	83
Figure 4.3. Reference fluorescence and SHINEF of a mixed LB monolayer (1:10) of nBPTCD and arachidic acid.....	84
Figure 4.4. Surface enhanced fluorescence of the R18 LB monolayer with "smart dust" nanoparticles	84
Figure 4.5. Reference fluorescence and SHINEF of a mixed LB monolayer (1:1000) of nBPTCD and arachidic acid.....	85
Figure 4.6. Fluorescence of the neat LB monolayer on quartz and subsequent addition of naked gold nanoparticles.	87
Figure 4.7. SEF of the R18 LB monolayer with SHIN nanoparticles with thinner shell.	87
Figure 4.8. SEM images of the SHIN particles used for most of the results of the <i>Angewandte Chemie</i> paper (codenamed "code B"). Images taken 3 years after they were synthesized and used for the results of the paper.....	88
Figure 4.9. Absorption spectrum of the SHIN particles in 2013.....	89
Figure 4.10. Quick (up to 700 nm only) test spectra with a R18:AA 1:10 LB film with the aged particles.....	89
Figure 5.1. Characterization of the sphere-like Au SHINs to study the effect of the core size.	98
Figure 5.2. SEM image of the large SHINs.	99
Figure 5.3. SHINEF from small core gold SHINs with different shell thickness.....	99
Figure 5.4. SHINEF from large core gold SHINs with different shell thickness.....	100
Figure 5.5. Calculated near field enhancement of small and large SHINs at 515 nm excitation and far field scattering of the small and large SHIN particles.	101

Figure 5.6. Fluorescence spectrum of the Cl-PTCD solution (monomer) and fluorescence from the Cl-PTCD mixed LB showing the monomer and excimer components of the emission.	102
Figure 5.7. TEM of SHINs particles with absorption at 531 nm and SHIN nanorods with plasmon absorption at 685 nm. Scale bars represent 100 nm.	103
Figure 5.8. Spectral profile modification in SHINEF with shelled nanospheres and nanorods.	104
Figure 5.9 All spectra in the map with spherical AuSHINs on a Cl-PTCD:AA 1:10 LB film.	105
Figure 5.10. All spectra in the mapping with AuSHIN nanorods on a Cl-PTCD:AA 1:10 LB film.	105
Figure 6.1. Characterization of the SHIN particles and the dyes employed.	112
Figure 6.2. SHINEF of a R18:arachidic acid 1:10 mixed LB film using our silver SHINs, showing the maximum EF of 94.....	113
Figure 6.3. Combined SHINERS and SHINEF spectra for an aqueous solution of CV, and comparison with normal Raman and fluorescence spectra.	114
Figure 6.4. Repetition of the LB test for SHINEF with a mixed R18:AA LB film.	115
Figure 6.5. Comparison of the experimental CV SHINERS spectrum with a calculated spectrum for CV.	116
Figure 6.6. Theoretical fits and EF calculations for both SHINERS and SHINEF.....	117
Figure 6.7. SHINERS and SHINEF spectra for a mix of SHINs and CV solution cast over a quartz slide.....	118
Figure 6.8. Spectra taken with uncoated Ag colloids.....	119
Figure 6.9. SHINEF of a LB film of nBPTCD:AA 1:10 with the new Ag-SHINs.....	120
Figure 6.10. SHINEF of CV in aqueous solution with Au SHINs.	120
Figure 7.1. Number of results of plasmon-enhanced luminescence, separated by keyword.	123
Figure 7.2. Characterization of the Ag SHINs and the CV and MG dyes.	131
Figure 7.3. SHINEF of CV in solution with increasing amounts of SHINs, using the 514.5 nm laser line.	132

Figure 7.4. SHINEF of MG in solution with increasing amounts of SHINs, using the 514.5 nm laser line.	133
Figure 7.5. SHINEF of MG in solution with increasing amounts of SHINs, using the 632.8 nm laser line.	134
Figure 7.6. Extinction spectra of CV 6×10^{-6} M with SHINs added, to study the effect of quantum yield.	136
Figure 7.7. Extinction spectra of CV 6×10^{-6} M with 20 and 40 μ L of SHINs added, after subtraction of the SHINs.	137
Figure 7.8. Fluorescence spectra of CV 6×10^{-6} M measuring quantum yield.	137
Figure 7.9. Extinction spectra of MG with SHINs added, to study the effect of quantum yield	139
Figure 7.10. Extinction spectra of MG 2×10^{-5} M with 20 and 40 μ L of SHINs added, after subtraction of the SHINs.	139
Figure 7.11. Fluorescence spectra of MG 2×10^{-5} M measuring quantum yield.	140
Figure 7.12. Fluorescence of Pyronin Y with increasing SHINs added.	141
Figure 7.13. Fluorescence of Sulforhodamine B with increasing APTES-Ag SHINs added.	141
Figure 7.14. Extinction spectra for CV with 100 μ L of SHINs and increasing concentrations of NaCl.....	142
Figure 7.15. Fluorescence spectra for CV with 100 μ L of SHINs and increasing concentrations of NaCl.....	143
Figure 7.16. Extinction spectra for MG with 50 μ L of SHINs and NaCl 0.01 M	144
Figure 7.17. Fluorescence spectra for MG with 50 μ L of SHINs and NaCl 0.01 M, with the 514.5 nm laser line.	145
Figure 7.18. Fluorescence spectra for MG with 50 μ L of SHINs and NaCl 0.01 M, with the 632.8 nm laser line.	145

List of Abbreviations

AFM	Atomic Force Microscope (also <i>microscopy</i>)
APTMS	3-aminopropyltrimethoxysilane
CCD	Charge-Coupled Device
Cl-PTCD	Bis(3,4-dichlorobenzyl tetracarboxydiimido) perylene
CTAB	Cetyltrimethylammonium bromide
CV	Crystal Violet
DDA	Discrete Dipole Approximation
DLVO	Derjaguin, Landau, Verwey and Overbeek (theory)
d-Hyp	Deuterated analogue of 4-hydroxyproline (trans-4-hydroxyproline-2,5,5-d ₃)
EF	Enhancement Factor
EM	Electromagnetic
FDTD	Finite Difference Time Domain
FWHM	Full Width at Half Maximum
Hyp	4-Hydroxyproline
IR	Infrared
LB	Langmuir-Blodgett
LL	Laser line
LSPR	Localized Surface Plasmon Resonance
MG	Malachite Green
nBPTCD	Bis- <i>n</i> -butyl perylene tetracarboxydiimide, also called bis- <i>n</i> -butylimido perylene
R18	Octadecyl Rhodamine B
RRS	Resonance Raman Scattering
SEF	Surface-Enhanced Fluorescence
SEM	Scanning Electron Microscope (also <i>microscopy</i>)

SERS	Surface-Enhanced Raman Scattering
SERRS	Surface-Enhanced Resonance Raman Scattering
SHIN	Shell-Isolated Nanoparticle
SHINEF	Shell-Isolated Nanoparticle-Enhanced Fluorescence
SHINERS	Shell-Isolated Nanoparticle-Enhanced Raman Scattering
SMD	Single-Molecule Detection
SPM	Spectral Profile Modification
TEM	Transmission Electron Microscope (also <i>microscopy</i>)
TEOS	Tetraethylorthosilicate

Chapter One

Theoretical Background of Plasmon-Enhanced Raman and Fluorescence

1.1. Fluorescence Spectroscopy

Fluorescence spectroscopy is a widely employed technique for chemical analysis, because of its inherent high sensitivity, and its large linear concentration ranges, often significantly larger than in absorption methods, but the latter find more applicability as relatively few species exhibit fluorescence.^[1,2]

1.1.1. History and Definition.

Fluorescence was first observed by the Spanish botanist Nicolás Monardes in 1565,^[3] in his infusions of a Mexican plant, but a correct interpretation was not provided. No new investigations were made until the nineteenth century, when Edward D. Clark in 1819 and later René Juste Haüy in 1823 described fluorescence in the mineral called fluorite. Later Sir David Brewster described it for chlorophyll in 1833 and Sir John Herschel for quinine in 1845, but it was the English physicist Sir George Gabriel Stokes in 1852 who coined the term *fluorescence*, in his paper “On the Change of Refrangibility of Light”.^[4]

Fluorescence is the main variant in a group of phenomena called *photoluminescence*, grouping fluorescence and phosphorescence. Fluorescence happens in two stages: first, a photon must be *absorbed* by a *fluorophore* (the species that fluoresces; it is usually a molecule, although it can also be an atom and a nanostructure) and it must be of energy equal or higher to that of an electronic excitation. The molecule is excited from a ground state S_0 to an excited state S_2 or S_1 . Here the S represents *singlet* states; $h\nu$ is the generic expression for a photon; h is Planck’s constant and ν is the photon’s frequency.

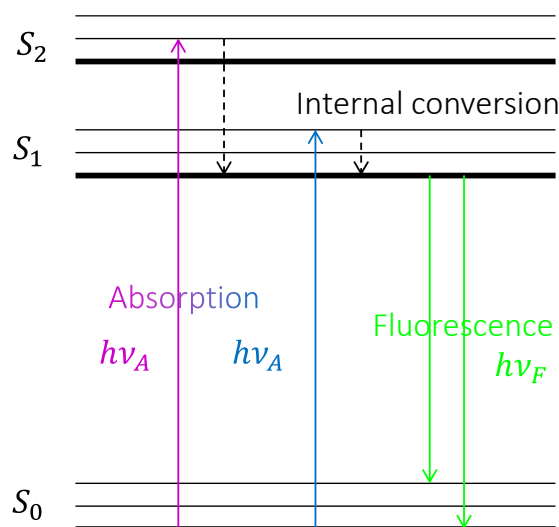


Figure 1.1. Jablonski diagram for fluorescence.

Second, the fluorophore is said to relax, generally to the lowest vibrational level of S_1 ; this is called *internal conversion*, and then the fluorophore emits a photon liberating energy as heat in the process so it goes back to the ground state S_0 . This is illustrated in the so-called Jablonski diagram, like that shown in Figure 1.1. Not shown in the picture above is when the system goes from the state S_1 to a triplet state T in a process called *intersystem crossing*; this leads to the delayed emission called *phosphorescence*, which will not be discussed here.

The emitted photon always has less energy than the absorbed, therefore it has a longer wavelength, and this change in energy is termed *Stokes shift*. The so-called Stokes and anti-Stokes in Raman are named after their corresponding fluorescence analogue.

Not all molecules do fluoresce; the phenomenon is restricted to the molecules that can: 1) absorb light at the excitation wavelength 2) relax by emitting a photon. This last condition is successfully met by molecules with a rigid structure like those with aromatic rings. This usually gives rise to transitions of the type $\pi \rightarrow \pi^*$ or $n \rightarrow \pi^*$. In theory it should be possible to achieve fluorescence with a $\sigma \rightarrow \sigma^*$ which would require wavelengths of less than 250 nm, but in practice the energy required for such transitions matches that necessary to produce bond ruptures and these processes happen before fluorescence can take place; therefore fluorescence is in practice restricted to the former type of transitions.

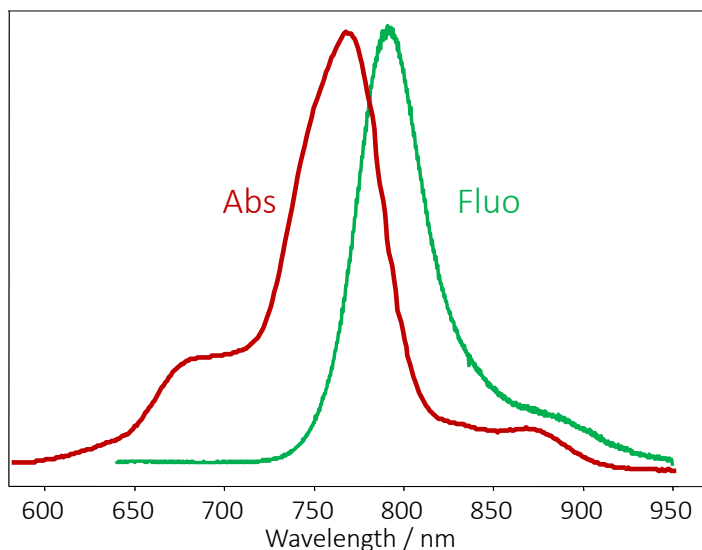


Figure 1.2. Fluorescence spectrum of octabutoxyphthalocyanine. The spectrum shows the mirror-image rule.

1.1.2. Fluorescence Spectra

Fluorescence spectra are always represented as a graph of emission intensity versus wavelength, usually in nanometres but sometimes expressed in absolute wavenumbers.

A characteristic of fluorescence is that the fluorescence emission is independent of the excitation wavelength. It is only required that the excitation light has enough energy to achieve the excited states, but with higher energies the emission spectrum remains the same. This is because upon relaxation, all excess energy is dissipated rapidly leaving the fluorophore in the lowest vibrational state of S_1 and the emission and relaxation proceeds from that state only; this is called *Kasha's rule*.

Also, it is experimentally observed that most molecules that do fluoresce follow the so-called mirror image rule: the emission spectrum is a mirror image of the absorption spectrum (Figure 1.2). This is because when the molecule relaxes and emits, it does not return to the lowest energy state, but to some excited vibrational ground state. Exceptions to the mirror-image rule are molecules like quinine, that show one less peak than that of its absorption spectrum. This is because in the absorption spectrum there is the second excited state S_2 , which at the moment of emission quickly relaxes back to the state S_1 . Then the emission spectrum is a mirror image of the S_0 - S_1 transition only.

There are also molecules like pyrene and perylene, which have a planar structure that allows for easy interaction between the pi electron clouds in the molecule, allowing for the formation of complexes of the molecule that emits at a longer wavelength, however this complex only exists in the excited state. If this excited state complex is with a different molecule, the complex is called an *exciplex*; but the complex can also be formed among two identical molecules; the resulting excited state dimer is termed an *excimer*. The fluorescence coming out of these excited state complexes lacks all the peak structure of the monomers; it becomes a very broad peak very much redshifted in comparison to the fluorescence of the monomer. An example of that can be seen in the experiments with the excimer-showing perylene derivatives described in Chapters 4 and 6.

1.1.3. Quantum Yield and Lifetime

A measure of the efficiency of photophysical processes, fluorescence among them, is the **quantum yield** or quantum efficiency (Φ), which is defined as:

$$\Phi = \frac{\text{number of photons emitted}}{\text{number of photons absorbed}} \quad (1.1)$$

It is equivalent to the ratio of the molecules that fluoresce to the total number of excited molecules. Molecules or systems that are highly fluorescent have a quantum yield approaching unity, while those that don't fluoresce appreciably have a quantum yield approaching zero.

The interval of time between the absorption of a photon and the emission of another is called the fluorescence **lifetime** (τ), and it represents for how long the molecule upholds the excited state. Typical fluorescence lifetime values are around 10^{-8} s.

Lifetime and quantum yields are related to each other. We have to consider the following relationship:

$$\Phi = \frac{\Gamma}{\Gamma + k_{nr}} \quad (1.2)$$

where Γ is the emissive rate of the fluorophore and k_{nr} is the nonradiative decay rate to S_0 . The latter accounts for the dissipation of energy to processes other than fluorescence, hence the name nonradiative. When k_{nr} is small, the quantum yield is high, and can be close to unity.

The lifetime in the absence of non-radiative processes, or intrinsic lifetime, can be expressed as:

$$\tau_n = \frac{1}{\Gamma} \quad (1.3)$$

When there are non-radiative processes included, this equation is converted to:

$$\tau = \frac{1}{\Gamma + k_{nr}} \quad (1.4)$$

Fluorescence is a random process and few molecules emit at precisely τ ; this value represents an average of the time spent in the excited state by a group of molecules.

Also, fluorescence intensity can decrease by a variety of processes, which together they are called **fluorescence quenching**. The mechanisms through which quenching can occur are many; among the most notable are collisions with other molecules in gas phase or in solution, in which case the fluorophore returns to the ground state due to energy transfer. Metals, including metallic particles, have a lot of electrons in their surface and are an example of good fluorescence quenchers.^[5] This is an important factor to take into account at the moment of discussing surface-enhanced fluorescence later.

1.2. Raman Spectroscopy

Like infrared (IR) absorption spectroscopy, Raman^[6] allows for the identification of the vibrations in a molecule, and can be said to be complementary to infrared, but it can be more expensive and less sensitive when not enhanced.^[4] Before we describe the plasmon enhancement causing the SERS effect, it is necessary to study the fundamentals of Raman spectroscopy.

1.2.1. Molecular Vibrations

When light interacts with matter, several things can happen: light can be reflected, absorbed or scattered. In the case when it is absorbed, photons are absorbed according to characteristic frequencies within the molecule. Classically, the way to describe the behaviour of chemical bonding between two atoms has been the *harmonic oscillator*; hence this approximation is then termed *harmonic approximation*. According to this,

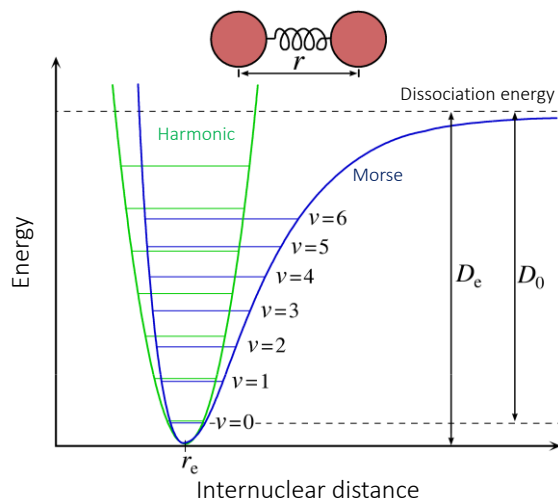


Figure 1.3. Potential energy diagram for a molecular vibration. The green curve represents the harmonic potential and the blue curve is the Morse potential.

atomic nuclei are modelled as balls united by springs undergoing simple harmonic motion, the springs representing the chemical bonds between the atoms in a molecule.^[7]

Under these premises, if there are N atoms in a molecule, and the molecule is treated as a whole, the said molecule must have $3N - 6$ degrees of freedom if the molecule is not linear, and $3N - 5$ if it is. Then every degree of freedom is set in correspondence with the so called normal modes of vibration, and they correspond to motions where all the nuclei undergo harmonic motion, move in phase and have the same frequency of oscillation.^[7] Differentiating the energy of a given bond, we can know the force F of the bond, and this bond is treated as a spring:

$$F = -k(R - R_{eq}) \quad (1.5)$$

where k is the “spring” constant (from now on, the *force constant of the bond*), R is the distance between the two atoms and R_{eq} is the equilibrium position for the vibration. Then the vibrational frequency (ν) is given by:

$$\nu = \frac{1}{2\pi} \sqrt{\frac{k}{\mu}} \quad (1.6)$$

where μ is the reduced mass of the two atoms of masses m_1 and m_2 ; it is defined as $\mu = \frac{m_1 m_2}{m_1 + m_2}$.

Equation (1.6) provides a rather rough but still useful estimate of the vibrational frequency; deviations to the harmonic behaviour are termed *anharmonicity*. A more accurate potential is the Morse potential, which is shown in comparison with the harmonic potential in Figure 1.3.

The vibrations in a molecule give origin to the two major forms of vibrational spectroscopy: infrared absorption and Raman scattering spectroscopy. Both techniques take advantage of the same vibrations, but they appeal to phenomena having different physical origin.

IR absorption will be mentioned here only briefly. In the case of IR absorption, this phenomenon occurs when a photon has a wavelength that matches that of the vibration of the molecule. When reaching the molecule, the photon is then absorbed and it induces a change in the *dipole moment* of the molecule. Molecular vibrations typically have absorption frequencies into the so-called mid-infrared part of the electromagnetic (EM) spectrum (200-4000 cm^{-1}), hence the name. A plot of absorption vs. wavelength gives the IR spectrum for a molecule, which is unique for every molecule; it is then its *fingerprint*, and for that reason it constitutes a classical way to identify molecules, giving rise to the field of IR spectroscopy, which is one of the most common ways to identify molecules, in organic and inorganic chemistry.^[8,9]

Process	Cross section of...	σ (cm^2) ^[10]
Absorption	Ultraviolet/visible	10^{-18}
Absorption	Infrared	10^{-20}
Emission	Fluorescence	10^{-19}
Scattering	Rayleigh scattering	10^{-26}
Scattering	Raman scattering	10^{-29}
Scattering	Resonance Raman	10^{-24}
Scattering	SERRS	10^{-17}
Scattering	SERS	10^{-19}

Table 1.1. Typical cross-sections of processes for various possible interactions of molecules with incident electromagnetic radiation

A typical way of measuring the efficiency of an optical process such as IR or Raman is the **cross section** (σ), which gives an idea of the probability for an event to occur; the higher

this value, the more efficient the process is. The theoretical concept of cross section comes from macroscopic objects and it refers to their literal cross section, which indicates how likely they are to be hit by a projectile. In a spectroscopy context, molecules and atoms are hit by photons, and while it is complicated to calculate exact cross sections for quantum objects like molecules, the concept remains useful. Typical cross sections for the most common optical processes are given in Table 1.1.

1.2.2. Raman Scattering

Having investigated scattered light since the early 1920s, in February 1928, Prof. Sir Chandrasekhara Venkata Raman in collaboration with his then-graduate student Kariamanickam Srinivasa Krishnan in Calcutta, India, published one of the most relevant findings in physics: the discovery of a new type of scattered radiation.^[11,12] This radiation had been previously predicted theoretically by Adolf Smekal in 1923^[13] and it was also reported experimentally two months after Raman, independently, by the Russian scientists Grigori Landsberg and Leonid Mandelstam in crystals.^[14] However, it was Raman's work that got better known, and after scientists in Germany were able to reproduce Raman's findings, they started calling the phenomenon as the *Raman effect*, and for his work Raman received the Nobel Prize in Physics in 1930. A comprehensive account of the discovery is given by Rajinder Singh.^[15]

Raman scattering is defined as the **inelastic scattering** of light. As said at the beginning of section 1.2.1, radiation can be reflected, absorbed or scattered. From the fraction of photons that are scattered, most of them are scattered without loss of energy; such phenomenon is called elastic scattering, or Rayleigh scattering. But a small fraction of those scattered photons undergo an *energy change* that is *equal to a vibrational quantum transition*, i.e. the same energy that gives rise to IR absorption, those photons constitute the Raman scattering. The probability for the generation of a Raman-scattered photon is about 1 for every 10^7 photons scattered by the molecule. This means that the process is very inefficient and this can be verified by the low cross-section assigned to normal Raman scattering in several orders of magnitude lower than fluorescence or absorption.

Raman scattering can have either more energy than the original light, or less energy. The latter case is much more likely, and since it matches the Stokes shift of fluorescence, is termed *Stokes Raman scattering*, and the former case is the *anti-Stokes Raman scattering*.

Raman scattering was initially described in terms of classical physics and was later further refined with a quantum-mechanical description. In this thesis we will describe only the classical treatment. Both treatments are based upon a property that describes its molecular response. That property is called **polarizability**, it is represented by the Greek letter alpha (α) and it is always modelled in terms of the induced polarization (p) that results of the interaction with an electric field E :

$$p = \alpha E \quad (1.7)$$

The polarizability is a description of the electron cloud that surrounds a molecule and essentially describes its deformability in the presence of an electric field. If the electric field, oscillating at a frequency ν_0 , is given by $E = E_0 \cos 2\pi\nu_0 t$, or if we consider the angular frequency $\omega = 2\pi\nu$, then $E = E_0 \cos \omega t$, the induced dipole will be:

$$p = \alpha E_0 \cos \omega_0 t \quad (1.8)$$

At any one time the molecule is in a complex motion of vibrations which are approximated as the summation of normal vibrations. The polarizability is a function of the normal coordinate $Q = Q_0 \cos \omega_j t$, where ω_j is the frequency of the j -th vibration. That way the polarizability can be expanded as a Taylor series:

$$\alpha = \alpha_0 + \left(\frac{\partial\alpha}{\partial Q}\right)_0 Q + \frac{1}{2} \left(\frac{\partial^2\alpha}{\partial Q^2}\right)_0 Q^2 + \dots$$

Neglecting the contributions of second order terms and higher, and after replacing $Q = Q_0 \cos \omega_j t$ as defined, the polarizability function looks like:

$$\alpha = \alpha_0 + \left(\frac{\partial\alpha}{\partial Q}\right)_0 Q_0 \cos \omega_j t \quad (1.9)$$

Then, substituting (1.9) in (1.8), the induced dipole moment p becomes:

$$p = \alpha_0 E_0 Q_0 \cos \omega_0 t + \left(\frac{\partial\alpha}{\partial Q}\right)_0 E_0 Q_0 \cos \omega_j t \cos \omega_0 t \quad (1.10)$$

Finally, applying the trigonometric identity $\cos \alpha \cos \beta = \frac{1}{2} [\cos(\alpha + \beta) + \cos(\alpha - \beta)]$ and rearranging, the equation above can be expressed as:

$$\begin{aligned}
 p = \alpha_0 E_0 \cos \omega_0 t + \frac{1}{2} \left(\frac{\partial \alpha}{\partial Q} \right)_0 Q_0 E_0 \cos(\omega_0 - \omega_j) t \\
 + \frac{1}{2} \left(\frac{\partial \alpha}{\partial Q} \right)_0 Q_0 E_0 \cos(\omega_0 + \omega_j) t
 \end{aligned}
 \tag{1.11}$$

The equation above contains three terms, meaning that the induced dipole oscillation is comprised of three frequencies that correspond to elastic scattering (Rayleigh scattering), which is the first term, and inelastic scattering (Raman scattering) that gives the other two terms: photons with a lower frequency (termed *Stokes* Raman scattering) and others with a higher frequency (termed *anti-Stokes* Raman scattering). Those are illustrated in Figure 1.4.

The main selection rule for Raman scattering results from the change in the polarizability during the motion of the vibration:

$$\left(\frac{\partial \alpha}{\partial Q} \right)_0 \neq 0
 \tag{1.12}$$

In practice, this means that the Raman or IR activity of each vibration depends on the symmetry of the molecule, as studied by group theory applied to molecular symmetry.^[16,17]

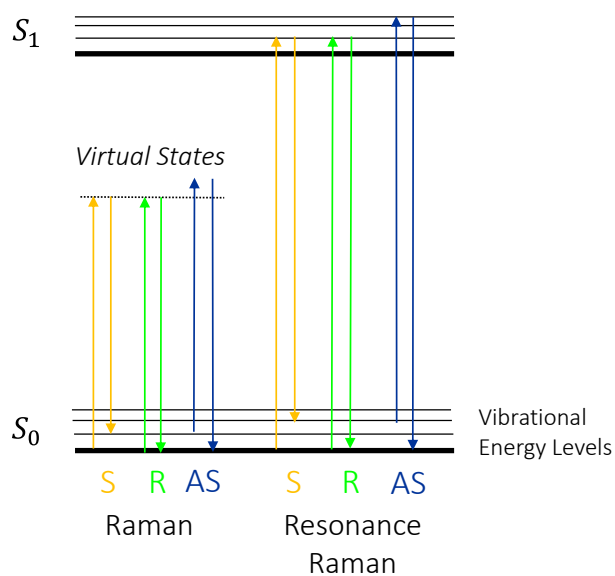


Figure 1.4. Jablonski diagram for Raman scattering processes.
S=Stokes, R=Rayleigh, AS=Anti-Stokes

1.2.3. Raman Spectra

Let us recall that the Stokes and anti-Stokes in Raman are relative to the incident light (which has the same wavelength as Rayleigh scattering); it is very important to notice that Raman scattering follows the wavelength of the Rayleigh scattering. Like IR spectra, Raman spectra are usually plotted in wavenumbers; not in absolute wavenumbers but in *relative* wavenumbers. The absolute wavenumber of the Rayleigh light is assigned as zero, and the difference between the Raman bands and the Rayleigh is plotted; this is called *Raman shift*. Stokes Raman scattering implies a positive Raman shift, and the anti-Stokes has negative Raman shift. So the spectrum is usually plotted as Raman shift versus Raman intensity, which usually means counts per second in a charge-coupled device (CCD) camera (see section 2.5.1). Figure 1.5 shows the complete Raman spectrum for carbon tetrachloride, showing both Stokes and anti-Stokes. Since Stokes Raman is much more intense than anti-Stokes, usually only the Stokes part is graphed and employed for analysis.

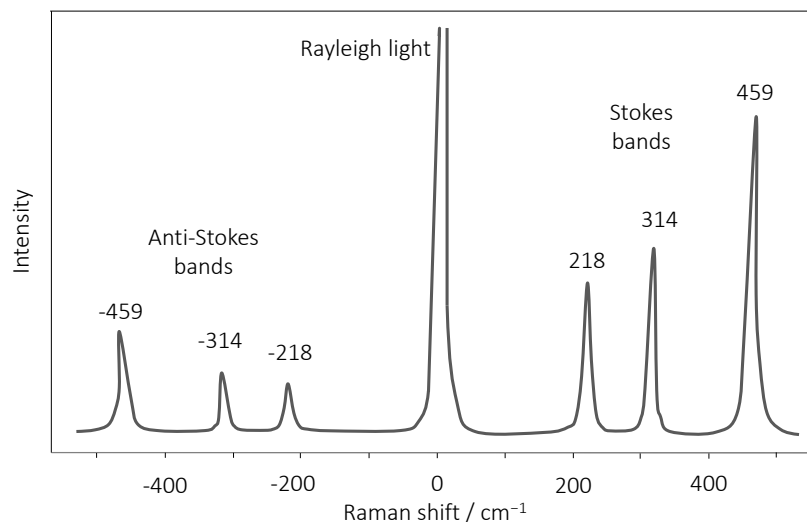


Figure 1.5. Complete Raman spectrum of carbon tetrachloride.

With Raman cross sections being quite small for most molecules, especially those not having a rigid structure with aromatic rings, makes the technique not as practical as IR. However, in the IR water is a big interferent because it has a large IR cross section, which does not allow for the visualization of anything else when water is present. On the contrary, water is a very poor scatterer, and indeed Raman spectroscopy finds a lot of applications in aqueous solutions where IR cannot be employed.

The low cross section problem can be circumvented in two ways: by employing resonance Raman scattering, by harnessing the plasmonic properties of metallic nanoparticles, i.e. doing SERS, and also by combining the two to obtain SERRS. All these are to be discussed in the following sections.

1.2.4. Resonance Raman Scattering

As we said before, when wavelength of the incident light matches that of an electronic transition, the scattered light is said to be *resonance Raman scattering* (RRS). Experimentally, the intensity of these spectra is much higher than those of regular Raman, in the order of 10^3 - 10^5 times as intense as regular Raman, thus increasing very much the sensitivity of the technique. It is also observed that the spectrum simplifies, for the enhancement only applies to the vibrations associated to the electronic transition.

If we go back to the Jablonski diagram in Figure 1.4 (page 11), we see that hitting an electronic transition means that the excitation is no longer into a virtual state, but instead

it goes directly into one of the excited states of the molecule. The Raman intensities, then, are determined by the properties of the excited state.

The coupling of the vibrational modes of a molecule to its electronic transition depends strongly on the dimensionless displacement between the ground and excited electronic potential energy surfaces along a normal coordinate. The most common case of RRS occurs when a component of the normal coordinate of a vibration is in the same direction that the molecule expands (polarizes) during an electronic excitation, which leads to an increase in the polarizability and the dipole moment as well. This happens most of the time with big aromatic molecules like dyes. The ring stretching modes of extended aromatic systems benefit particularly from this form of RRS enhancement of the signal, which is termed *Franck-Condon enhancement*. The ring breathing modes of these molecules are along the same normal coordinates as the expansion of the molecule that occurs when $\pi \rightarrow \pi^*$ transitions are excited. Consequently, these modes are greatly enhanced, preferentially over the other vibrational modes of the molecule.

Because of the above, RRS often happens in molecules that can also fluoresce. If the molecule can fluoresce, RRS and fluorescence can and will occur at the same time. If the fluorescence quantum yield is high, as is the case of molecules like octadecyl rhodamine B (R18, used in Chapters 4, 5 and 6) and the excitation light is in the vicinity of the spectrum (take the case of the laser line at 514.5 nm), the fluorescence falls in the same region as the RRS bands and fluorescence overpowers RRS, then only fluorescence is seen. But when the RRS bands are far apart from the fluorescence emission and the fluorescence quantum yield is not that high, as is the case for crystal violet in Chapter 6, both RRS and fluorescence appear in the same spectrum.

It is important to mention that overtones and combinations are rarely seen in non-resonant Raman scattering, but are allowed transitions in RRS, and are usually seen. Compare their complete absence in the SERS spectra for hydroxyproline in Chapter 3, and their easy observance in crystal violet and malachite green in Chapters 6 and 7.

1.3. Nanoparticles

According to the IUPAC (International Union of Pure and Applied Chemistry) glossary of terms used in toxicology, a **nanoparticle** is a microscopic particle whose size is measured in nanometres, often restricted to nanosized particles, that is, with an aerodynamic diameter* of less than 100 nm, also called ultrafine particles.^[18] Nanoparticles may adopt different shapes after synthesis, as a result of nucleation processes. An accurate description of these processes has been given by Sun.^[19]

The most common shape for nanoparticles, especially at sizes smaller than 50 nm, approximates a sphere. However, synthesis protocols have been described that allow the formation of nanoparticles of different shapes, and they are generally named after their apparent shape adding the “nano” prefix, thus we have nanospheres, nanorods, nanotriangles, etc. Nanoparticles of different shapes are shown in Figure 1.6.

* This aerodynamic diameter is, according to the same IUPAC Glossary, is defined as the diameter of a spherical particle, with a density equal to unity, that has the same deposition velocity in air than the particle into question.

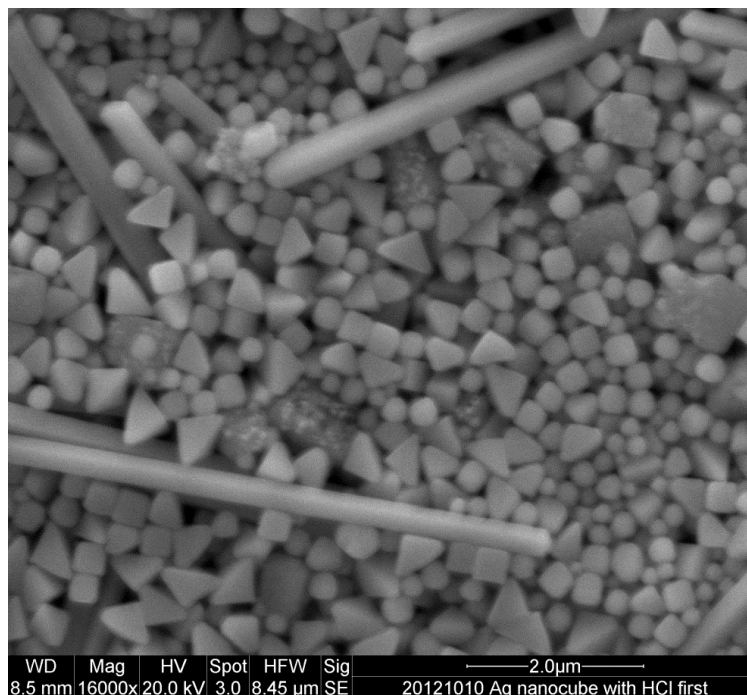


Figure 1.6. SEM image of nanoparticles of different shapes and sizes. Here we see nanowires, nanopyramids, nanocubes and nanospheres. Image courtesy of Wenhao Chen.

Metallic nanoparticles like those employed in this thesis form what is known as a *colloid* or *colloidal dispersion* composed by two separate phases, namely, the dispersed phase and the continuous medium. In our case, the particles, which are nothing but solid metal particles, are the dispersed phase, and the liquid medium (water in our case) is the dispersant phase. Metallic nanoparticles at the colloidal state form a *lyophobic* colloid, word which means “which hates the solvent”. The dispersion is thermodynamically unstable, unlike what happens in a lyophilic colloid where the dispersion is more stable than the components. This means that, eventually, separation of phases will occur, that is, particles will aggregate. However, the speed of separation can be almost infinitely slow: the gold colloids fabricated by Michael Faraday are still conserved and exhibited in the British Museum.

The stability of colloidal dispersion has been described in the classical theory called DLVO after the initials of its developers (Derjaguin, Landau, Verwey and Overbeek). This theory explains the stability as a function of the result of the particles being in a “tug-of-war” between two forces: electrostatic repulsion forces, and van der Waals attraction

forces. The latter is responsible of nucleation and growth, and also of aggregation, but for the particles to exist as such, the electrostatic repulsion must win in the end. DLVO forces and the exceptions to their rules are extensively described in Israelachvili's textbook.^[20] From there we can retrieve the most important equation for spherical particles:

$$U_{DLVO} = U_{\text{electrostatic}} + U_{\text{vdW}}$$

$$U_{DLVO} = \frac{64\pi k_B T R c \Gamma^2}{\kappa} e^{-\kappa D} - \frac{AR}{12D} \quad (1.13)$$

Where k_B is Boltzmann's constant, T is temperature in kelvins, R is the radius of the particles, c is the molar concentration of the particles, and Γ is a factor related to the surface potential of the particles. A is Hamaker's constant which is a number that characterizes the van der Waals interaction. Equation (1.13) offers several general cases of stability for a colloid. κ is a parameter related to the length of the electric double layer; κ^{-1} is the Debye length and represent the thickness of the electric double layer.

DLVO theory offers a good explanation when there are no other forces involved aside from van der Waals' attraction and electrostatic repulsion. However, there is an exception to the DLVO theory that comes for particles which are coated, especially with polymers; that is called *steric stabilization*. The adhesion forces may be stronger but if the particles are surrounded by a thick coating, like that provided by a polymer, the particle cores never really come into contact and they are harder to aggregate, thus providing a more stable colloid.

1.4. Plasmons

Nanosized particles of coinage (also called *noble*) metals like gold, and silver, and also copper, present the unique property of showing to the naked eye a colour that is remarkably different than that of the bulk metal. For example, gold has a characteristic "golden" colour when in the bulk, but in its nanoscale form it shows colours varying between orange-reddish and blue, depending on the size, as shown in Figure 1.7. Among

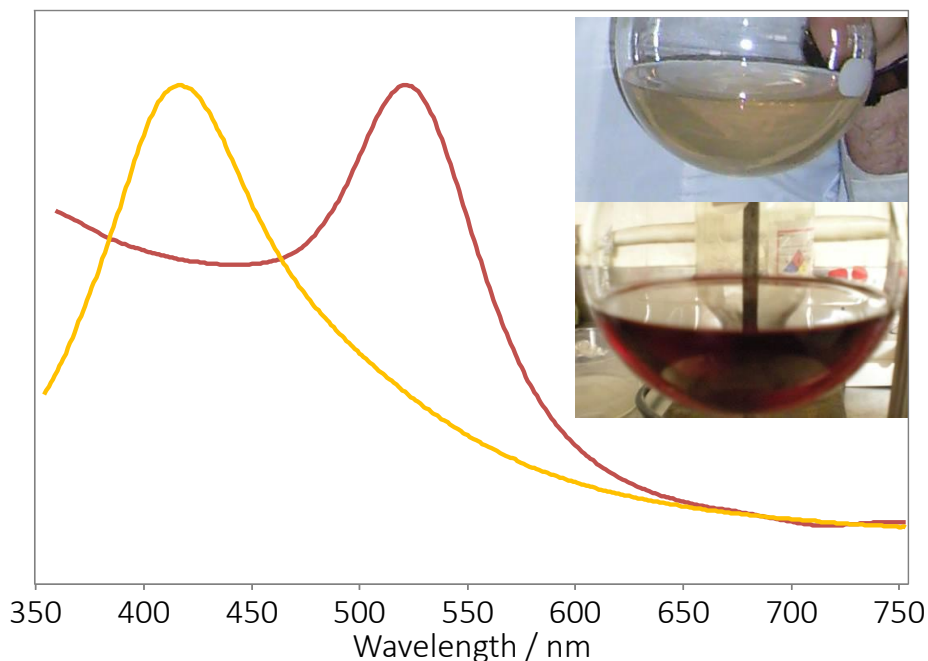


Figure 1.7. Plasmon absorption of silver and gold colloids. The yellow curve shows the plasmon absorption of a silver colloid at slightly above 400 nm and the red curve represents a gold colloid at above 500 nm. The inset shows photos of a silver colloid (above) and a gold colloid (below). In either case, particle sizes are around 50-60 nm. Sample spectra taken by the author.

the first ones to study the subject was J. C. Maxwell Garnett[†], who in 1904 published a paper that explained partly the colour of colloidal metal dispersions.^[21] This early model is now better understood in a subset of physics called *effective medium theory* and used for other applications.

The classical explanation for the colloids phenomenon was published in 1908, in a seminal paper by Gustav Mie,^[22] where he solved Maxwell's equations for spherical homogeneous particles with a plane monochromatic wave, thus describing the extinction (absorption plus scattering) spectrum for metal particles and explaining the colours seen. This and further related studies are usually called *Mie theory*, although the use of the term *theory* may be a bit inaccurate as he did not formulate any new equations. The subject has been of great interest, and over the years several reviews have been published on the linear

[†] Garnett's father, having met the famous physicist James Clerk Maxwell, was so impressed with him, that he named his son James Clerk Maxwell Garnett, and this son later became a physicist himself. This is the author of the 1904 paper.

optical properties of isolated metallic particles of arbitrary shape, with diameters of up to a few hundred nanometres.^[23] The original Mie paper assumed a spherical shape for the particles yielding an exact solution, but in reality particles may differ from a sphere, and this causes variations in their absorption and scattering. Gans^[24,25] adapted Mie's theory for its application in particles with different shapes, to include prolate and oblate ellipsoids smaller than the wavelength of light. Another problem of relevance for surface-enhanced spectroscopy is the coupling effect of interacting nanoparticles next to each other, which is approached under the *extended Mie theory*.

Since Maxwell's equations cannot be solved for arbitrary shapes, approximations are necessary. One of the most extended ways of performing the task of calculating absorption and scattering for nanostructures of different shapes is the so-called *discrete dipole approximation* (DDA). This method employs an arrangement of point dipoles that approximately match the shape of the nanostructure. With the advent of modern computers, the calculation of multiple dipoles becomes faster and feasible.

The main consequence of Mie's contribution is the concept, theory and study of *plasmons*. When a small spherical nanoparticle, much smaller than the wavelength of the incident light, is irradiated by a plane monochromatic wave, the oscillating electric field causes the electrons in the conduction band to oscillate coherently. These collective oscillations of the conduction electrons are called *localized surface plasmon resonances* (LSPR), usually shortened to *plasmons*.[‡] These plasmons are radiative, meaning that they scatter the incoming light to their vicinity. How much is scattered is a property of both the wavelength of the incident light (here we will express it as angular frequency, ω) and the nature of the material, as described in the *dielectric function* of the metal. This dielectric function is complex:

[‡] These *plasmons* should not be confused with those arising from large flat metal surfaces, usually termed *surface plasmon resonances*, which are non-radiative. Those give origin to another field of study called *surface plasmon spectroscopy*, which has nothing to do with SERS or SEF.

$$\varepsilon(\omega) = \varepsilon'(\omega) + i\varepsilon''(\omega) \quad (1.14)$$

Now, an incident electric field will induce a local electric field which in turn will be dependent on the shape and size of the particle, but most importantly on the dielectric function for the metal, and also that of the surrounding medium, and both of them are dependent on the wavelength of the light:

$$E \propto \frac{\varepsilon(\omega) - \varepsilon_0(\omega)}{\varepsilon(\omega) + 2\varepsilon_0(\omega)} \quad (1.15)$$

where ε is the dielectric function of the metal and ε_0 is the dielectric function of the surrounding medium. From this, we deduce that the electric field is at a maximum (that is, the best scattering by nanoparticles) when the conditions are such that a resonance is found (when ε'' is negligible):

$$\text{Re}[\varepsilon(\omega)] = -2\varepsilon_0 \quad (1.16)$$

The real part of the dielectric function must be in that resonance condition with the incident light. This is called the Fröhlich condition. As shown in Table 1.2,^[10,23,26] species fulfilling this condition are the well-known coinage or noble metals: silver (where the real part goes really close to -2 and the imaginary part is very close to zero), gold and copper to a lesser extent. Alkali metals also satisfy this, but they are not practical to work with, because they react violently with water. Other metals satisfy the conditions in different parts of the spectrum, either in the near IR or the UV.

The position of the absorption peak is dependent on the dielectric function of the metal, which is also modulated by the size and shape of the nanoparticle.^[27] The fabrication of nanoparticles of different sizes and shapes gives the possibility of tuning the position of the plasmon absorption, and therefore scattering, to one's particular needs. For our purposes, this means to tune where in the spectrum will SERS and/or SEF occur.

Metal	ε'	ε''	Plasmon resonance (nm)
Silver	-2.029919	+0.60192	350
Gold	-2.546544	+3.37088	496

Table 1.2. Dielectric function values for silver and gold

1.5. Surface-Enhanced Raman Scattering

Surface-Enhanced Raman Scattering (SERS) and Surface-Enhanced Fluorescence (SEF) represent the convergence of the paths of nanostructure development and of the analytical techniques of Raman and fluorescence spectroscopy, giving rise to new analytical techniques and new research avenues which find more and more applications every day because of their unique properties. The fundamentals of SERS have been extensively studied since its discovery, and the field has matured enough that today there are several textbooks on the subject.^[10,26,28-30] Here we will present a brief summary with the essentials only.

The amplification of Raman signals was observed for the first time in Dr. Martin Fleischmann's laboratory in 1974.^[31] The authors observed anomalously intense Raman spectra of pyridine coming from this substance in the vicinity of electrochemically roughened silver electrodes. The authors attributed the signal enhancement to a higher number of molecules placed near the electrodes. The interpretation of the phenomenon seemed strange since the beginning, and indeed, it was not long before it was challenged. It took the contributions of Jeanmaire and van Duyne,^[32] and those of Albrecht and Creighton,^[33] to set SERS in the right track: the augment in the signal could not be explained by the number of molecules alone, and the scientific community was in the presence of a new physical phenomenon. The history of the discovery has been told several times by its pioneers.^[34-37]

1.5.1. SERS Theory

Creighton proposed that the roughened electrodes acted much like colloidal nanoparticles, and indeed when he prepared gold and silver sols he reproduced the enhanced Raman.^[38] He went as far as to associate it to the Mie scattering of the silver and gold sols, having titled his paper "*Plasma Resonance Enhancement of Raman Scattering by Pyridine...*" However it was Dr. Rick van Duyne who coined the acronym SERS,^[39] in light of the increase in surface provided by the particles, and this name has stuck until today, although it is well understood and agreed upon, that it is the *plasmon* which is responsible

for the phenomenon. Some publications now talk about *plasmon*-enhanced spectroscopy,^[40] hence the title chosen for this thesis, but for historical reasons we will stick to the acronym SERS.

The first SERS models were proposed by Moskovits in 1978,^[41] Joel Gersten and Abraham Nitzan in 1980,^[42] and by Milton Kerker in 1980^[43] and 1984^[44]. A comprehensive review is given by Moskovits again in 1985.^[45] The models employ mostly classical electrodynamics to explain the phenomenon. First they used a single spherical nanoparticle and a molecule attached to it; this is the **spherical model of SERS**. Later Kerker refined his models to include other shapes also, like prolate spheroids. These early efforts already describe the fact that the EM enhancement accounts for most of what is seen, and allow to rationalize most of the experimental findings.

To avoid misconceptions,^[46] we will adopt Moskovits's definition^[47]: *“As it is currently understood SERS is primarily a phenomenon associated with the enhancement of the electromagnetic field surrounding small metal (or other) objects optically excited near an intense and sharp (high Q), dipolar resonance such as a surface plasmon polariton. The enhanced re-radiated dipolar fields excite the adsorbate, and, if the resulting molecular radiation remains at or near resonance with the enhancing object, the scattered radiation will again be enhanced (hence the most intense SERS is really frequency-shifted elastic scattering by the metal). Under appropriate circumstances the field enhancement will scale as E^4 where E is the local optical field”*.

The enhanced local field is illustrated in Figure 1.8. The enhanced Raman comes from the fact that in normal Raman the molecule has a very small cross section. In SERS, there are nanostructures with much higher cross section than the molecules, and therefore are much more efficient at capturing and scattering photons.

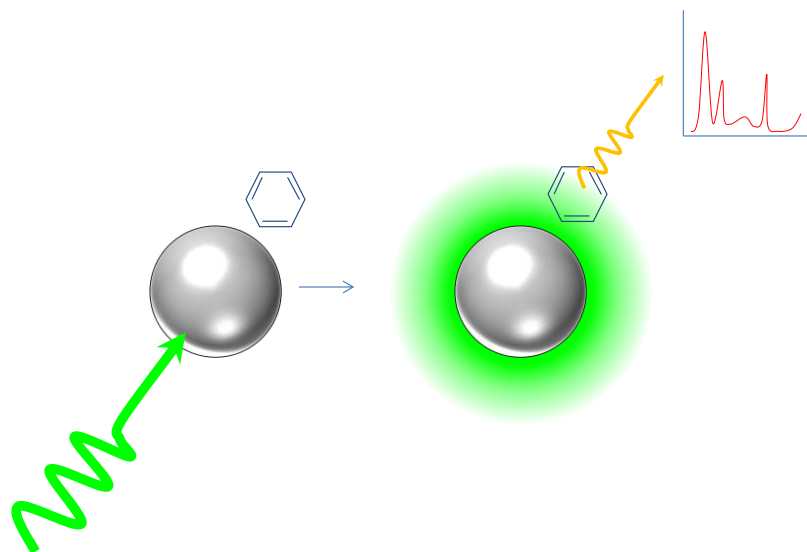


Figure 1.8. Simple diagram illustrating SERS.

Not every metal gives this phenomenon, of course. The capability of giving SERS is associated to the particle's capability of holding LSPR's, that is, a radiative plasmon that scatters light to the vicinity of the nanoparticle (see section 1.4) and this is why the phenomenon is restricted to coinage metals (silver, gold and copper).

At this point it is convenient to introduce the concept of **enhancement factor** (EF),^[26] or how many times the signal is enhanced when compared to taking a Raman spectrum in the same conditions but without the presence of nanostructures. Experimentally, this is given by:

$$\text{SERS EF} = \frac{I_{\text{SERS}}/N_{\text{SERS}}}{I_{\text{RS}}/N_{\text{RS}}} \quad (1.17)$$

where I_{SERS} is the intensity of Raman in SERS conditions, I_{RS} is the intensity in normal Raman conditions; N_{SERS} and N_{RS} are the corresponding number of molecules for each condition. The intensities I are usually calculated by fitting the area under the curve to theoretical Gaussian curves (usually a sum of them) and then calculating the area under the curve by integration. EF values for a SERS experiment may vary quite a bit; those reported in the earliest experiments were in the order of 10^5 - 10^6 .^[32] With better SERS substrates, and without considering RRS, those can be enhanced up to 10^8 - 10^{10} at best.^[26] Either way, the characteristic of SERS is the enhancement by several orders of magnitude.

From a theoretical point of view, there are two major electromagnetic contributors to these enhancement factors.^[26] We recall from basic electromagnetism that the intensity of the radiation in a certain point is always proportional to the square of the electric field in that point. Then the first enhancement term is called the *local field intensity enhancement factor*, and it is usually expressed as:

$$G_{loc} = |E^2| = \frac{|E_{loc}(\omega)|^2}{|E_{inc}|^2} \quad (1.18)$$

Here $E_{loc}(\omega)$ is the local electric field caused by the nanoparticle excitation, and E_{inc} is the incident electric field (say, the laser that illuminates the system). The idea is that the presence of the nanoparticle will make $E_{loc}(\omega)$ much larger than E_{inc} .

The second is called the radiation enhancement factor, caused by the re-emission at a different wavelength in Raman scattering (the scattered field) which we will write as G_{rad} .[§] This factor can be hard to solve from a physics point of view,^[26,48] and that is why a very comfortable approximation is usually employed, which is simply to assume that the Raman shift is negligible and therefore $G_{loc} = G_{rad}$. Therefore,

$$\text{SERS EF} = G_{loc}G_{rad} \approx G_{loc}G_{loc} \approx |E^4| \approx \frac{|E_{loc}(\omega)|^4}{|E_{inc}|^4} \quad (1.19)$$

From here comes the expression that the SERS enhancement is proportional to the fourth power of the electric field. It must be stressed that the expression above is an approximation only, being the so-called **E^4 approximation**. A more rigorous discussion of G_{loc} and the validity of the E^4 approximation has been done by Etchegoin and Le Ru.^[26,48]

The EF achieved is strictly dependent on the distance from the nanostructure to the molecule, as the electric field decreases as we move away from the surface of the nanostructure. If we consider a gold or silver nanosphere, it comes as obvious that the highest enhancement is obtained when the molecule is touching the surface of the nanoparticle, and that since the electric field decreases as we move the molecule away from the surface, the enhancement will decrease as well. The decrease in the SERS EM

[§] Some literature write M instead of G ; here we will prefer G .

enhancement for such a nanosphere is $\left|\frac{r}{r+d}\right|^{12}$, r being the nanoparticle radius and d the distance from the molecule to the nanoparticle.

This is the case for a nanosphere (spherical model), but real-life nanoparticles deviate from this shape. Indeed, to optimize the wavelengths at which light is better scattered by the nanoparticles, one may employ nanoparticles with shapes different than a sphere.

It is also very important to discuss the contribution of more than one nanoparticle to the EM enhancement. When molecules are placed on arrays of nanostructures, like a silver island film, or even a colloidal dispersion cast over a surface, molecules often fall in regions where they receive the EM enhancement of several nanoparticles, all of them contributing their EM enhancement to the molecule. Such a region of space is called a **hot spot**, and the existence of hot spots is one of the major justifications of the high enhancement factors classically observed in SERS.^[49,50]

1.5.2. Interpretation of SERS spectra

The interpretation of SERS spectra can be frustrating if all one wants is to rapidly achieve enhanced Raman spectra,^[10] for in many occasions the normal Raman spectrum *does not* match exactly the SERS spectrum; this is seen very well in our own SERS investigations of hydroxyproline in Chapter 3. One must remember that in regular Raman the molecule is moving freely in a medium, but in SERS the molecule is not alone: now it is in the vicinity of a nanostructure, interacting with it, and the SERS spectrum reflects that. In most SERS experiments the molecule is directly adsorbed to a nanoparticle, either by simple van der Waals attraction, which is termed *physisorption*, or by interactions whose energy is comparable to regular chemical bonds, which are termed *chemisorption*. Either way, in many occasions the molecule can be considered to be forming a complex with the nanoparticle, and therefore *it may lose the symmetry* it had before the adsorption. In general, a molecule in liquid or gas phase has a random orientation, but the adsorption to the nanoparticle makes the molecule adopt a *preferential spatial configuration*; the freedom is abruptly restricted. Therefore the selection rules in SERS are different than those in Raman. This topic was addressed by Dr. Martin Moskovits in 1982 in his seminal paper “Surface Selection Rules”.^[51]

The complexation with the nanoparticle brings a previously inexistent bonding between the molecule and the nanoparticle, thus changing the total number of vibrations, introducing new vibrations, introducing a new geometry (thus shifting the frequencies of existing vibrations), and also changing the electronic resonance frequencies of the molecule. This may account for part of the enhanced signal, thereby seeing resonance effects (surface-enhanced resonance Raman scattering, SERRS) that do not exist in the original molecule. It should be emphasized, however, that this is an effect of RRS and not part of the intrinsic EM enhancement brought about by the nanoparticle. This accounts for much of what has been broadly termed “chemical enhancement”, or spectral changes due to a chemical effect. One of the best examples of this effect is that of charge transfer in SERS experiments.^[52]

1.5.3. SERRS and Single-Molecule Detection

SERS opened up the possibility for very sensitive detection of chemicals. The next question was, of course, how far could the sensitivity limit be pushed? It was left to the experimentalists to try to figure it out.

In a paper from Katrin Kneipp’s group, one finds the first demonstration of SMD in aqueous solution. Independently, Shuming Nie and Emory in a Science paper in 1997^[53,54] also reported SMD using SERS. As noted by Le Ru and Etchegoin,^[26,55] the outlandishly high enhancement factors claimed in these papers arise not from electromagnetic SERS enhancement alone, but from the contribution of both SERS enhancement from the particles and the fact that the experiments were performed in resonance conditions (SERRS, for the Nie case).

Possibly the most relevant way of achieving SMD for the purposes of this thesis is that first proposed in 2001 by Carlos J. L. Constantino and Aroca, where the analyte is placed in a matrix which is a Langmuir-Blodgett (LB) film^[56] and using silver island films as the enhancing nanostructure. The hydrophobicity of the LB film and the ability of the technique to control very well the amount of molecules per unit of surface have made it possibly the most credible evidence for the detection of a single molecule. Many have indeed called

into question the proof for SMD; Etchegoin and Le Ru have described the advantages and disadvantages of using LB films, thus addressing the credibility of SMD claims.^[55]

1.6. Surface-Enhanced Fluorescence

As its name suggests, *surface-enhanced fluorescence* (SEF) is an analogue to SERS, but with fluorescence. However, the processes at play make it operate in a different way. In SERS, the mechanisms make it clear that the best SERS enhancement is obtained with the molecule directly adsorbed to the noble metal nanostructure, but in order to enhance fluorescence, it is necessary to put the molecule *a few nanometres away* from the surface of the nanostructures^[57] for, as it was mentioned before, noble metal nanostructures are well known fluorescence quenchers.

SEF has been called the “poor cousin of SERS”^[45] as its foundations do not allow it to achieve the spectacular EF values seen in SERS. The mechanism to achieve enhancement is still being researched upon, and is indeed the subject of Chapter 7 in this thesis.

The first ones to report experimental observation of SEF (or “enhanced luminescence” as it was described at the time) were Glass, Liao, Bergman and Olson in 1980,^[58] after a deliberate effort to see whether it was possible to achieve with fluorescence what had been done with Raman for SERS. The authors employed coinage metal films evaporated on top of glass, and then evaporated rhodamine dyes onto the films, obtaining enhanced fluorescence from the dye situated in between the particles. Later, the technique has been perfected to achieve better SEF by introducing spacer layers.

The acronym SEF was given following the lines of SERS, but in more recent years, Lakowicz and Geddes have introduced a new name for the same phenomenon, “metal-enhanced fluorescence” (MEF).^[59] One should be careful with this denomination as bulk metals are well known *quenchers*, rather than enhancers, of fluorescence. Plus, today it is well known and agreed upon that the cause of the phenomenon is the plasmon, so probably the most accurate description would be *plasmon-enhanced fluorescence* (as we prefer and use occasionally here, especially for the titles) or *plasmon-coupled*

fluorescence.^[60] Just like with SERS, for historical reasons we will employ the SEF denomination for most of this thesis, while acknowledging the limitation of the name.

1.6.1. Theoretical Model

The abundance of factors at play on the origin and mechanism of SEF, like the extinction coefficient of the molecule, its intrinsic quantum yield, the excitation power, and the presence or absence of hot spots, have made the subject quite difficult to study. The origin of SEF still has many things that have not been properly described, and that is the motivation of the research presented in Chapter 7.

As with SERS, Gersten and Nitzan have first provided the first theoretical basis for the understanding of SEF.^[61] In order to achieve the maximum enhancement, the target molecule must be placed a few nanometres away from the enhancing nanostructure, for it is well known that the enhancing nanostructure is also a fluorescence quencher. What happens is that the quenching (or Förster energy transfer) and the EM enhancement are in direct competition. The experimental SEF enhancement factor is defined analogously to the SERS EF:

$$\text{SEF EF} = \frac{I_{SEF}/N_{SEF}}{I_{RF}/N_{RF}} \quad (1.20)$$

Here the RF subindices mean ‘regular fluorescence’, the rest is analogous to equation (1.17) and the intensities are obtained from experimental data in the same way, except that fluorescence peaks are very broad and take up areas much larger than those of Raman, if they are viewed in the same spectral window.

Fluorescence, however, is a process of several steps, and this means that the radiative component of the SEF EF can be due to a modification of the decay rates (radiative and non-radiative). Therefore, assuming an optimal radiative enhancement, from the theoretical point of view, the SEF EF can only benefit from the local electric field enhancement, and it looks like:

$$\text{SEF EF} = G_{loc} = |E^2| = \frac{|E_{loc}(\omega)|^2}{|E_{inc}|^2} \quad (1.21)$$

Therefore the EF is proportional only to the square of the electric field at the location where the molecule is placed. The relationship between the EFs of both SERS and SEF until very recently was only theorized, but now has been demonstrated experimentally by the author of this thesis, and it is the subject of the research presented in Chapter 6.

In SEF the enhancement is dependent on the distance from the nanostructure, although not exactly in the same way as SERS. For illustrative purposes, let us consider a nanosphere of, say, 40 nm of radius, as illustrated in Figure 1.9. The EM enhancement for SEF decays as $|\frac{r}{r+d}|^6$, (the square root of that of SEF) where r is the radius of the nanoparticle and d is the distance from it; this is the blue line. The quenching, on the other hand, decays as $\frac{1}{|d^3|}$ (red line). Therefore, the total enhancement would be the difference between the two, $|\frac{r}{r+d}|^6 - \frac{1}{|d^3|}$ (green line). The graph clearly shows that there is an optimal distance; the maximum effective EM enhancement happens at about 2.5 nm from the surface of the nanostructure and it decays when the molecule is placed further away. Between that maximum and the nanoparticle, quenching dominates. This is in qualitative agreement with experimental results; one must take into account that the actual maximum EF distance is affected by the fact that nanoparticles are not perfectly spherical, and also because of presence of hot spots. There are several papers documenting the experimental evidence for this optimal distance and how the enhancement decreases with the distance for both SERS and SEF. ^[62-66]

This means now that in our experiments, in order to achieve a good SEF enhancement, we have to include a spacer layer between the molecule and the nanoparticle. In most cases this has been achieved by coating the enhancing nanostructures with a layer of silica (SiO₂). In the early days of SEF, the nanostructures were usually affixed to a glass substrate and silica had to be evaporated on top of that, but recently we have employed wet chemistry methods to coat colloidal gold and silver with silica in the development of what we have called SHINEF, as is shown in Chapters 4 to 7 of this thesis.

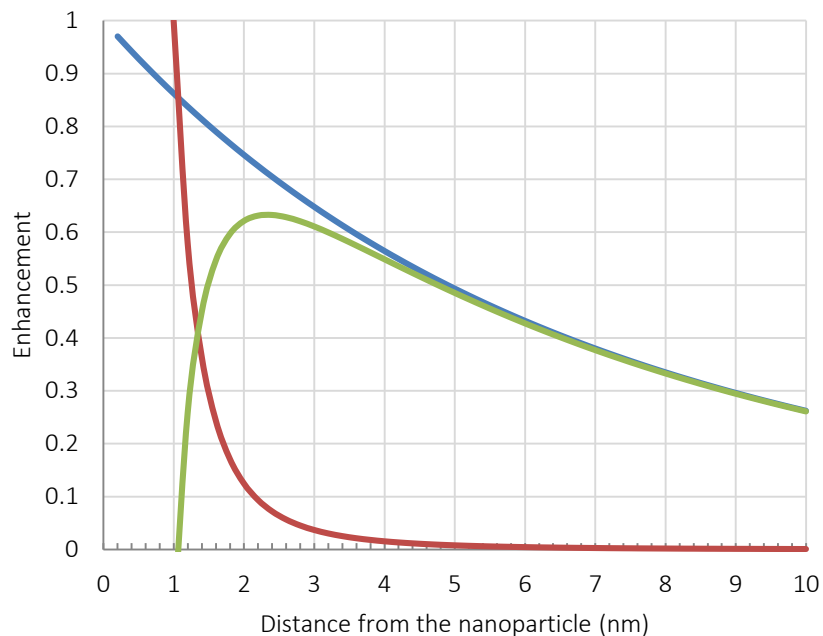


Figure 1.9. The theoretical distance dependence in SEF. The blue line represents the EM enhancement, the red line the quenching, and the green line is the effective enhancement.

1.7. References

1. Skoog, D.; Holler, F. J.; Nieman, T. A. *Principles of Instrumental Analysis*; 5th ed.; Saunders College Publishing: Philadelphia, 1998.
2. Lakowicz, J. R. *Principles of Fluorescence Spectroscopy*; 3rd ed.; Springer: New York, 2006; Vol. 1.
3. Valeur, B.; Berberan-Santos, M. N. *J. Chem. Educ.* **2011**, *88*, 731.
4. Stokes, G. G. *Philos. T. R. Soc. Lond.* **1852**, *142*, 463.
5. Chance, R. R.; Prock, A.; Silbey, R. In *Advances in Chemical Physics*; John Wiley & Sons, Inc.: 1978, p 1.
6. Long, D. A. *The Raman Effect. A unified treatment of the theory of Raman scattering by molecules*; John Wiley & Sons, Ltd, 2002.
7. Wilson, E. B.; Decius, J. C.; Cross, P. C. *Molecular Vibrations: The Theory of Infrared and Raman Vibrational Spectra*; Dover Publications: New York, 1955.

8. Lambert, J. B.; Shurvell, H. F.; Lightner, d. A.; Cooks, G. *Introduction to Organic Spectroscopy*; Macmillan Publishing Company: New York, 1987.
9. Nakamoto, K. *Infrared and Raman spectra of inorganic and coordination compounds. Part A: Theory and applications in inorganic chemistry.*; Fifth Edition ed.; John Wiley & Sons, Inc: New York, 1997.
10. Aroca, R. *Surface-Enhanced Vibrational Spectroscopy*; John Wiley & Sons.: Chichester, 2006.
11. Raman, C. V. *Indian J. Phys.* **1928**, *2*, 387.
12. Raman, C. V.; Krishnan, K. S. *Nature* **1928**, *121*, 501.
13. Smekal, A. *Naturwissenschaften* **1923**, *11*, 873.
14. Landsberg, G.; Mandelstam, L. *Naturwissenschaften* **1928**, *16*, 557.
15. Singh, R. *Phys. Perspect.* **2002**, *4*, 399.
16. Cotton, F. A. *Chemical Applications of Group Theory*; 1st ed.; Wiley: New York, 1963.
17. Ferraro, J. R.; Zioemek, J. S. *Introductory Group Theory and its Applications to Molecular Structure*; Plenum: New York, 1969.
18. Duffus, J. H.; Nordberg, M.; Templeton, D. M. *Pure Appl. Chem.* **2007**, *79*, 1153.
19. Sun, Y. *Chem. Soc. Rev.* **2013**, *42*, 2497.
20. Israelachvili, J. N. *Intermolecular and Surface Forces*; 2nd ed.; Academic Press: San Diego, CA, 1992.
21. Garnett, J. C. M. *Philos. T. R. Soc. Lond.* **1904**, *203*, 385.
22. Mie, G. *Ann. Phys.-Leipzig* **1908**, *25*, 377.
23. Meier, S. A. *Plasmonics: Fundamentals and Applications*; 1st ed.; Springer Science: New York, NY, 2007.
24. Gans, R. *Ann. Phys.-Leipzig* **1912**, *342*, 881.
25. Gans, R. *Ann. Phys.-Leipzig* **1915**, *352*, 270.
26. Le Ru, E. C.; Etchegoin, P. G. *Principles of Surface Enhanced Raman Spectroscopy (and related plasmonic effects)*; Elsevier: Amsterdam, 2009.
27. Willets, K. A.; Van Duyne, R. P. *Annu. Rev. Phys. Chem.* **2007**, *58*, 267.

28. *Surface Enhanced Raman Spectroscopy*; Schlücker, S., Ed.; John Wiley & Sons: Chichester, 2011.
29. Chang, R. K.; Furtak, T. E. *Surface-Enhanced Raman Scattering*; 1st ed.; Plenum Press: New York, 1982; Vol. 1.
30. *Surface Enhanced Raman Scattering: Physics and Applications*; Kneipp, K.; Moskovits, M.; Kneipp, H., Eds.; Springer: Berlin, 2006; Vol. 1.
31. Fleischmann, M.; Hendra, P. J.; McQuillan, A. J. *Chem. Phys. Lett.* **1974**, *26*, 163.
32. Jeanmaire, D. L.; Van Duyne, R. P. *J. Electroanal. Chem. Interfacial Electrochem.* **1977**, *84*, 1.
33. Albrecht, M. G.; Creighton, J. A. *J. Am. Chem. Soc.* **1977**, *99*, 5215.
34. Kerker, M. *Appl. Optics* **1991**, *30*, 4699.
35. Haynes, C. L.; Yonzon, C. R.; Zhang, X.; Van Duyne, R. P. *J. Raman Spectrosc.* **2005**, *36*, 471.
36. Moskovits, M. *J. Raman Spectrosc.* **2005**, *36*, 485.
37. McQuillan, A. J. *Notes Rec. Roy. Soc.* **2009**, *63*, 105.
38. Creighton, J. A.; Blatchford, C. G.; Albrecht, M. G. *J. Chem. Soc., Faraday Trans. 2* **1979**, *75*, 790.
39. Van Duyne, R. P. In *Chemical and Biochemical Applications of Lasers*; Moore, C. B., Ed.; Academic Press: New York, 1979; Vol. 4, p 101.
40. Aroca, R. F. *Phys. Chem. Chem. Phys.* **2013**, *15*, 5355.
41. Moskovits, M. *J. Chem. Phys.* **1978**, *69*, 4159.
42. Gersten, J.; Nitzan, A. *J. Chem. Phys.* **1980**, *73*, 3023.
43. Kerker, M.; Wang, D. S.; Chew, H. *Appl. Optics* **1980**, *19*, 4159.
44. Kerker, M. *Acc. Chem. Res.* **1984**, *17*, 271.
45. Moskovits, M. *Rev. Mod. Phys.* **1985**, *57*, 783.
46. Moskovits, M. *Phys. Chem. Chem. Phys.* **2013**, *15*, 5301.
47. Douketis, C.; Haslett, T. L.; Wang, Z.; Moskovits, M.; Iannotta, S. *J. Chem. Phys.* **2000**, *113*, 11315.
48. Le Ru, E. C.; Etchegoin, P. G. *Chem. Phys. Lett.* **2006**, *423*, 63.

49. Cang, H.; Labno, A.; Lu, C. G.; Yin, X. B.; Liu, M.; Gladden, C.; Liu, Y. M.; Zhang, X. *Nature* **2011**, *469*, 385.
50. Kleinman, S. L.; Frontiera, R. R.; Henry, A.-I.; Dieringer, J. A.; Van Duyne, R. P. *Phys. Chem. Chem. Phys.* **2013**, *15*, 21.
51. Moskovits, M. J. *Chem. Phys.* **1982**, *77*, 4408.
52. Lombardi, J. R.; Birke, R. L. *Acc. Chem. Res.* **2009**, *42*, 734.
53. Kneipp, K.; Wang, Y.; Kneipp, H.; Perelman, L. T.; Itzkan, I.; Dasari, R. R.; Feld, M. S. *Phys. Rev. Lett.* **1997**, *78*, 1667.
54. Nie, S.; Emory, S. R. *Science* **1997**, *275*, 1102.
55. Etchegoin, P. G.; Le Ru, E. C. *Phys. Chem. Chem. Phys.* **2008**, *10*, 6079.
56. Constantino, C. J. L.; Lemma, T.; Antunes, P. A.; Aroca, R. *Anal. Chem.* **2001**, *73*, 3674.
57. Goulet, P. J. G.; Aroca, R. F. In *Radiative Decay Engineering*; Geddes, C. D., Lakowicz, J. R., Eds.; Springer US: 2005; Vol. 8, p 223.
58. Glass, A. M.; Liao, P. F.; Bergman, J. G.; Olson, D. H. *Opt. Lett.* **1980**, *5*, 368.
59. Geddes, C. D.; Lakowicz, J. R. *J. Fluoresc.* **2002**, *12*, 121.
60. Höppener, C.; Novotny, L. Q. *Rev. Biophys.* **2012**, *45*, 209.
61. Gersten, J.; Nitzan, A. *J. Chem. Phys.* **1981**, *75*, 1139.
62. Murray, C. A.; Allara, D. L. *J. Chem. Phys.* **1982**, *76*, 1290.
63. Wokaun, A.; Lutz, H. P.; King, A. P. *Springer Ser. Chem. Phys.* **1983**, *33*, 86.
64. Wokaun, A.; Lutz, H. P.; King, A. P.; Wild, U. P.; Ernst, R. R. *J. Chem. Phys.* **1983**, *79*, 509.
65. Kovacs, G. J.; Loutfy, R. O.; Vincett, P. S.; Jennings, C.; Aroca, R. *Langmuir* **1986**, *2*, 689.
66. Aroca, R.; Kovacs, G. J.; Jennings, C. A.; Loutfy, R. O.; Vincett, P. S. *Langmuir* **1988**, *4*, 518.

Chapter Two

Experimental Methods and Instrumentation

2.1. Colloidal Wet Chemistry Methods

Most of the nanostructures fabricated in the following chapters are obtained by chemical reduction of oxidized salts of the coinage metals mentioned in Chapter 1, and the action of a stabilizing agent.

2.1.1. Synthesis of Gold Nanospheres

Forms of what we know today as colloidal gold had been known since Antiquity.^[1] In Ancient Egypt colloidal gold was known for its supposed medicinal properties. In Rome, it was found the Lycurgus cup that has the unique property that when lit from the inside has a different colour than when lit from outside.

Among the first methods developed to produce colloidal gold in the laboratory was that published by John Turkevich, then graduate student Peter Cooper Stevenson, and James Hillier in 1951.^[2] In that paper, the authors use several reagents and protocols for the reduction of gold chloride, but the method that gave them the best results was that in which they used trisodium citrate as a reducing agent, and the paper is remembered mostly for establishing the citrate reduction as a method to obtain colloidal gold.^[3] They obtained particles of about 20 nm, analyzed by then-recently invented TEM. Turkevich's method was later perfected by Frens in 1973^[4] having described that by varying the citrate-to-gold ratio, it was possible to produce nanoparticles of different sizes, while still having a reasonable dispersion in size. An example of this type of particles can be seen in Figure 2.1.

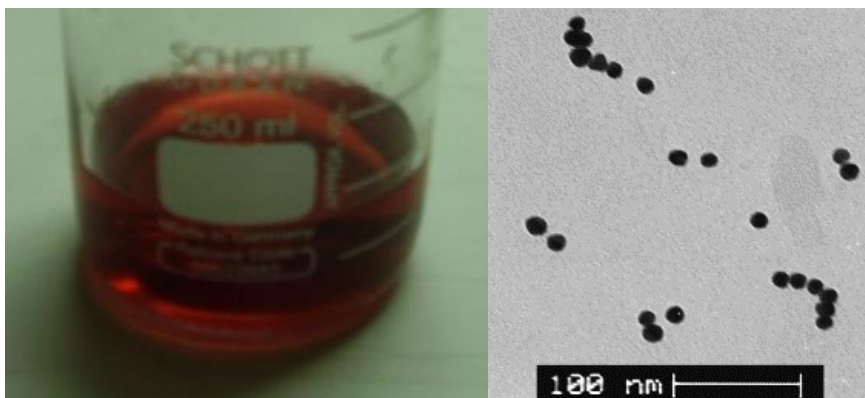


Figure 2.1. Citrate-reduced gold colloid.
Left: macroscopical view of the colloidal dispersion. Right: TEM image of the nanoparticles. Unpublished images taken by the author.

In citrate reduction, citrate is oxidized to acetonedicarboxylate, suffering the loss of the carboxyl adjacent to the hydroxyl; the latter is lost as CO_2 which in turn lowers the pH. The reaction generates chloride ions which are neutralized by one of the sodium ions from the citrate. Also, acetonedicarboxylate continues to oxidize to formic acid and CO_2 . Then, Au^{3+} (as tetrachloroauric acid, HAuCl_4) is reduced to metallic gold, Au^0 . Attraction forces (van der Waals) predominate, atoms aggregating to each other in a nucleation process.

This nucleation process does not continue indefinitely. It has been described that part of the Au^{3+} is not completely reduced, but is left in the intermediate oxidation state (Au^+). These Au^+ atoms place themselves on top of the nanoparticle which then acquires a positive surface charge. This charge attracts electrostatically citrate molecules, which end up being adsorbed on the surface of the nanoparticle. Two of the carboxylic groups of citrate counter the surface positive charges; the remaining one looks outwards. The particles finally acquire negative charge and electrostatic repulsion becomes enough to counter the van der Waals adhesion, becoming nanoparticles (see section 1.3). Evidence supporting this explanation can be found in the work of Li and collaborators.^[5]

2.1.2. Synthesis of Silver Nanospheres

Among the modern methods to obtain colloidal silver, one of the most cited publications is that of Lee and Meisel in 1982.^[6] This paper is remarkable as it represents the first silver colloids synthesized specifically to produce a SERS substrate. It remains really

popular in literature. It is analogue to the gold-citrate reduction, with the difference that the synthesis starts from silver nitrate (AgNO_3), and there cannot be a partial reduction of silver, however, there are probably some Ag^+ ions incorporated into the nanoparticle, as well as some clusters composed of several Ag atoms like those described by Linnert and Mulvaney.^[7]

Another very popular reducing agent to produce colloidal silver is hydroxylamine (NH_2OH). One of the better known papers where they employ this method is that of Leopold and Lendl.^[8]

2.1.3. Nanoparticles with different shapes

After attempting to synthesize sphere-like particles, there were several attempts to synthesize particles with different shapes. Possibly the simplest shape to synthesize, after a sphere, is a rod-like particle. But the synthesis of such particles in high yield becomes hard; the addition of different salts becomes necessary to orient the nucleation in one direction rather than having the process completely random.

The first published method to produce nanorods in high yield was done by Jana *et al.*^[9] where they employ a two-pot reaction. They start by synthesizing very small silver nanoparticles (2-3 nm) reducing from silver nitrate with a strong reducing agent (sodium borohydride, NaBH_4); this is called the *seeds solution*. Then an aliquot of this solution is placed over another solution (the *growth solution*) where there is silver nitrate with a weaker reducing agent (ascorbic acid); here the seeds are expected to grow linearly. The aspect ratio of the nanorods is controlled by how much seed solution is placed into the growth; the less seed is placed, the longer the rods that are produced. The rods are stabilized by the presence of the surfactant cetyltrimethylammonium bromide (CTAB), which adsorbs on the surface of the rods giving them a positive charge.

Possibly the best known method to produce gold nanorods was published by Babak Nikobaakht and Mostafa El Sayed.^[10] They built upon Jana's method, and that is how this is also a seeded method. In their seeds, they start from the original HAuCl_4 making small seeds of gold nanoparticles, always reducing with NaBH_4 , and then they pour a little of the seeds into a growth solution containing ascorbic acid. The main difference is that in their

method, they introduce another reagent (silver nitrate, AgNO_3) to control the aspect ratio. They always employ CTAB to stabilize their nanorods. This method, with minor modifications, is the one we employed in Chapter 5. Prof. El Sayed's group have very recently developed another method, this time a seedless method, to produce gold nanorods.^[11] The reproducibility of this newer method has yet to be tested.

It is possible to synthesize many different shapes but one of the main questions that appear at the moment of developing it is the yield, that is, of all the nanostructures produced, how many of them achieve the desired shape? Prof. El Sayed's is the most used nanorod synthesis method because it achieves a very high yield, and the method is very reproducible. Many authors have tried variations on this synthesis to achieve different shapes, but it is very hard to obtain them in good yield.

2.1.4. Coating with Silica

In this thesis we employed two processes to coat our nanostructures with silica (silicon dioxide, SiO_2), thus producing the so-called *shell-isolated nanoparticles* (SHINs). The general procedure to coat gold structures with silica evolved from the original research published by Werner Stöber in 1960^[12] for the production of silica spheres and has been used since then by many, many others. In Stöber's original paper they already used the reagent tetraethylorthosilicate (TEOS) still employed until now, which hydrolyzes to ethanol and silica. The final products in Stöber's original paper were nanometric silica spheres, but soon it was discovered that when performing the same process in a metal colloid, the silica started to grow on top of the colloidal particles. Therefore the method resulted useful to coat the particles, and is usually dubbed as *the Stöber method*, after its discoverer.

The Stöber method has the disadvantage of being somewhat slow, considering that in order to produce relatively thick coatings (greater than 10 nm) it needs a day, or maybe two. Plus the fact that TEOS does not dissolve in water, and therefore it is necessary to use a miscible co-solvent (usually ethanol or methanol) to dissolve the TEOS and let the reaction proceed. Luis Liz-Marzán and Paul Mulvaney have published another way to coat gold nanoparticles,^[13,14] with a method that starts from citrate-reduced nanoparticles; then

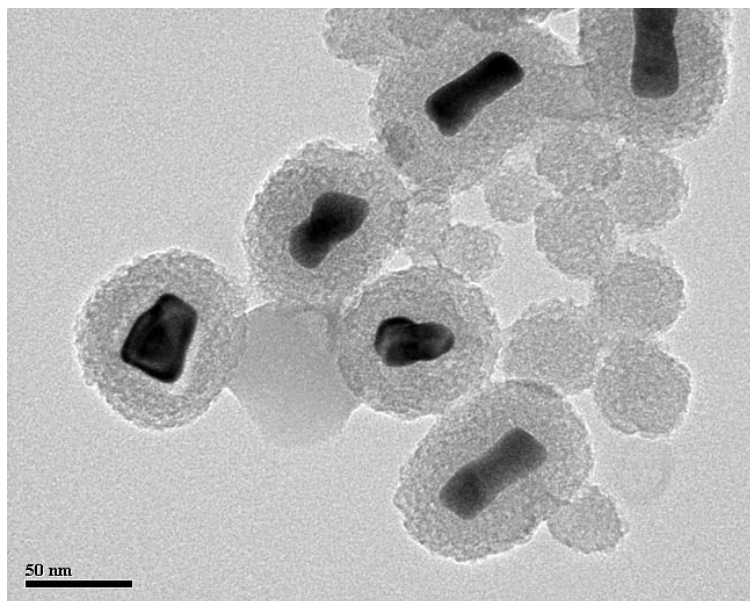


Figure 2.2. Silica-coated gold nanorods, coated using the Stöber method.

employs 3-aminopropyl-trimethoxysilane (APTMS) as an anchor for the silica, and then sodium silicate solution (which is just silica plus other oxides) to grow that silica on the particles. This method has the particularity that the sodium silicate solution must be activated; the silicate solution is very alkaline and it must be acidified a little for the silicate to polymerize and grow on the particle; in order not to increase the volume by addition of, say, hydrochloric acid, this is done by passing the solution through an acidifying resin. In their SHINERS paper, Li *et al.*^[15] have adapted this method with one modification: they have added heat, in the form of a water bath, to speed up the process, thus reducing the time to achieve a coating of about 2 nm to 15-20 minutes. We have employed this sped-up method in Chapter 5, but heating for longer times to produce thicker coatings.

It is usually considered that just like in the Stöber method, the APTMS suffers hydrolysis of the methoxyl groups at the moment of silica growth, therefore yielding some methanol as a byproduct, and growing only silica on the particle. This is consistent with the fact that neither the SHINERS authors nor us attempting SHINEF have seen SERS of APTMS when employing SHIN particles.

2.1.5. Other experimental details

All aqueous solutions for reagents, and also the colloidal dispersions, were made using Milli-Q® water. This is obtained from filtering systems (branded Milli-Q) by Millipore, Inc. that guarantee water that is free from particulate material and ions, and for that reason it is sometimes branded as *nanopure water*. The presence of ions is regulated by measuring the resistivity of the water; the accepted value is 18.2 MΩ·cm. We obtained our Milli-Q water from the filters available at the Stockroom in the Biology building at the University of Windsor.

In order to remove the gold and silver debris from previous experiments, and before working with gold and silver again, all glassware was cleaned with *aqua regia*, a mixture of concentrated hydrochloric acid and nitric acid, 3:1 in volume. The glassware was left in *aqua regia* for at least 20 minutes.

For glassware cleaning that required organic matter destruction, we employed Piranha solution, a mixture of concentrated sulfuric acid and hydrogen peroxide 30%, 7:3 in volume.

After the treatment with these strong acid solutions, the glassware was rinsed at least six times with Milli-Q water.

Unless otherwise specified, all reagents were purchased from Sigma-Aldrich and used without further purification.

2.2. Electron Microscopy

The nanostructures presented in the two previous subsections cannot be characterized morphologically (here morphology means size and shape of the particles) using traditional optical microscopy, as the size of the structures fall below the wavelength of visible light. In order to be able to resolve smaller objects, electron microscopy was invented.^[16,17]

As the name suggests, electron microscopy techniques employ electrons instead of photons of visible light to achieve that extra resolution; at high vacuum, an electron beam is directed to the sample. Since electrons are used, those electrons (unlike photons) have

all the same wavelength; this means that all electron microscopy images are necessarily black and white. It is possible to add colour using computer programs to better visualize images, but this is external to the technique.

2.2.1. Transmission Electron Microscopy

Transmission Electron Microscopy (TEM) is the oldest form of electron microscopy (it was invented in 1932 and improved upon in the rest of that decade) and it remains the technique of choice for characterization of the morphology of colloidal particles at the nanoscale.

The characteristic of TEM is that an electron beam is made to pass *through* an ultra-thin sample (electrons are transmitted), interacting with the sample as it passes through. The contrast in the image thus obtained is due to the absorption of electrons. This image is magnified by lenses (here those lenses are not crystals as when working with normal light; they are magnets that alter the path of the electrons) and then it is focused into an imaging device. In older days this used to be a fluorescent screen or a layer of photographic film, but in modern days a CCD camera (see section 2.5.1 for more details) is employed for digitalization of the image and control by computers.

The main advantage of TEM as an imaging technique is its resolution. Modern high-resolution TEM instruments allow for the visualization of structures at the nanoscale and even sub-nanoscale. It is often possible to visualize the crystal structure within a nanoparticle, identifying all the planes in it. Another feature of TEM is the possibility of obtaining electron diffraction patterns, which give more information on the crystal structure of the sample analyzed. Another technique associated with TEM is electron energy loss spectroscopy (EELS).

The main disadvantage of TEM is that the images produced are essentially just a cross-section of whatever is in the sample. It can also be argued that the sample preparation can be time-consuming and costly. In the particular case of nanoparticle systems, the colloidal dispersions are placed into a typical TEM copper grid, but one that is coated either with carbon or Formvar (polyvinyl formal). Then the particles get stuck into this Formvar polymer and then it is possible to see them in the microscope. Overall this is not very

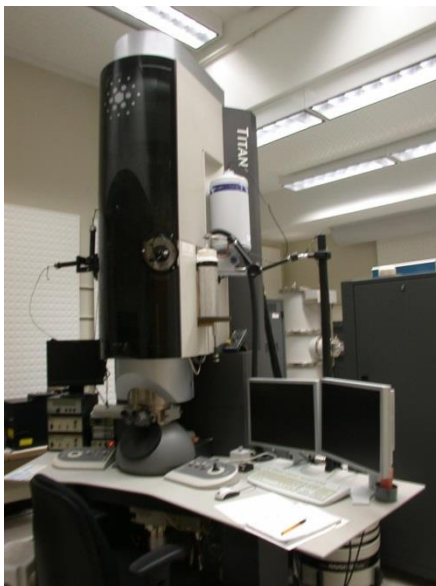


Figure 2.3. FEI Titan 800B transmission electron microscope.
This instrument is located at the Canadian Centre for Electron Microscopy,
McMaster University.

complicated, but if what one wants to see is, say, a cell and its elements within, then it becomes necessary to use highly expensive machines to cut the sample and obtain an ultrathin slice; such devices are called ultramicrotomes.

If what one needs is just a cross section, then TEM is the technique of choice, and that is how most papers involving nanoparticles include TEM images for the characterization of those nanoparticles. But if one desires to visualize things in 3D, it is necessary to employ other high-resolution microscopy techniques, like SEM and AFM, which are to be described next.

Used for this thesis work: Most TEM images for this work (all of those included in this volume) were obtained with a high resolution TEM instrument FEI Titan 80-300 at the Canadian Centre for Electron Microscopy at McMaster University in Hamilton, Ontario, Canada. The instrument is shown in Figure 2.3.

2.2.2. Scanning Electron Microscopy

Scanning Electron Microscopy (SEM) was invented after TEM and it allows for the visualization of the shapes of micro and nanostructures. The difference with the TEM is

that, as its name suggests, the electron beam is made to *scan* the surface in a rastering process, and it is the bouncing electrons that produce the image.

The received electrons are mainly two types: the *secondary electrons* (SE) and the *backscattered electrons* (BSE). Secondary electrons are called so because they are generated by ionization of the sample (rather than being scattered by it) and they are usually the main way of visualizing images in SEM. The backscattered electrons, as the name suggests, are electrons that are scattered by the sample in the exactly opposite direction to the laser beam.

The resulting images usually appear much like a black and white photo of the sample, especially for the SE image and when not much magnification is applied. The BSE image can be more useful to give an idea of the chemical composition, for it is a reflection of the electron density of the materials. That is why, for example, starting with Chapter 5, in the SEM images of SHINs it is possible to better observe the particle cores with the BSE image, while the silica shell is observed better with the SE image. Most of the images presented are a composite image of both SE and BSE.

The main advantage of SEM imaging is how it allows to observe objects as if one were standing right in front of them, giving a sense of perspective to the captured images, still with very high resolution (while not as high as TEM) and nowadays, with a bit of computational aid, it is even possible to reconstruct the 3D image. It also has the advantage that the same instrumentation can allow to use the beam for energy-dispersive X-ray spectroscopy (EDX), a technique that allows for identification of the chemical elements present in a substance.



Figure 2.4. FEI Quanta 200 Environmental scanning electron microscope. This was the instrument employed in all the SEM work for this thesis. Image courtesy of Mrs. Sharon Lackie

Disadvantages of SEM also have to do with sample preparation. Metallic surfaces require little to no preparation, but non-conductive samples like organic matter usually have the problem that when the electron beam hits them, electrostatic charge accumulates in their surface which causes image artifacts. Because of this, most organic samples have to be coated with some conductive material, like graphite or carbon. Sometimes to achieve a better effect, they are coated with gold. Of course, this introduces extra thickness in the image. For most biological samples where features are at the micro scale rather than at the nanoscale, the thin gold film is not a problem, but when employing SEM to characterize nanoparticles it is important to try not to coat them as the features might get a bit of distortion. In particular, we have noticed that in SHIN particles like those employed in Chapters 5-8 the silica shell usually appears thicker than in the TEM image.

Used for this thesis work: All SEM images in this thesis were taken with a FEI Quanta 200 Environmental scanning electron microscope equipped with an Everhart-Thornley secondary electron detector and a solid state backscattering detector, available at the Great Lakes Institute for Environmental Research (GLIER) at our University of Windsor with

the assistance of the resident technician Mrs. Sharon Lackie. The instrument is illustrated in Figure 2.4.

2.3. Atomic Force Microscopy

Atomic force microscopy (AFM) is a relatively new technique to explore matter at the nanoscale.^[18] At present it is the most popular variant of the scanning probe microscopy (SPM) techniques. It is unique in the fact that it does not employ conventional optics and lenses to acquire images, but instead it employs a scanning probe that runs over the surface and gives account of the features found in it. The AFM was invented in 1985 and its description was published in 1986.^[19] Its name comes from the fact that it was designed to study matter at the *atomic* and molecular scale by studying the *forces* between the probe and the surface.

In general terms, the probe consists of a rectangular surface. On a side of this surface, a small piece is placed called *cantilever*, which is fabricated in different ways according to the mode used by the microscope. In the apex of the cantilever we find a tip, nanometrically sharp, facing downwards. This tip makes contact with the sample. A laser beam is directed to the cantilever zone located behind the tip (which faces upwards) and the reflection of the laser gets to a photodetection zone, usually a photodiode array. Then the probe is moved across the sample in a sweeping movement (*scan*) and the variations in the reflection of the laser beam, caused by the deflection of the cantilever, account for the features in the surface.

The principle described here may sound really simple, and it is, but its application for nanoscale research with the invention of *piezoelectric materials*, that is, a material that can change its volume when different electrical potentials are applied (or vice versa, that generates a potential when compressed). By applying very small variations in the electric potentials, the movement generated to perform the sweeping movement can be very small, thus making the microscope very sensitive, all the way to the nanoscale.

The scanning process usually proceeds in two major ways, namely *contact* and *tapping* mode. *Contact mode* is, as its name suggests, characterized by the tip being in an almost

perfect contact with the surface at all times when scanning, while recording the height and cantilever deflection and producing a 3D map of the sample. As a general rule, to add a better support, contact mode cantilevers usually have a triangular shape.

In *tapping mode*, the probe is made to oscillate at near its resonance frequency (the frequency at which the oscillation amplitude is maximum) and when scanning, the tip is in intermittent contact with the sample, in a “tapping” fashion. The instrument is tuned to the oscillation frequency in such a manner that the instrument will record when the tip is in contact with the sample. Tapping mode cantilevers need to be more flexible and therefore they are usually linear for high-frequency operation.

The major advantage of the technique is that unlike in electron microscopy, the sweeping method that gives the height produces a fully 3D map of the surface being scanned, thus giving an insight not possible with other techniques. Plus, for most applications it does not require any vacuum; the measurements are routinely done at room temperature and pressure, and with an accessory fluid cell, the measurements can even be performed in a liquid environment (thus allowing the measurements to be studied as a function of pH). Another advantage is the possibility of employing the AFM in what is called *ramping mode*, that is, no X-Y movement but only Z (up and down) movement; this allows to study the small forces between the tip and the surface (as variations in the expected cantilever deflection) in a technique called *force spectroscopy*.*[20]

* The name is somewhat misleading as it does not really involve interaction between light and matter, but this is the name that has prevailed in the literature.



Figure 2.5. Nanoscope IV scanning probe microscope

The major disadvantages of AFM have to do with the fact that the 3D image generated only represents what the sharp tip can sense; and tips cannot be perfectly sharp, or have no width. If the surface has a hole where the tip cannot sink perfectly, the shape of the hole will be distorted. A similar situation happens for steep walls, the steepness cannot be fully resolved. There is also the fact that the scanning can be affected by hysteresis (especially when scanning areas of $1 \mu\text{m}^2$ or less). Sometimes also the tip picks up debris in the surface that becomes permanently attached to the tip, and all images taken after that point will be distorted taking the shape of the impurity attached, thus producing artifacts. In general, the scanning takes way longer than in SEM, and therefore the image capturing process is longer.

Used for this thesis work: AFM images employed for the characterization of particles in Chapter 3 were collected using a Digital Instruments Nanoscope IV scanning probe microscopy instrument in our laboratory, illustrated in Figure 2.5. This instrument is a tube-scanning instrument, which means that the cantilever actually stays immobile over the surface, and it has a replaceable piezo-scanner where the sample is mounted, and that is the part that actually moves in contrary movement to what one expects it, so it can simulate that it is the tip moving across the surface.

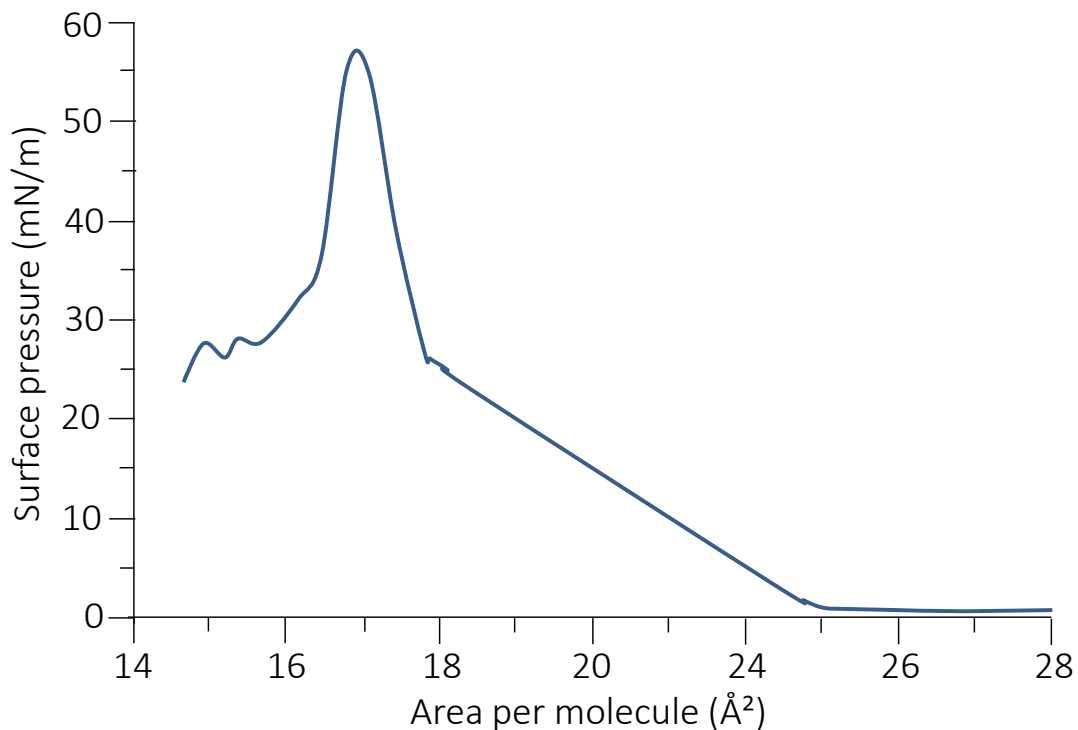


Figure 2.6. Surface pressure-area isotherm for arachidic acid

2.4. Langmuir-Blodgett Filmmaking

Langmuir-Blodgett (LB) films are films of organic molecules (especially fatty acids) that can be one molecule-thick, an LB monolayer. The physics that led to their discovery was developed by Irving Langmuir, after whom they are named.^[21,22] But it was Langmuir's research associate Katharine Blodgett who invented a device to transfer Langmuir films to solid substrates like glass.

2.4.1. Theory

When an amphiphilic substance (that is, one that has a hydrophilic side and a hydrophobic side) is placed on the surface of water, the molecules arrange in a fashion that the hydrophilic moiety faces down, towards the water, and the hydrophobic side faces upwards, in contact with the air above it. Also, the molecules spread all over the surface of the water, extending the coverage as much as possible. If there are enough molecules, they will form a layer that is exactly one-molecule thick, also called a *monomolecular layer*, or

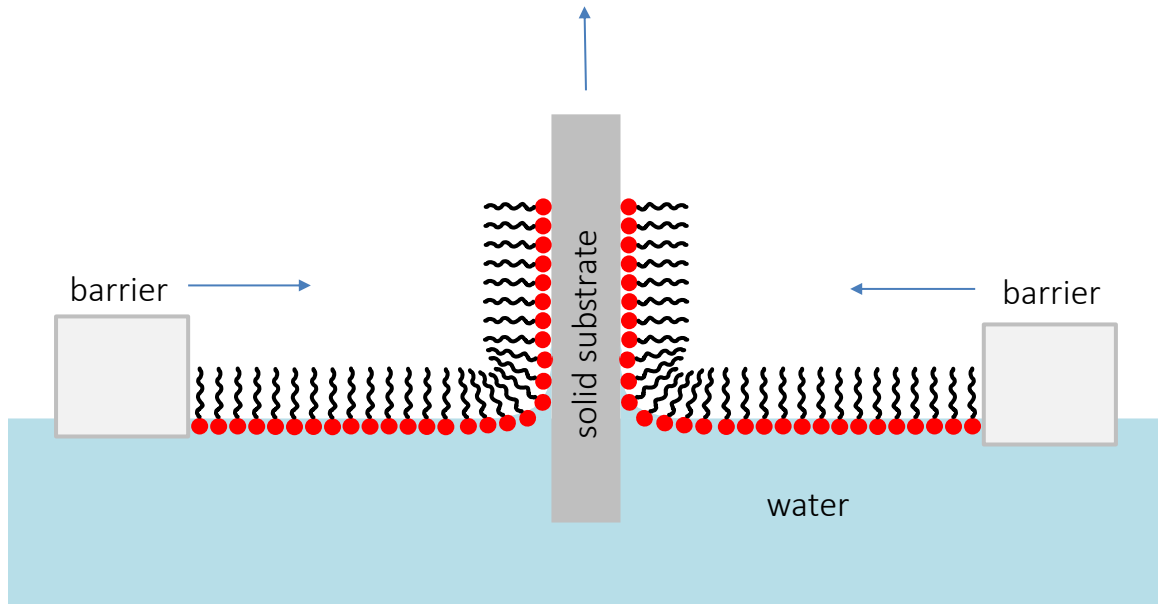


Figure 2.7. Z-deposition to a glass slide.

by contraction, a *monolayer*. If there is less than a monolayer-like coverage, the molecules bounce trapped in the surface of the water. Water is usually employed to fill the device (usually a trough), but it can be other substances; the filling liquid is called the *subphase*. The bouncing molecules in the surface move and exert a “pressure” over the boundaries of the surface, this is called surface pressure (Π).

Back in the 1930’s, Katharine Blodgett devised an instrument to transfer these monolayers to substrates, by measuring and keeping the surface pressure constant, using a trough that employed a barrier, which moved at the same speed. So, the surface area is reduced when the barrier is moved, and from there, the area per molecule is calculated by knowing exactly how much substance is added in terms of number of molecules $N_{\text{molecules}}$, starting from the concentration of the solution that is spread on the subphase:

$$c = \frac{N_{\text{molecules}}}{N_A V_{\text{spread}}} \quad (2.1)$$

where N_A is Avogadro’s constant and V_{spread} is the volume that has been spread. Once the amphiphilic fatty acid is added (dissolved in a volatile solvent that is later made to evaporate), the barriers are compressed, packing the molecules of fatty acid in the surface. If we measure the surface pressure as we compress and plot surface pressure versus area per molecule, we obtain a graph that is characteristic when temperature is conserved,

therefore it is called an *isotherm*, and a typical isotherm for arachidic acid is shown in Figure 2.6. As compression proceeds, the diagram goes through three major regions, namely one where the molecules are very sparse, which is called the gas-like phase, then one where the molecules are more packed (a liquid-like phase), and then one even more packed, with an even higher slope, that allows for little to no movement of the molecules (solid-like phase). This last one is that which we desire, but in order to know the correct surface pressure we must plot the isotherm first. Once the surface pressure is known, the next step is to produce a Langmuir film on the water surface and transfer it into a solid substrate, usually glass.

The most common way to proceed when one wants just one monolayer is to dip the substrate into the water, spread the amphiphiles on top, compress to the desired surface pressure, and then start pulling the substrate up while at the same time compressing with the barriers to keep the surface pressure constant. This is illustrated in Figure 2.7 and is called Z-deposition. It is possible to deposit only when the substrate is dipped and being compressed, that would be an X-deposition. When a bilayer is produced by combining the two processes above, a Y-deposition is obtained.

2.4.2. Mixed LB films

Dr. Aroca's group pioneered the use of LB films for ultrasensitive analysis since the 1980s, having become their signature technique. The mixed monolayers are mixtures of commonly a fatty acid and Raman and/or fluorescence probes (most of the time dyes) in well-known concentrations and ratios, in such a manner that the area per molecule, and the number of molecules per area are always well known, thus allowing for the validation of the claims for single-molecule detection. In our case, the fatty acid molecule is arachidic acid, which has a very well-known area per molecule of 25 \AA^2 .^[23] Knowing that, and assuming monolayer coverage, it is possible to calculate how many molecules are there in a given surface area, say, 1 \mu m^2 (4,000,000 molecules). Now, if we add a dye mixed at a given ratio to the arachidic acid, it is possible to calculate approximately the number of molecules of dye per surface area as expressed in Table 2.1.

Ratio	Approx. no. of molecules per 1 μm^2	
	Dye	Arachidic acid
1:1	2,000,000	2,000,000
1:10	363,637	3,636,363
1:100	39,604	3,960,396
1:1000	3,996	3,996,004
1:40,000	100	3,999,900
1:400,000	10	3,999,990
1:4,000,000	1	3,999,999

Table 2.1. Probe molecule to fatty acid ratio with the approximate number of molecules

Used for this thesis work: All LB films employed for the work presented in this thesis were made using the Nima film balance, model 302M, with dimensions 414x70 mm², illustrated in Figure 2.8. This instrument is computer-controlled.



Figure 2.8. Nima 302M LB film balance.

2.5. Spectroscopy Instrumentation

2.5.1. Raman and Fluorescence Microscope

All Raman and fluorescence spectra presented in this thesis were collected using the Renishaw inVia™ Raman microscope in our laboratory illustrated in Figure 2.9.

The instrument is built by attaching a microscope (Leica DMLM) to the Renishaw spectrometer. Samples are usually mounted on standard microscope slides, and put into focus through the microscope objectives. For measurements, the incident laser light is directed through the objectives and focused in the sample. The Raman or fluorescence radiation coming out of the sample is captured by the same objective and directed into the spectrometer in the opposite direction; that is, the measurements proceed in a backscattering geometry (180°).

When it becomes necessary to measure liquids in cuvettes, a special macro adapter is employed instead (pictured in Figure 2.9). Quartz cuvettes are employed in this case.



Figure 2.9. Renishaw inVia Raman microscope

To explain it in simple terms, we will divide the instrument in three parts: the optics for light delivery, light dispersion and detection. For light delivery, the instrument employs the microscope part. Inside the spectrometer, the Raman or fluorescence light going in needs to be separated from the laser light; this is achieved using a filter called a *beamsplitter*. Then, since the Rayleigh-scattered light is too powerful, it is blocked using another filter, appropriately named Rayleigh filter. There are two types of Rayleigh filters, namely, ones called *notch* filters, and other called *edge* filters. If we make a graph of light allowed versus wavelength, we see that notch filters block only a small section of the visible spectrum (making a “notch”), while edge filters block everything from a certain wavelength downwards or upwards (a kind of “edge”).

The detection device does not discriminate by wavelength, it just counts photons, so light must be diffracted to obtain a spectrum. So after the Raman or fluorescence light crosses the Rayleigh light filter, it goes through a diffraction grating which is a crystal with many grooves. The shorter the wavelength, the more grooves per unit of length are required to produce a good separation of wavelengths. In our case, we employ two diffraction gratings, one with 1800 grooves per millimetre, and one with 1200 grooves per millimetre (for our 785 nm laser).

The diffraction grating sends the light to different parts of the detection device, which is a charge-coupled device (CCD). This is a camera-like device that generates electric charges when light hits it. The CCD within our inVia instrument has an area of 516×516 pixels. Also, in order to eliminate thermal dark currents (which would give false readings of light) the device is cooled thermoelectrically[†] to -70°C .

2.5.2. Lasers

The Renishaw inVia spectrometer needs external lasers to excite the sample. In our laboratory we have three of them, with three different wavelengths, as detailed in Table 2.2 below:

[†] Also said to be Peltier-cooled as it uses the Peltier effect

Laser type	Wavelength (nm)	Power (mW)
Argon-ion	514.5	18
Helium-neon (HeNe)	632.8	16
Photodiode	785	18

Table 2.2. List of lasers and their wavelength and power

Gas lasers like the argon-ion 514.5 nm are well suited for Raman measurements because they are highly monochromatic, that is, the variation in wavelength is minimal. Their main disadvantages are that they are large and consume much power. They not only produce the wavelength they are characterized by, but they also produce light in several other wavelengths although in less intensity. In order to prevent that these additional laser lines cause more Raman scattering, an optical filter is placed at the gate of the laser, which is called a *plasma line rejection filter* (PLRF).

2.5.3. UV-visible Absorption Spectrometer

All absorption spectra presented in this thesis were collected using the Varian Cary 50 instrument in our laboratory illustrated in Figure 2.10. It has a double-beam setup and has an effective measurement range between 190 and 1100 nm, and it is equipped with a durable xenon flash lamp.

2.6. Computational Resources

2.6.1. Computational Chemistry

It is said that *theoretical chemistry* is the mathematical description of chemistry, and *computational chemistry* is when those mathematical methods are sufficiently well developed to be automated by their implementation in a computer program. A comprehensive description of computational chemistry can be found in the excellent books



Figure 2.10. Varian Cary 50 UV-vis spectrometer

by Young^[24] and Jensen^[25] as well as Wenjuan Huang's Ph.D. thesis^[26] in the Department of Chemistry at the University of Windsor.

In this work, like most authors using IR and Raman spectroscopy, what we want to do when performing this type of calculations is to make a good assignment of the Raman bands, by comparing the experimental data to that predicted by theory.

Used for this thesis work: To assign the Raman/SERS bands coming from the experiments described in Chapter 3 and the additional calculations of Chapter 6, we performed quantum mechanical calculations using the computational chemistry software Gaussian 09^[27] (Gaussian, Inc.) running in clusters from the Shared Hierarchical Academic Research Computing Network (SHARCNET)[‡] of Canada using up to 2 gigabytes (as shared memory) and up to 8 processors at a time. In every case, we performed geometry optimization followed by frequency calculations, at the levels of theory described in section 3.2 of Chapter 3, and section 6.2 of Chapter 6.

Molecular models for the optimized geometries were drawn using the ACD/Chemsketch Freeware program, and later to converted to Gaussian 09 input text, and

[‡] We employed the supercluster for the Gaussian User Group, "Saw". Full specifications of the system can be found at the website www.sharcnet.ca.

the Gaussian output was read with the assistance of the GaussView 5.09 (Gaussian Inc.) program, which we also employed to generate the images of the calculated spectra. No scaling factor corrections were made. Additional lines to employ effective core potentials were added manually with text editors (Vim, Notepad++).

2.6.2. Other Software

Experimental Raman and fluorescence spectra were obtained using the Renishaw WiRE 3.2 software that controls the inVia microscope, and these spectra were later further processed using the Thermo Galactic GRAMS 8.00 software. This software allows for baseline correction, offset correction, smoothing, curve fitting and, by importing the displayed spectra into Microsoft PowerPoint, was used for the elaboration of most of the figures that display spectra.

2.7. References

1. Daniel, M.-C.; Astruc, D. *Chem. Rev.* **2004**, *104*, 293.
2. Turkevich, J.; Stevenson, P. C.; Hillier, J. *Discuss. Faraday Soc.* **1951**, *11*, 55.
3. Enüstün, B. V.; Turkevich, J. *J. Am. Chem. Soc.* **1963**, *85*, 3317.
4. Frens, G. *Nature, Phys. Sci.* **1973**, *241*, 20.
5. Li, G.; Lauer, M.; Schulz, A.; Boettcher, C.; Li, F.; Fuhrhop, J.-H. *Langmuir* **2003**, *19*, 6483.
6. Lee, P. C.; Meisel, D. *J. Phys. Chem.* **1982**, *86*, 3391.
7. Linnert, T.; Mulvaney, P.; Henglein, A.; Weller, H. *J. Am. Chem. Soc.* **1990**, *112*, 4657.
8. Leopold, N.; Lendl, B. *J. Phys. Chem. B* **2003**, *107*, 5723.
9. Jana, N. R.; Gearheart, L.; Murphy, C. J. *Chem. Commun.* **2001**, 617.
10. Nikoobakht, B.; El-Sayed, M. A. *Chem. Mater.* **2003**, *15*, 1957.
11. Ali, M. R. K.; Snyder, B.; El-Sayed, M. A. *Langmuir* **2012**, *28*, 9807.
12. Stöber, W.; Fink, A.; Bohn, E. *J. Colloid Interface Sci.* **1968**, *26*, 62.
13. Liz-Marzán, L. M.; Giersig, M.; Mulvaney, P. *Langmuir* **1996**, *12*, 4329.
14. Liz-Marzán, L. M.; Giersig, M.; Mulvaney, P. *Chem. Commun.* **1996**, 731.
15. Li, J. F.; Huang, Y. F.; Ding, Y.; Yang, Z. L.; Li, S. B.; Zhou, X. S.; Fan, F. R.; Zhang, W.; Zhou, Z. Y.; Wu, D. Y.; Ren, B.; Wang, Z. L.; Tian, Z. Q. *Nature* **2010**, *464*, 392.

16. Bozzola, J. J.; Russell, L. D. *Electron Microscopy: Principles and Techniques for Biologists*; 2nd. ed.; Jones and Bartlett: Sudbury, MA, 1999.
17. *Electron Microscopy: Principles and Fundamentals*; 1st ed.; Amelinckx, S.; van Dyck, D.; van Landuyt, J.; van Denteloo, G., Eds.; VCH Verlagsgesellschaft mbH: Weinheim, Germany, 1997.
18. Yongho, S.; Wonho, J. *Rep. Prog. Phys.* **2008**, *71*, 016101.
19. Binnig, G.; Quate, C. F.; Gerber, C. *Phys. Rev. Lett.* **1986**, *56*, 930.
20. Guerrero, A. R.; Caballero, L.; Adeva, A.; Melo, F.; Kogan, M. J. *Langmuir* **2010**, *26*, 12026.
21. Martin, P.; Szablewski, M. *Langmuir-Blodgett Troughs, Operating Manual*; 6th ed.; Nima Technology Ltd.: Coventry, England, 2004.
22. Petty, M. C. *Langmuir-Blodgett films: an introduction*; 1st ed.; Cambridge University Press: Cambridge, England, 1996.
23. Constantino, C.; Duff, J.; Aroca, R. *Spectrochim. Acta A* **2001**, *57*, 1249.
24. Young, D. C. *Computational Chemistry: A Practical Guide for Applying Techniques to Real-World Problems*; 1st. ed.; John Wiley & Sons: Chichester, England, 2001.
25. Jensen, F. *Introduction to Computational Chemistry*; 2nd. ed.; John Wiley & Sons.: Chichester, England, 2007.
26. Huang, W. J. Computational Investigations into Carbohydrate-Related Biochemistry. Ph.D. Dissertation, University of Windsor, Windsor, Ontario, 2012.
27. Frisch, M. J.; Trucks, G. W.; Schlegel, H. B.; Scuseria, G. E.; Robb, M. A.; Cheeseman, J. R.; Scalmani, G.; Barone, V.; Mennucci, B.; Petersson, G. A.; Nakatsuji, H.; Caricato, M.; Li, X.; Hratchian, H. P.; Izmaylov, A. F.; Bloino, J.; Zheng, G.; Sonnenberg, J. L.; Hada, M.; Ehara, M.; Toyota, K.; Fukuda, R.; Hasegawa, J.; Ishida, M.; Nakajima, T.; Honda, Y.; Kitao, O.; Nakai, H.; Vreven, T.; J. A. Montgomery, J.; Peralta, J. E.; Ogliaro, F.; Bearpark, M.; Heyd, J. J.; Brothers, E.; Kudin, K. N.; Staroverov, V. N.; Kobayashi, R.; Normand, J.; Raghavachari, K.; Rendell, A.; Burant, J. C.; Iyengar, S. S.; Tomasi, J.; Cossi, M.; Rega, N.; Millam, J. M.; Klene, M.; Knox, J. E.; Cross, J. B.; Bakken, V.; Adamo, C.; Jaramillo, J.; Gomperts, R.; Stratmann, R. E.; Yazyev, O.; Austin, A. J.; Cammi, R.; Pomelli, C.;

Ochterski, J. W.; Martin, R. L.; Morokuma, K.; Zakrzewski, V. G.; Voth, G. A.; Salvador, P.; Dannenberg, J. J.; Dapprich, S.; Daniels, A. D.; Farkas, Ö.; Foresman, J. B.; Ortiz, J. V.; Cioslowski, J.; Fox, D. J.; Revision C.01 ed.; Gaussian, Inc.: Wallingford, CT, 2010.

Chapter Three

Surface-Enhanced Raman Scattering of Hydroxyproline

The work presented in this chapter has been published by the author in the Journal of Raman Spectroscopy, in April 2012 under the same title.^[1] This material has been adapted from that paper with permission* from John Wiley & Sons (see *Permissions Obtained for Published Copyrighted Materials* section, page 154.)

3.1. Introduction

Surface-Enhanced Raman Scattering (SERS) of amino acids has proven a difficult task. The SERS of biomolecules and the formation of a reliable (reproducible) SERS database for biomedical applications has shown to be a very challenging task for two reasons: First, the functional groups in proteins, lipid and sugars do not usually include aromatic moieties or chromophores absorbing in the visible (with intrinsic very large Raman cross sections), and therefore, large average enhancement factors are needed for ultrasensitive analysis. Second, the biomolecule-metal surface interaction leads to active surface photochemistry, photoisomerisation or photodissociation, thus hindering the reproducibility of the experiment. SERS measurements on silver colloids or silver surfaces lead to spectra showing this phenomenon.^[2,3]

In this work, we have developed an analytical protocol to obtain reproducible SERS spectra of 4-hydroxyproline (Hyp). Hydroxyproline is a non-essential amino acid, found in proteins like collagen, and its presence in proteins is the result of post-translational modification of proline. There are few studies of the vibrational spectroscopy of

* © 2012 John Wiley and Sons.

hydroxyproline. The Raman spectrum has been reported in a computational study and vibrational assignment of hydroxyproline in solid samples by Tarakeshwar and Manogaran^[4]. István et al.^[5] reported Raman and SERS of hydroxyproline as part of study of several amino acids in thin layer chromatography spots. The authors qualified their findings by saying: *“It is shown, however, that due to severe adsorption-induced spectral distortions and increased sensitivity to microscopic inhomogeneity of the sample, none of the SERS spectra obtained with the dispersive Raman microscope operating in the visible region were superior to the best NIR normal FT-Raman spectra, as far as sample identification is concerned.”*^[5] Shortly after the publication of our present work at the Journal of Raman Spectroscopy, another study on proline and hydroxyproline was published by Cárcamo and collaborators.^[6] This and our work are the only literature published about the SERS of Hyp.

The problem of lack of reproducibility of the SERS spectra of amino acids in the visible region using silver is illustrated in the work of Aliaga et al.^[2,3] In our own laboratory, we have used several Ag nanostructures (colloids, silver island films and commercial substrates) pursuing SERS of several amino acids and we encounter the same problems reported in the literature.

In this investigation, the problem of SERS reproducibility is solved for Hyp using gold colloids instead of silver, avoiding reactivity on Ag which leads to photodissociation products, and also removing the colloid stabilizers to improve the adsorption of the molecule to the nanostructures. This gave a short colloid lifetime, but long enough to carry out a SERS experiment. The outline of the chapter is as follows. First, a complete assignment of the vibrational Raman spectrum is given using spectra in the solid state and in solution (at different pH values) supported by computational studies. A partially deuterated compound (trans-4-hydroxyproline-2,5,5-d₃) was also studied to help vibrational interpretation and make a more complete study. Second, the SERS spectra obtained on Au colloids is presented and supported by computations including one Au⁺ ion interacting with the Hyp molecule.

3.2. Materials and Methods

L-4-Hydroxyproline was purchased from Fluka and used without further purification. The deuterated analogue (trans-4-hydroxyproline-2,5,5-d₃, d-Hyp) was purchased from CDN Chemicals and also used as received. All solutions were made using Milli-Q water. The concentration of the amino acid stock solution to mix with the colloid was 10⁻³ M. AFM images of the colloidal particles immobilized over a glass substrate were obtained with the Digital Instruments Nanoscope IV described in section 2.3, under tapping mode, using an aluminum-coated n⁺-silicon tip (Mikromasch, Inc.). Samples were prepared by treating a glass slide (cut to approx. 8 × 8 mm) with a diluted poly-L-lysine solution for 30 minutes, air-dried, and subsequently a droplet of the colloidal solution was applied and we waited for another 30 minutes, then rinsed and air-dried.

Gold colloids were synthesized by modifying Lee and Meisel's standard borohydride reduction procedure.^[7] Briefly, we prepared 20 mL of a 5 × 10⁻³ M potassium tetrachloroaurate (KAuCl₄, Sigma-Aldrich), stirred into an ice bath, and then very slowly poured 60 mL of an ice-cold 2 × 10⁻³ sodium borohydride (NaBH₄) solution. No stabilizing agent was employed. Next, equal parts of the colloidal solution and the amino acid solution were mixed so the final concentration of the amino acid in the colloid was 5 × 10⁻⁴ M. The resulting colloid had a lifetime of around 2 hours before collapse in the cuvette, which was the allocated time to perform the Raman measurements. After that, the colloid was concentrated by centrifugation at 14,000 rpm for 7 minutes, and the sediments were collected for Raman measurements.

Absorption spectra were recorded using the Cary 50 UV-vis spectrometer described in section 2.5.3. Raman spectra were recorded from our Renishaw inVia Raman microscope described in section 2.5.1 using the excitation of the 514.5, 632.8 and 785 nm laser lines. The measurements in aqueous solution were performed in a quartz cuvette using the optics adapter described in that section. For the measurements of 1 M aqueous solutions, we just placed 1 mL of the solution in the quartz cuvette. For the measurements of colloidal dispersions, the cuvette was washed with *aqua regia* and copious water between every measurement. Calculated Raman spectra and geometry optimizations were obtained using

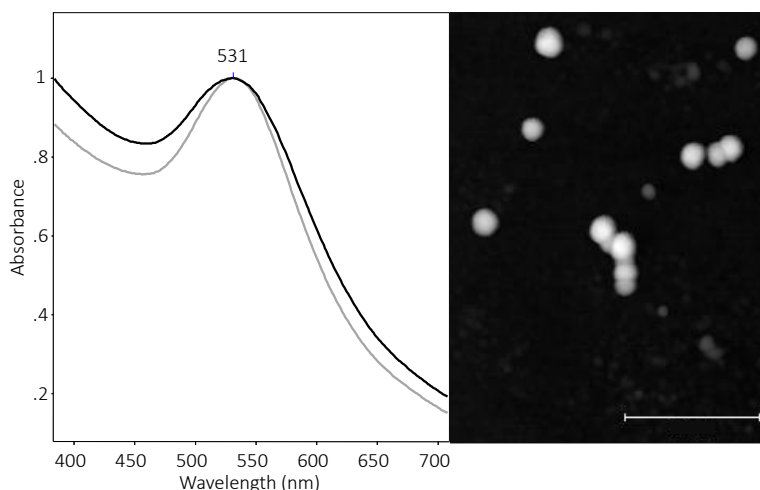


Figure 3.1. Absorption spectrum and AFM image of the particles. The white bar in the image represents 500 nm.

the Gaussian 09^[8] suite of programs, using density functional theory at the B3LYP/aug-cc-pVTZ level of theory using the default solvation model (polarizable continuum model) with water as solvent, and in the case of the calculations using gold ions, we used the LANL2DZ basis set, with effective core potentials for the core electrons in the gold ion. No scaling factor correction was employed. Molecular models for the optimized geometries were obtained using the GaussView 5.0 program.

3.3. Results and Discussion

Typical plasmon absorption spectra of the colloids are shown in Figure 3.1. In the sample results for the colloids shown in the figure the maxima are located at 531 nm for both the bare colloid and that with Hyp dissolved. In the many repetitions of the experiment following the same procedure, the absorption maxima of the synthesized colloid varied between 530 and 531 nm. Because of the unstable nature of the colloid, the experiment had to be repeated many times in order to obtain meaningful results. It is possible to see that the incorporation of the amino acid into the colloidal solution causes a decrease in the bandwidth of the plasmon. While here we show a single pair of absorption spectra, this observation was seen in every replication of the experiment, without noticing a significant shift in the placement of the absorption maximum. The colloidal particles were further characterized by atomic force microscopy measurements, as shown in the right

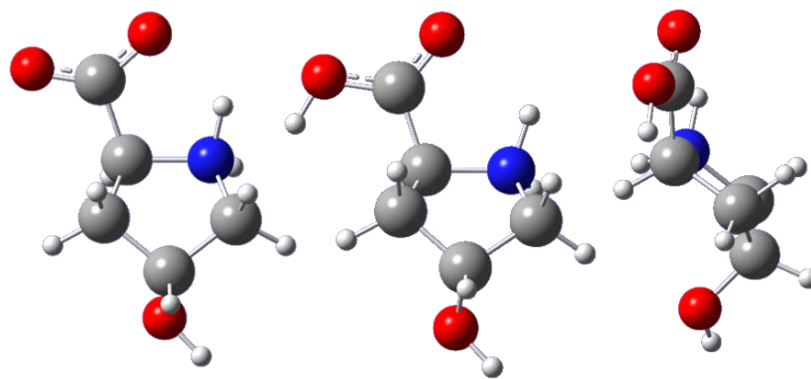


Figure 3.2. Optimized conformations for Hyp.
Zwitterion (left), neutral form (centre) and protonated form (right)

side of Figure 3.1. Particle diameters between 50 and 80 nm were observed, with approximately round shapes. Geometrical configuration of the molecules after optimization is shown in Figure 3.2. The neutral form of Hyp is also shown in its zwitterionic form, which given the pKa values for Hyp (1.94 for the carboxylic, 9.73 for the amino group)^[9] which is the most likely configuration at neutral pH. Due to the acid pH of the gold colloid solution, the amino acid may be found in a protonated form, and for that reason we also performed calculations for that protonated configuration.

In a theoretical and experimental study of proline, Kapitán *et al.*^[10] showed that there are two major conformers for the proline ring, the main difference being the orientation in which the ring is bent, and it can be seen that the conformer of less energy is that oriented with the aliphatic portion of the ring bent in the opposite direction to the carboxylate. It was reasonable to assume a similar configuration for Hyp, with the 4-hydroxyl and the carboxylate in opposite sides of the ring plane, and this is the configuration to which we performed the optimization, as can be seen in Figure 3.2. We also performed the calculation using the alternative configuration but it has a higher energy (data not shown)

Raman spectra for Hyp are shown in Figure 3.3. Calculated spectra are shown for the neutral and for the protonated form of Hyp (a and b). The normal Raman spectra of Hyp in solid and in solution at neutral pH show similar bands, and are consistent with a zwitterionic configuration for the neutral molecule.

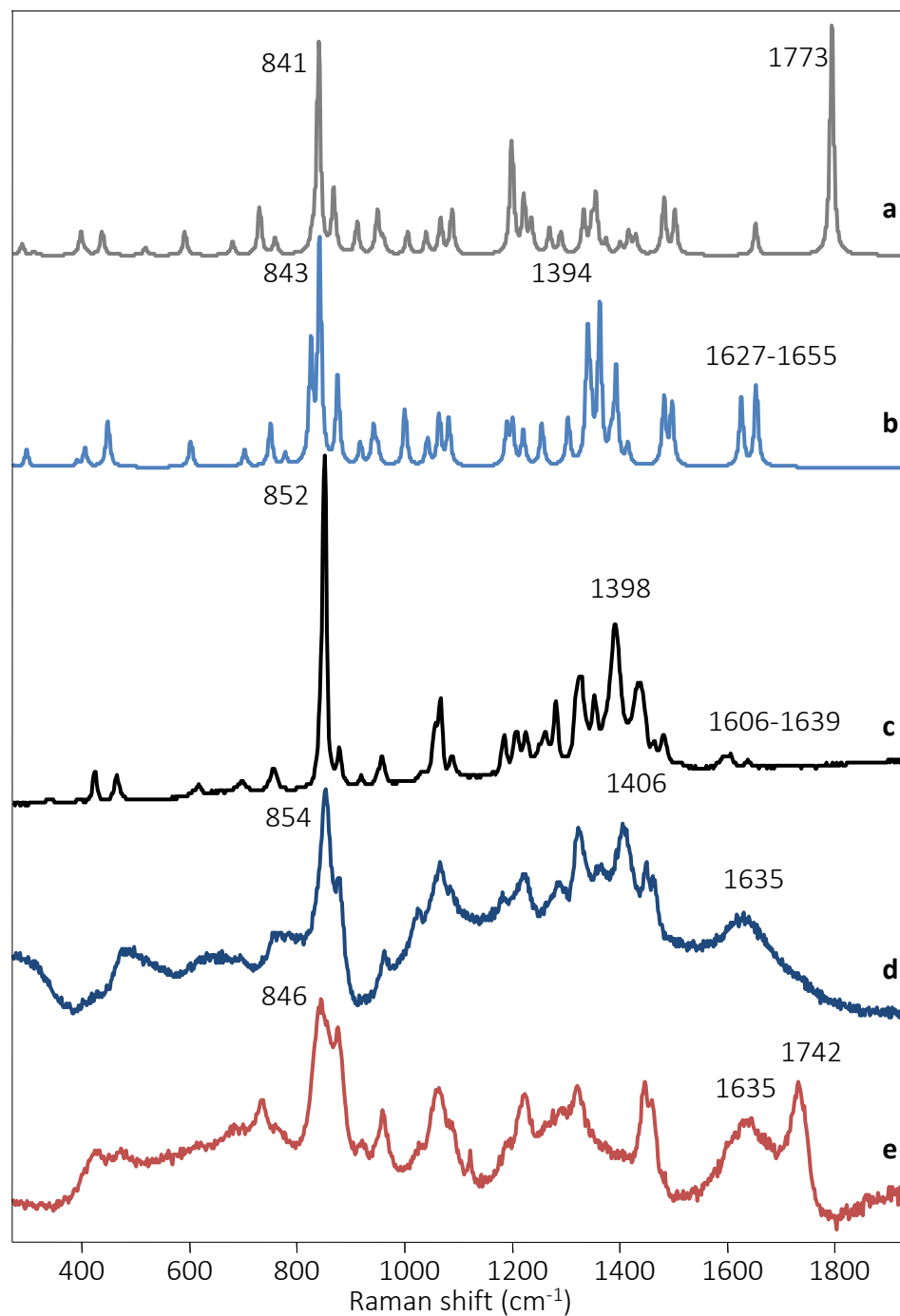


Figure 3.3. Calculated and experimental Raman spectra for Hyp.
 a) Calculated Raman spectrum for the protonated form of Hyp; b) calculated Raman spectrum for the neutral form of Hyp; c) normal Raman spectrum of solid Hyp (LL = 514.5 nm); d) normal Raman spectrum of a 1 M solution of Hyp at neutral pH (LL = 514.5 nm); e) normal Raman spectrum of a 1 M solution of Hyp at pH = 1 (LL = 514.5 nm).

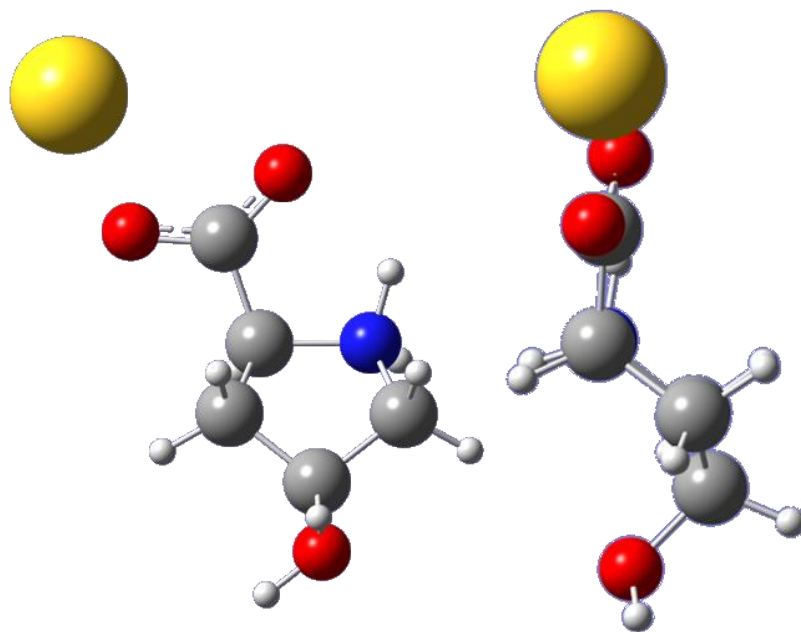


Figure 3.4. Optimized conformation for Hyp with one Au⁺ ion

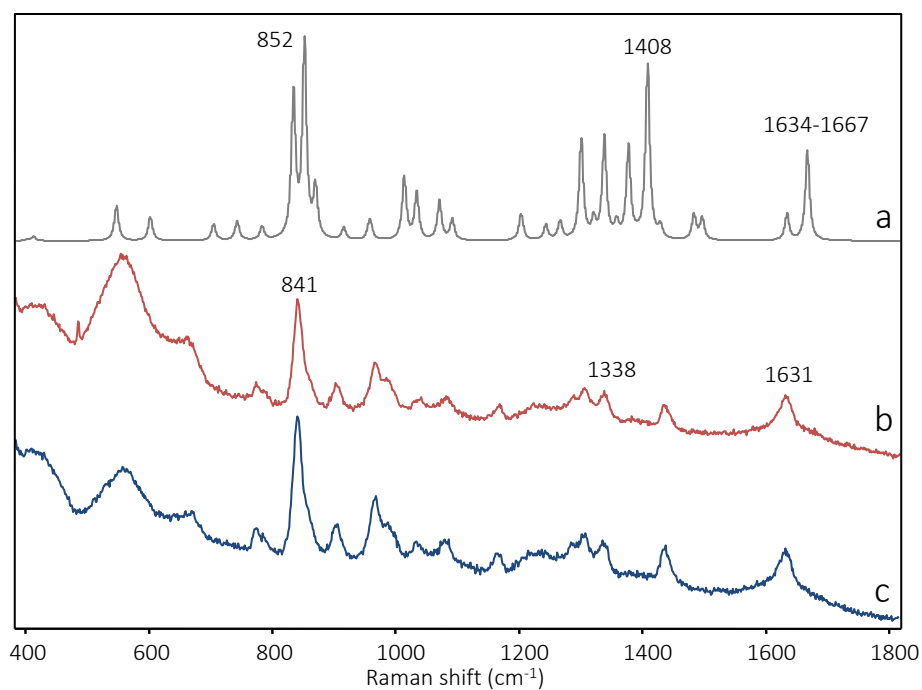


Figure 3.5. Calculated and experimental SERS spectra.
 a) Calculated spectrum of Hyp with one Au⁺ ion added. b) and c),
 experimental SERS spectra of Hyp in gold colloids, at a concentration of
 5×10^{-4} M, two replicas of the experiment (LL=785nm)

Table 3.1. Band assignment for the normal, non-protonated Raman spectra.

Calculated frequency (cm ⁻¹)	Observed frequency in solid (cm ⁻¹)	Observed frequency in solution (cm ⁻¹)	Assignment
205			Ring vibration
264	257		OH bending
299	345		Ring bending
392	395		Ring bending
406			Ring bending
450	465	477	Ring vibration
604	618	619	Ring bending
704	698	696	Ring torsion and COO ⁻ symmetric stretching
752	757	757	Ring bending
779			Ring torsion and COO ⁻ symmetric stretching
827	852	854	Ring stretching
843			Ring stretching
877	879	878	Ring stretching
919	920		Ring stretching
943	959	964	Ring stretching
951			Ring stretching
1002	1035	1027	C-N stretching
1043	1058	1066	C-C stretching
1065	1066		C-C stretching
1083	1089	1088	C-C stretching
1191	1185	1182	CH and NH bending
1201	1208		CH ₂ , NH ₂ twisting and OH bending
1222	1225	1222	CH ₂ and NH ₂ twisting
1256	1262	1271	CH, NH and OH bending
1305	1325	1287	CH and NH bending
1339	1328	1324	CH and OH bending
1342			CH bending
1348			CH bending

1363	1353	1364	COO ⁻ symmetric stretching and NH, CH bending
1384	1392	1406	NH ₂ twisting, CH bending and CH ₂ wagging
1394			COO ⁻ symmetric stretching and CH bending
1415	1438		CH and OH bending
1483	1464	1450	CH ₂ scissoring
1498	1482	1486	CH ₂ scissoring
1627	1606	~1635	COO ⁻ antisymmetric stretching and NH ₂ scissoring
1655	1639		COO ⁻ antisymmetric stretching and NH ₂ scissoring
3071			CH stretching
3082	2864	2881	CH stretching
3104	2957	~2960	CH ₂ symmetric stretching
3118			CH stretching
3140	2987	2992	CH stretching
3161	2997		CH ₂ asymmetric stretching
3180			NH stretching
3518	3038	3038	NH stretching
3799	3137		OH stretching

Table 3.2. Assignment for the SERS spectra of Hyp

Calculated frequency (cm ⁻¹)	Observed frequency in solution (cm ⁻¹)	Assignment
273		Ring shaking
296		OH bending
308		NH ₂ bending and OH bending
403		Ring bending
413		Ring bending
548	560	Ring torsion and O-Au stretching
602		Ring bending
705		Ring torsion
743	774	Ring and carboxylate torsion
784	784	Ring and carboxylate torsion
835	841	Ring stretching
852		Ring stretching
870	~860	Ring stretching
916	904	Ring torsion
957		Ring stretching
960		Ring stretching
1014	967	Ring torsion
1034	987	Ring torsion
1071	1035	Ring torsion
1092	1080	Ring bending
1203	1166	CH, NH and OH bending
1205		CH ₂ twisting
1243	1219	Ring bending and CH ₂ twist
1266	1242	CH ₂ and OH bending
1301	~1265	CH ₂ wagging, CH bending and NH bending
1321		HCCH scissoring
1338	1285	HCCH rocking
1358		CH bending modes
1377	1306	NH bending
1391		NH ₂ and CH ₂ wagging

1408	1337	NH ₂ twisting and COO ⁻ symmetric stretching
1429		OH and CH bending
1484	1436	CH ₂ scissoring
1497		CH ₂ scissoring
1634	1634	NH ₂ scissoring
1667		NH ₂ scissoring and COO ⁻ antisymmetric stretching
3065		CH stretching
3074		CH stretching
3120		CH ₂ symmetric stretching
3127		CH stretching
3139		CH stretching
3180		CH ₂ antisymmetric stretching
3314		NH stretching
3503		NH stretching
3799		OH stretching

The calculated bands at 817 and 843 cm^{-1} , which correspond to the ring breathing modes, are seen to overlap in the experimental spectra giving one single strong peak at 852 cm^{-1} in the solid and at 854 cm^{-1} in the solution. The bandwidth also increases for the spectrum of Hyp in solution. This is due to the increased concentration. The peaks of the carboxylate can be clearly appreciated, namely the COO^- symmetric stretching at 1395 cm^{-1} in the solid and at 1408 cm^{-1} in the solution. The antisymmetric stretching can be clearly seen in the solution spectrum as the broad peak at 1632 cm^{-1} . The full band assignments for these spectra can be found in Table 3.1.

The normal Raman spectrum of Hyp in solution at pH 1 shows clearly the C=O stretching mode at 1742 cm^{-1} and does not show the peak at 1408 cm^{-1} , thus making clear the presence of the protonated form of the molecule. The ring breathing mode at 846 cm^{-1} is seen blue shifted with respect to the neutral form, but in general the same bands are seen.

For the assignment of the SERS spectra of Hyp we modeled the molecule including one Au^+ ion as shown in Figure 3.4, and the calculated spectrum is compared to the experimental SERS spectra in Figure 3.5. The two traces b) and c) correspond to two replicas of the experiment carried out at two different times, and they show exactly the same Raman bands thus proving the reproducibility of the method presented here.

The SERS spectra show distinctive bands of hydroxyproline. The pH of the colloidal solution is 2.93, so it would be expected to see an acidic configuration of the amino acid. However, the C=O stretching at 1742 cm^{-1} (which is seen in the Raman spectrum of the acidic 1 M solution) is not seen, and also the presence the COO^- antisymmetric stretching mode at 1631 cm^{-1} suggests that that the adsorption on the colloidal surface would be through the carboxylate moiety.

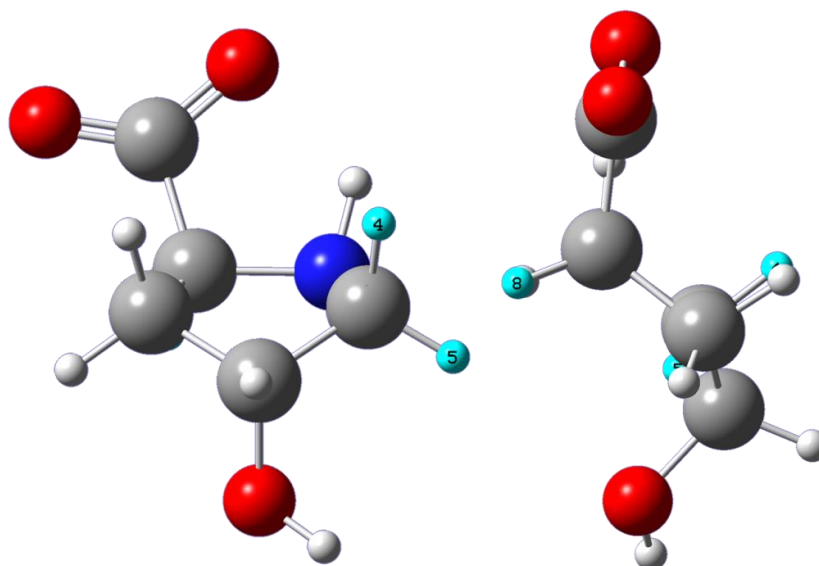


Figure 3.6. Optimized conformations for d-Hyp.

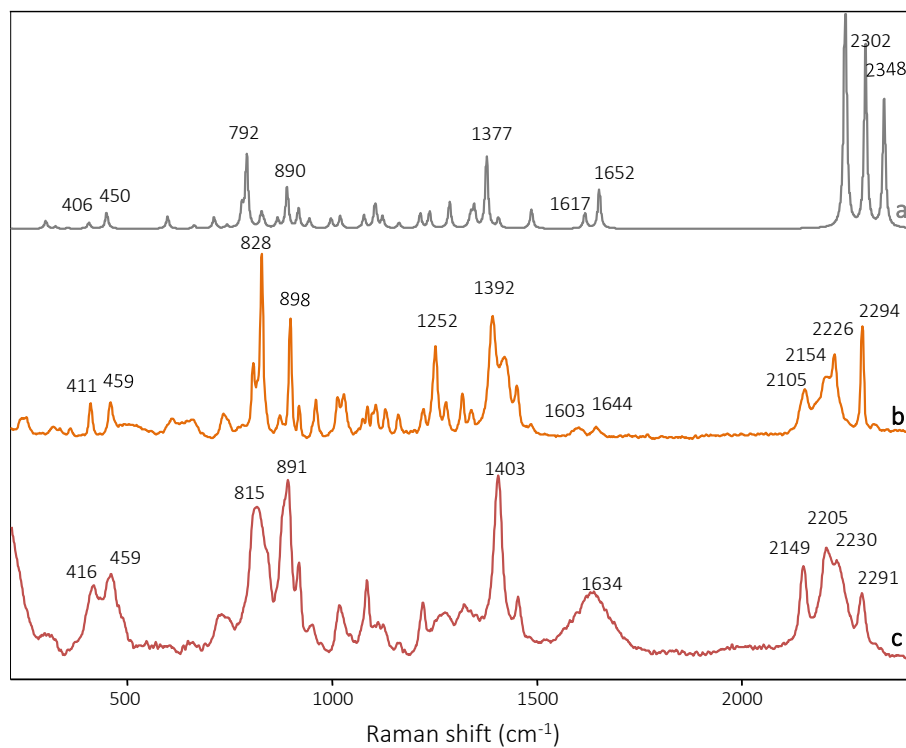


Figure 3.7. Calculated and experimental Raman spectra for d-Hyp. a) Calculated spectrum of Hyp with one Au^+ ion added. b) and c), experimental SERS spectra of Hyp in gold colloids, at a concentration of 5×10^{-4} M, two replicas of the experiment (LL=785nm)

Table 3.3. Assignment for the spectra of d-Hyp in solid and solution

Calculated frequency (cm ⁻¹)	Observed frequency in solid (cm ⁻¹)	Observed frequency in solution (cm ⁻¹)	Assignment
206	209		Ring vibration
301	319		OH and ring bending
325	334		OH bending
354	361		Ring bending
406	411	417	Ring bending
450	459	459	Ring bending and COO ⁻ torsion
599	609		Ring bending and COO ⁻ torsion
663	660		Ring torsion
712	736	727	Ring stretching and NH ₂ rocking
744	~780		Ring torsion and COO ⁻ symmetric stretching
780	807	815	Ring stretching
792	828		Ring stretching and COO ⁻ symmetric stretching
827			Ring stretching
833			Ring stretching and COO ⁻ symmetric stretching
867			Ring stretching
890	898	891	Ring stretching and CD ₂ twisting
918	920	917	C-C stretching
944	961	949	C-N stretching and CD bending
998	1014	1017	C-C stretching
1020	1029		C-N stretching
1078	1075,1086	1084	C-C stretching and ring bending
1104	1098,1107	1109	CH ₂ scissoring
1107			C-C α -N stretching
1123	1131	1123	Ring bending
1164	1162	1162	Ring torsion
1215	1222	1220	CH and OH bending
1238	1252		CH ₂ twisting
1287	1278	1274	NH bending
1336	1318	1322	NH and CH bending

1340			NH ₂ twisting, CH bending and OH bending
1347	1340	1404	COO ⁻ symm. stretching, CH bending and NH ₂ wag
1377	1392		COO ⁻ symm. stretching, CH bending and NH ₂ wag
1406	1421		CH and OH bending
1487	1451	1452	CH ₂ scissoring
1617	1601	1634	COO ⁻ antisymmetric stretching and NH ₂ scissoring
1652	1644		COO ⁻ antisymmetric stretching and NH ₂ scissoring
2253	2153	2150	CD ₂ symmetric stretching
2302	2203	2203	CD stretching
2348	2228	2234	CD ₂ antisymmetric stretching
3066	~2870	~2890	CH stretching
3078	2963	2967	CH stretching
3132	2993	3014	NH stretching
3134			CH ₂ antisymmetric stretching
3515	3144		NH stretching
3795	3294		OH stretching

The d-Hyp geometry optimization gives the configuration shown in Figure 3.6, and the corresponding Raman spectra are shown in Figure 3.7. Calculated spectra are shown for the zwitterionic neutral form of d-Hyp. The normal Raman spectra of d-Hyp in solid and in solution at neutral pH show similar bands, and are also consistent with a zwitterionic configuration. The calculated bands at 780 and 792 cm^{-1} , which correspond to the ring breathing modes, are seen to overlap in the experimental spectra giving one single strong peak at 828 cm^{-1} in the solid and at 815 cm^{-1} in the solution. The full width at half maximum increases for the spectrum in solution due to the high concentration of Hyp; this is consistent with previous investigations^[11,12]. The peaks of the carboxylate can be clearly seen, namely the COO^- symmetric stretching at 1392 cm^{-1} in the solid and at 1403 cm^{-1} in the solution. The antisymmetric stretching can be clearly seen in the solid at 1644 cm^{-1} and in the solution as the broad peak at 1634 cm^{-1} .

In the case of the d-Hyp, the spectra are slightly altered to the prediction in terms of the bands expected in the regions from 1100-1200 cm^{-1} and in the C-D region from 2100 to 2250 cm^{-1} . This is undoubtedly due to a partial N-deuteration in the purchased

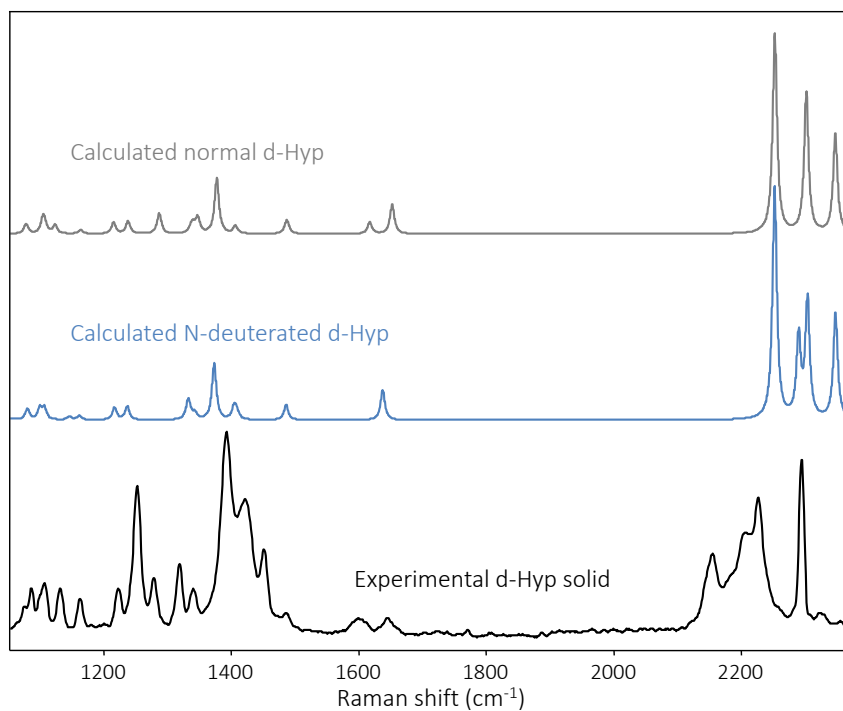


Figure 3.8. Additional calculations for d-Hyp compared to experiment. The experimental spectrum for d-Hyp shows elements seen in the calculations for both the N-deuterated and regular d-Hyp; the actual compound is only partially N-deuterated

deuterated analogue, thus causing extra peaks in the fingerprint region and one extra peak in the C-D region. An additional quantum mechanical calculation performed for the N-deuterated compound confirms this assumption, as shown in Figure 3.8.

To help the interpretation of the SERS spectra of the deuterated analogue, we modelled again this interaction using one Au⁺ ion, and the calculated spectrum in Figure 3.9 is compared to two replicas of the SERS experiment. We followed the same protocol as for normal Hyp.

The calculated spectrum is still useful in the prediction and interpretation of vibrational modes, although the agreement with experiment in terms of the band relative intensity is poor. However, that is expected since SERS relative intensities are modulated by surface selection rules and molecular orientation. Most important is the fact that repeated experiments showed little variations in the SERS spectrum, thus proving the method reproducible. The N-D and C-D stretching bands arising from a partial deuteration are clearly seen in the SERS spectrum. However, the C-H and N-H are very weak in the SERS spectrum of Hyp.

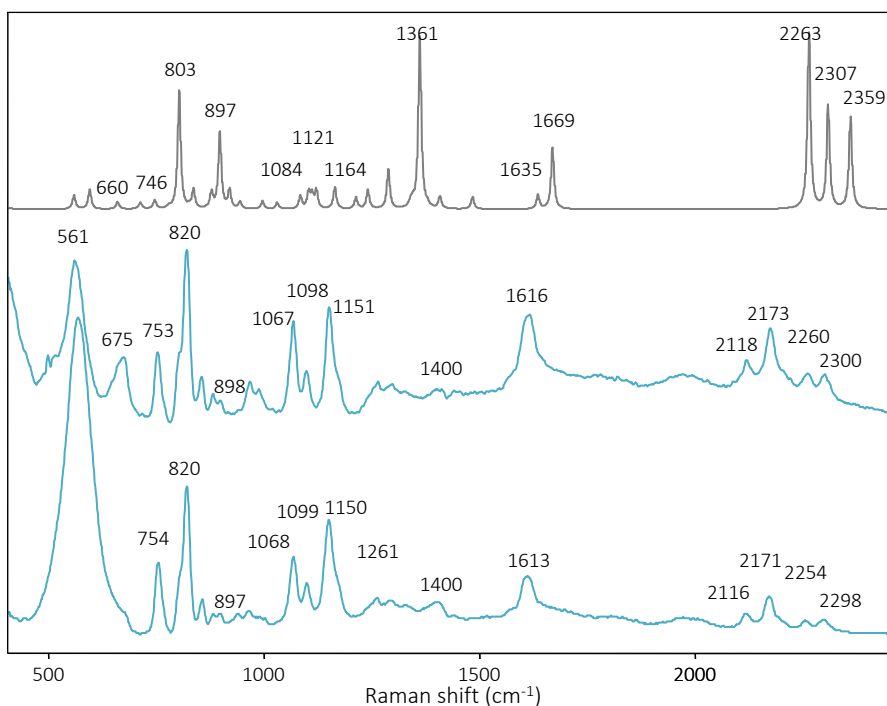


Figure 3.9. SERS spectra of d-Hyp

a) Calculated SERS spectrum of Hyp with one Au⁺ ion added. b) and c), experimental SERS spectra of Hyp in gold colloids, at a concentration of 5×10^{-4} M, different repetitions of the experiment (LL=785nm).

Table 3.4. Assignment for the spectra of d-Hyp in solid and solution

Calculated frequency (cm ⁻¹)	Observed frequency in solution (cm ⁻¹)	Assignment
278		OH bending
282		Ring bending
307		Ring bending and OH bending
353		CD ₂ rocking
412		CH ₂ rocking
560	561	Ring torsion and O-Au stretching
596		Ring bending
661	675	Ring torsion
714		NH ₂ rocking
747	753	Ring and carboxylate torsion
779		Ring torsion
804	820	Ring stretching
826		Ring stretching
837	855	Ring stretching
879	882	Ring stretching
898	898	Ring stretching
920		C-C stretching
945		C-N-C stretching
997	967	C-C stretching
1031	988	C-C stretching
1084	1067	C-C stretching
1103		CD ₂ scissoring
1111	1098	CH ₂ and NH ₂ rocking, and CD bending
1122		Ring bending
1164	1151	Ring torsion
1213	1263	CH and OH bending
1241	1295	CH ₂ twisting
1288		NH ₂ twisting
1339		C-C stretching
1345		CH ₂ wagging

1361	~1400	COO ⁻ symmetric stretching and NH ₂ twisting
1380		NH ₂ wagging
1408		CH and OH bending
1483		CH ₂ scissoring
1635		NH ₂ scissoring
1669	1613	COO ⁻ antisymmetric stretching and NH ₂ scissoring
2263	2118	CD ₂ symmetric stretching
2308	2173	CD stretching
2359	2260	CD ₂ antisymmetric stretching
3073		CH stretching
3084		CH stretching
3146		CH ₂ antisymmetric stretching
3321		NH stretching
3503		NH stretching
3798		OH stretching

3.4. Conclusions

In conclusion, an experimental procedure is presented to demonstrate the acquisition of reproducible SERS spectra of hydroxyproline. The study of molecules, such as the amino acids, with inherent low Raman cross section and photosensitive on silver surfaces, may require special protocols to attain reproducible analytical results using SERS.

3.5. References

1. Guerrero, A. R.; Aroca, R. F. *J. Raman Spectrosc.* **2012**, *43*, 478.
2. Aliaga, A. E.; Osorio-Román, I.; Garrido, C.; Leyton, P.; Cárcamo, J.; Clavijo, E.; Gomez-Jeria, J. S.; Díaz, G.; Campos-Vallette, M. M. *Vib. Spectrosc.* **2009**, *50*, 131.
3. Aliaga, A. E.; Osorio-Román, I.; Leyton, P.; Garrido, C.; Cárcamo, J.; Caniulef, C.; Celis, F.; Díaz, G.; Clavijo, E.; Gómez-Jeria, J. S.; Campos-Vallette, M. M. *J. Raman Spectrosc.* **2009**, *40*, 164.
4. Tarakeshwar, P.; Manogaran, S. *Theochem-J. Mol. Struct.* **1997**, *417*, 255.
5. István, K.; Keresztury, G.; Szep, A. *Spectrochim. Acta A* **2003**, *59A*, 1709.
6. Cárcamo, J. J.; Aliaga, A. E.; Clavijo, E.; Garrido, C.; Gómez-Jeria, J. S.; Campos-Vallette, M. M. *J. Raman Spectrosc.* **2012**, *43*, 750.
7. Lee, P. C.; Meisel, D. *J. Phys. Chem.* **1982**, *86*, 3391.
8. Frisch, M. J.; Trucks, G. W.; Schlegel, H. B.; Scuseria, G. E.; Robb, M. A.; Cheeseman, J. R.; Scalmani, G.; Barone, V.; Mennucci, B.; G. A. Petersson, H. N., M. Caricato, X. Li, H. P. Hratchian, A. F. Izmaylov, J. Bloino, G. Zheng, J. L. Sonnenberg, M. Hada, M. Ehara, K. Toyota, R. Fukuda, J. Hasegawa, M. Ishida, T. Nakajima, Y. Honda, O. Kitao, H. Nakai, T. Vreven, J. A. Montgomery, Jr., J. E. Peralta, F. Ogliaro, M. Bearpark, J. J. Heyd, E. Brothers, K. N. Kudin, V. N. Staroverov, R. Kobayashi, J. Normand, K. Raghavachari, A. Rendell, J. C. Burant, S. S. Iyengar, J. Tomasi, M. Cossi, N. Rega, J. M. Millam, M. Klene, J. E. Knox, J. B. Cross, V. Bakken, C. Adamo, J. Jaramillo, R. Gomperts, R. E. Stratmann, O. Yazyev, A. J. Austin, R. Cammi, C. Pomelli, J. W. Ochterski, R. L. Martin, K. Morokuma, V. G. Zakrzewski, G. A. Voth, P. Salvador, J. J. Dannenberg, S. Dapprich, A. D. Daniels,

- Ö. Farkas, J. B. Foresman, J. V. Ortiz, J. Cioslowski, and D. J. Fox; Gaussian, Inc.: Wallingford, CT, 2009.
9. Dawson, R. M. C.; Elliott, D. C.; Elliott, W. H.; Jones, K. M. *Data for Biochemical Research*; Clarendon Press: Oxford, 1959.
 10. Kapitán, J.; Baumruk, V.; Kopecký, V.; Pohl, R.; Bouř, P. *J. Am. Chem. Soc.* **2006**, *128*, 13451.
 11. Covington, A. K.; Tait, M. J.; Wynne-Jones, L. *Discuss. Faraday Soc.* **1965**, *39*, 172.
 12. Kreevoy, M. M.; Mead, C. A. *J. Am. Chem. Soc.* **1962**, *84*, 4596.

Chapter Four

Surface-Enhanced Fluorescence with Shell-Isolated Nanoparticles: SHINEF

This work has been published in the journal *Angewandte Chemie*, in both International^[1] and German^[2] editions, in January 2011, under the same title. This material has been adapted from that paper with permission* from John Wiley & Sons (see *Permissions Obtained for Published Copyrighted Materials* section, page 154.).

This work has meant recognition for the author and his advisor from the University (see section Vita Auctoris, in the last pages of this thesis) in February 2012.

4.1. Introduction

In a 2010 report by then-graduate student Jian-Feng Li from Dr. Zhongqun Tian's group^[3] in Xiamen, China, a new approach for SERS was described, which was termed *shell-isolated nanoparticle-enhanced Raman spectroscopy* (SHINERS). The plasmon-enhanced Raman signal is provided by gold nanoparticles with an ultrathin silica shell (2 to 4 nm). The enhancing coated Au nanoparticles can be spread as 'smart dust' over the surface, and the coating separates them from direct contact with the probed material. The authors also pointed out that the SERS signal disappeared when changing the shell thickness from 2 to 20 nm. In SHINERS, working with an ultrathin shell for the Au@SiO₂ nanoparticles is essential to expose the adsorbate to the maximum electromagnetic field from the Au core (enhancement factor of 85 at 4 nm for particles with a diameter of 55 nm).

However, for a fluorophore located on an enhancing nanostructure, increasing the spacer layer (shell thickness) will make obvious a continuous transition from fluorescence

* ©2011 John Wiley & Sons Inc.

quenching to fluorescence enhancement. Therefore, *shell-isolated nanoparticles* (SHINs) with *thicker* coatings could be ideal substrates for SEF.^[4-6]

Here we demonstrate the application of the SHINs for SEF (*shell-isolated nanoparticle enhanced fluorescence*, SHINEF) using a single Langmuir-Blodgett (LB) monolayer containing fluorescent probes. The enhanced fluorescence cross section is one of the highest in molecular spectroscopy with values in the order of 10^{-17} cm²/molecule and, correspondingly, there is a rainbow of applications for this very strong spectroscopic signal.^[6-8] A maximum fluorescence enhancement is achieved at a certain distance from the nanostructure surface, and this property has been demonstrated using silver island films and SiO_x as spacer layers by Wokaun *et al.*^[9], and also using the LB technique to separate the metal from the probe molecule.^[10]

Recently, the continuous transition from quenching to SEF for a single molecule on gold has been reported.^[11] In this study it is shown that for molecule-gold distances shorter than 5 nm the fluorescence is quenched. Since it is possible to control the shell thickness of the shell-isolated nanoparticles^[12], it is evident that they are ideal SEF enhancing nanostructures with a broad range of potential applications: “expanding versatility”^[13] of SEF with portable nanostructures. The dipole emission can be strongly modified by the coupling of an excited molecule and the surface states of a metal. This interaction has been discussed in an early paper by Philpott in 1975,^[14] exploring the idea of using fluorescence to probe the surface-plasmon polaritons in metals.

Presently, plasmonics^[15,16] provides the reference for plasmon-enhanced spectroscopies, and central to SERS and SEF are the surface-plasmon polaritons observed in nanostructures, or localized surface plasmon resonances (LSPR)^[17]. Gersten and Nitzan^[5] provided the first complete electromagnetic study for a molecule-particle system in terms of a modified local electromagnetic field. The plasmon resonance connection was first pointed out by Moskovits in 1978.^[18]

4.2. Materials and Methods

Solutions were prepared mixing (1:10) octadecyl rhodamine B (R18) with *n*-eicosanoic acid (C₂₀H₄₀O₂) or arachidic acid (AA), and (1:10 and 1:100) bis(*n*-butylimido)perylene (nBPTCD) with arachidic acid. The concentration of the dye was 10⁻⁴ M and that of the arachidic acid was 10⁻³ M, and the solvent was dichloromethane. To improve solubility of nBPTCD, three drops of trifluoroacetic acid were added and then the solution was sonicated for 5 minutes. The solutions were covered in aluminum foil to protect them from light.

4.2.1. SHIN Particle Synthesis

SHIN particles were synthesized adapting the method described by Li *et al.*^[3] The gold core was synthesized by gold citrate reduction of tetrachloroauric acid (HAuCl₄) based upon existing protocols.^[19,20] 50 mL of 0.01% HAuCl₄ solution was brought to boiling. A solution of 1% sodium citrate (667 μL) was added. Boiling was continued for 10 minutes and then removed from heat, while the stirring was continued for 15 minutes.

Later, to produce the silica coating, to the resulting solution we added 3 mL of a 1 mM aqueous solution of 3-aminopropyl-trimethoxysilane (APTMS) under vigorous stirring, and then allowed to stand. The resulting solution was heated in a water bath to a temperature between 90-95°C; when reaching this range, we added 9 mL of activated 0.54% aqueous sodium silicate solution to get the silica coating, then allowed the solution to stand at this temperature for 2 hours and let cool down. The samples were filtered using 0.20 μm pore polyethersulfone filters (Sarstedt), and later centrifuged at 4000 rpm for 30 minutes, recovering the sediment.

4.2.2. Electron Microscopy

SEM images were taken with the FEI Quanta 200 described in section 2.2.2. TEM images were obtained with the high resolution TEM instrument FEI Titan 80-300 described in section 2.2.1.

4.2.3. LB Filmmaking

Langmuir monolayers of R18 and nBPTCD mixtures were prepared at the air-water interface of the Nima film balance described in section 2.4, in order to obtain the surface pressure-area isotherms and perform the depositions over glass slides. The solutions were spread on the aqueous surface using a Hamilton microsyringe held very close to the aqueous surface and then the solvent was allowed to evaporate completely over a period of time at least 25 minutes. The subphase was ultrapure Milli-Q water at a constant temperature of 23°C. The monolayer was then compressed at a fixed barrier speed of 10 cm²/min to record the surface pressure-area (π -A) isotherm. The Langmuir-Blodgett monolayers on Corning glass slides were fabricated by Z-deposition at a constant surface pressure of 25 mN/m. To perform the SHINEF experiments, a drop of 5 μ L of the SHIN particles was deposited over the LB monolayer (on the glass slide) and allowed to dry under warm air.

4.2.4. Spectroscopic measurements

UV-visible absorption spectra were recorded for the solutions employing the Varian Cary 50 spectrophotometer described in Chapter 2.

Fluorescence and Raman spectra were acquired by point-by-point mapping of a section of the LB surface with the 50 \times objective (1 μ m² spatial resolution), with the Renishaw inVia micro-Raman system using the 514.5 nm laser line, described in section 2.5.

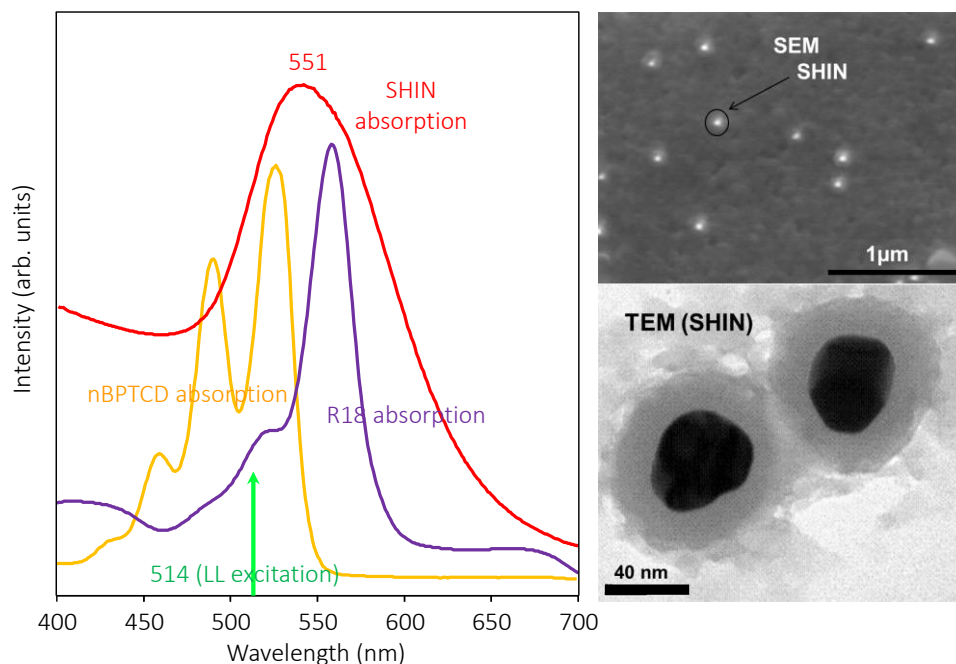


Figure 4.1. Absorption spectra of the SHINs' plasmon, R18 and nBPTCD dyes, and SEM and TEM images of the SHINs.

4.3. Results and Discussion

The plasmon absorption of the shell-isolated nanoparticles and the electronic absorption spectra of two dyes (R18 and nBPTCD) in solution are shown in Figure 4.1. Notably, the absorption of the nanoparticles and the dyes is in resonance with the 514.5 nm laser line, and this line has been used to demonstrate the “smart dust” SEF. The scanning electron microscopy (SEM) and the transmission electron microscopy (TEM) images of the SHIN nanoparticles in the smart dust are also shown in Figure 4.1, where the brightness is due to the gold core. The plasmon absorption of the shell-isolated nanoparticles (SHIN), selected in our work for the proof of concept, is relatively narrow (FWHM[†] of 88 nm) with a gold core of ca. 50 nm and the thickness of the coating is ca. 20 nm, a coating that prevent the observation of SERS^[3]. The R18 reference fluorescence

[†] The full width at half maximum (FWHM) is defined as the the width of a band (can be either transmittance, absorbance or scattering) measured at half of the maximum transmittance (absorbance or scattering) value. It is the most common way in spectroscopy to express how broad a band is.

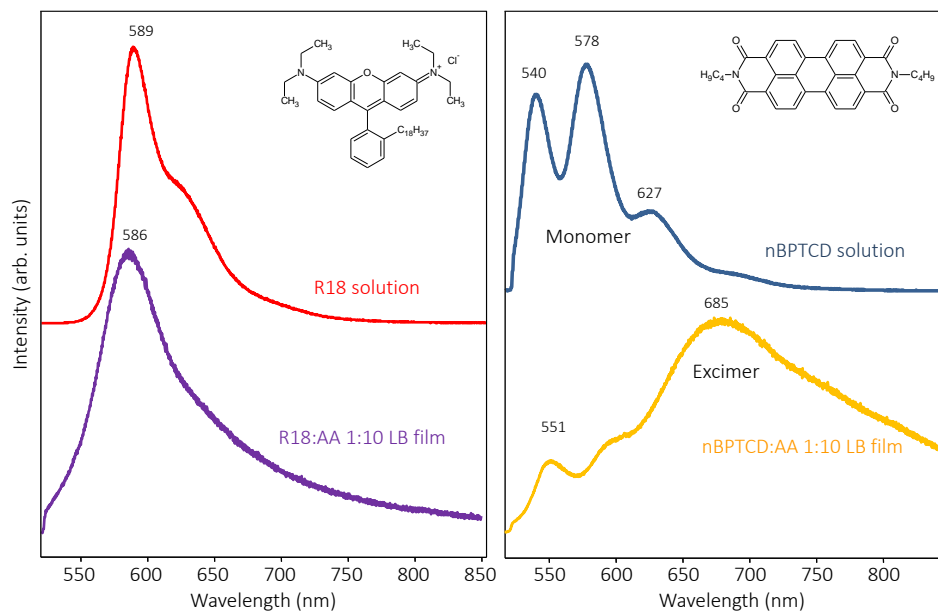


Figure 4.2. Reference fluorescence spectra of R18 and nBPTCD in solution and of one LB monolayer on glass.

of a 10^{-4} M solution and that of a mixed LB monolayer R18-arachidic acid (1:10 ratio) is shown in Figure 4.2. The solution emission of R18 shows a maximum at 589 nm and a shoulder at 618 nm. The LB fluorescence of R18 is quite similar showing a maximum at 586 nm. The arachidic acid is used here to facilitate the transfer of the monolayer to solid substrates^[21]. The surface enhanced fluorescence induced by the SHIN nanoparticles is shown in Figure 4.3. The SEF in that figure corresponds to an “average SEF enhancement” (similar to the definition used for average SERS)^[22] over the probe surface. It simply means that there is a distribution of enhancement factors (EF) contributing to the observed enhanced signal, and some localized spots may have a fairly large enhancement factor compared to observed average.

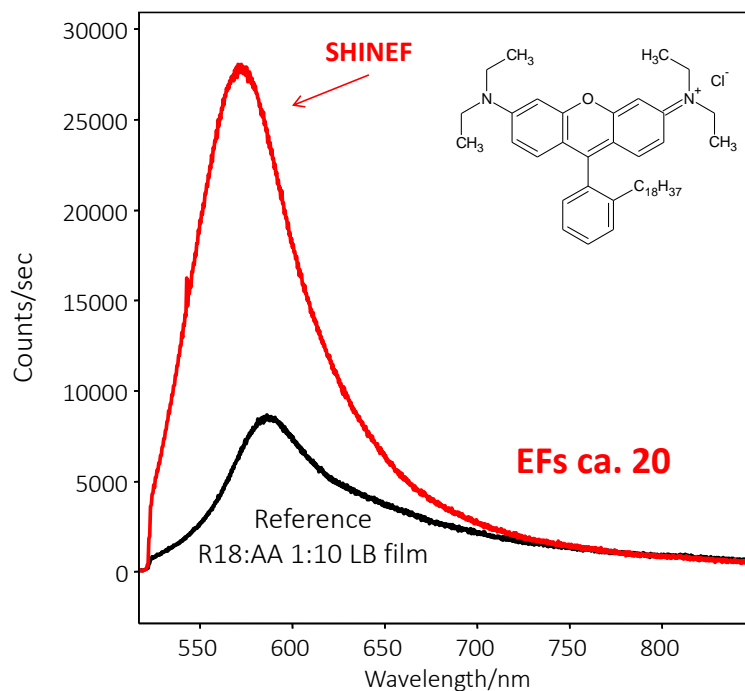


Figure 4.3. Surface enhanced fluorescence of the R18 LB monolayer with “smart dust” nanoparticles

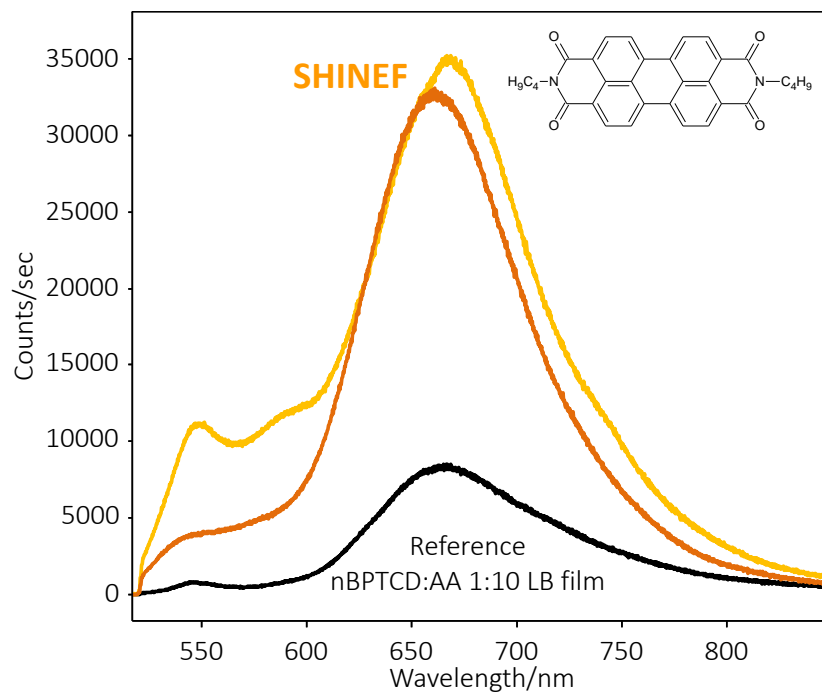


Figure 4.4. Reference fluorescence and SHINEF of a mixed LB monolayer (1:10) of nBPTCD and arachidic acid.

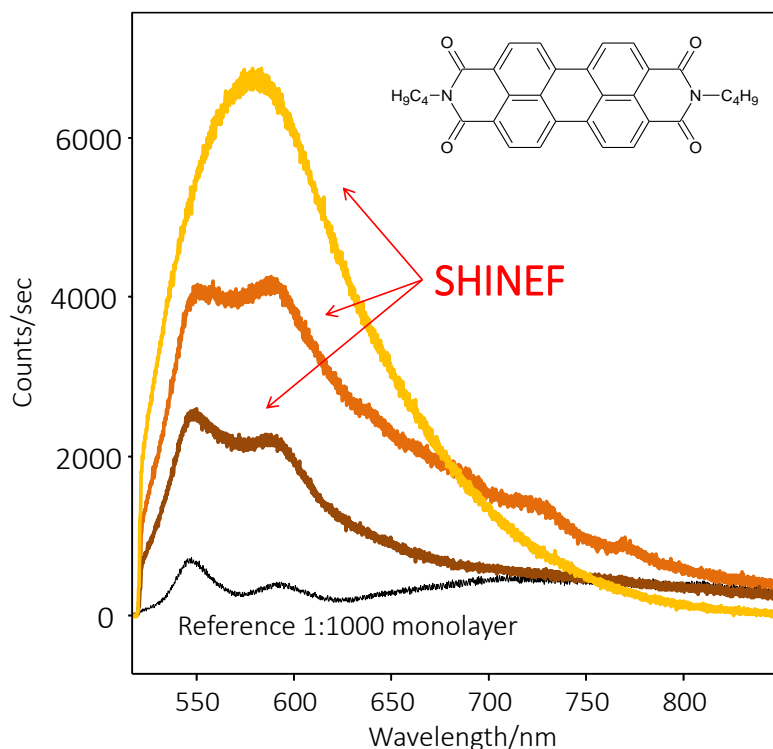


Figure 4.5. Reference fluorescence and SHINEF of a mixed LB monolayer (1:1000) of nBPTCD and arachidic acid. The spectra in yellow and brown are three points in the mapping where SHINEF is observed.

The reference fluorescence spectra of nBPTCD in dilute solutions is the mirror image of the absorption spectrum shown in Figure 4.1 with maxima at 540, 578 and 623 nm. From several previous studies,^[22,23] it is known that the PTCd dyes, in addition to the monomer emission (nBPTCD in solution in Figure 4.2), they produce a very strong red-shifted excimer emission in the solid state, and particularly in “concentrated” LB films due to the formation of aggregates. In the 1:10 (nBPTCD:AA) mixed film, the broad (structureless) excimer emission prevails in the fluorescent spectrum as can be seen in Figure 4.2b (bottom trace). The SHINEF at two points of the monolayer covered with SHINs is given in Figure 4.4. A mapping of the small surface area shows enhancement factors in the 1-20 range for the integrated intensity of the excimer emission. The presence of the monomer is occasionally seen in the multifile of the mixed film.

Experiments were also carried out with a dilute mixed monolayer (1:1000 nBPTCD:AA) and the results are illustrated in Figure 4.5. The reference spectrum of the dilute mixed

monolayer shows the typical bands of the monomer at 547 nm and 589 nm, and correspondingly the SHINEF shows similar structure. However, the enhancement produces an overlap of the main peaks as can be seen in Figure 4.5. It should be pointed out that when LB monolayers of PTCd derivatives are transferred directly onto silver or gold nanostructures and excited with the 514.5 nm laser line, the fluorescence is almost completely quenched and surface-enhanced resonance Raman scattering (SERRS) is observed.^[23,24] In the present work with the thick coating of the SHIN used, we do not observe SERRS. At the time of publishing of the paper associated with this article, synthesis of SHINs with variable core (size and shape) and coating thicknesses were in progress for plasmonic manipulation, focusing on thickness coatings between around 10 nm or below for SHINEF applications^[25,26] and they are detailed in the following chapters of this thesis. Although SHINEF was shown for specific SHINs of a thick coating ca. 20 nm, SHINEF can also be attained with thinner coatings. Coatings of about 10 nm produce SHINEF as shown in Figure 4.7. For practical applications a coating of ca. 6 nm or more is recommended to maximize SEF and avoid any SERS signal. For instance, when a section of the LB monolayer is covered with the stock “naked” nanoparticles, fluorescence is partially quenched and SERRS is observed (Figure 4.6). However, the section of the LB surface covered with SHINs gives only SHINEF.

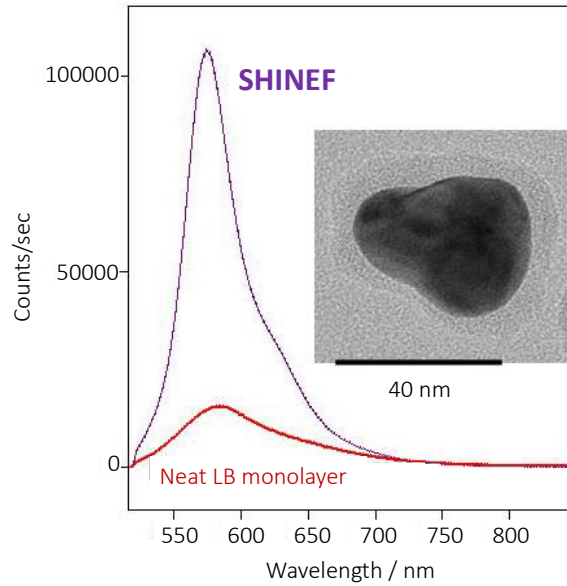


Figure 4.7. SEF of the R18 LB monolayer with SHIN nanoparticles with thinner shell. This is compared to the reference fluorescence of the mixed LB monolayer of R18 on quartz. HRTEM of SHIN nanoparticle with SiO₂ coating of ca. 10 nm (Inset)

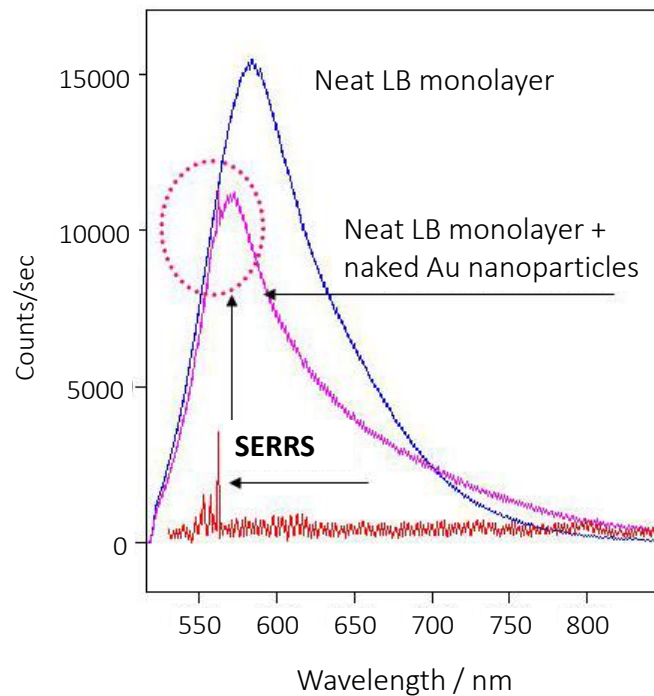


Figure 4.6. Fluorescence of the neat LB monolayer on quartz and subsequent addition of naked gold nanoparticles. The SERRS spectrum has been plotted separately, after subtracting the fluorescence background.

As an addition to the data published in the 2011 *Angewandte Chemie* paper, we can say something about the batch of SHINs employed to obtain most of the results of the paper. We have recently discovered that they are still in *very good* condition, proving that the particles are stable even 3 years after their synthesis. We show this data in Figures 4.8 to 4.10.

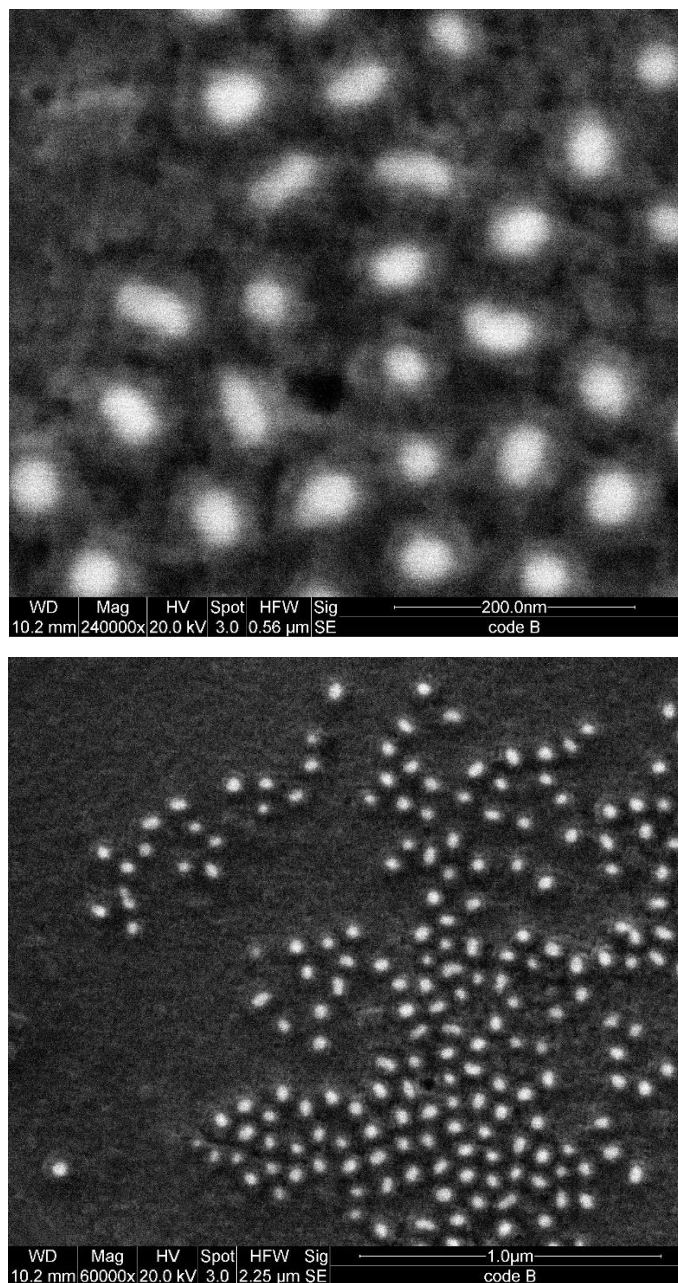


Figure 4.8. SEM images of the SHIN particles used for most of the results of the *Angewandte Chemie* paper (codenamed “code B”). Images taken 3 years after they were synthesized and used for the results of the paper.

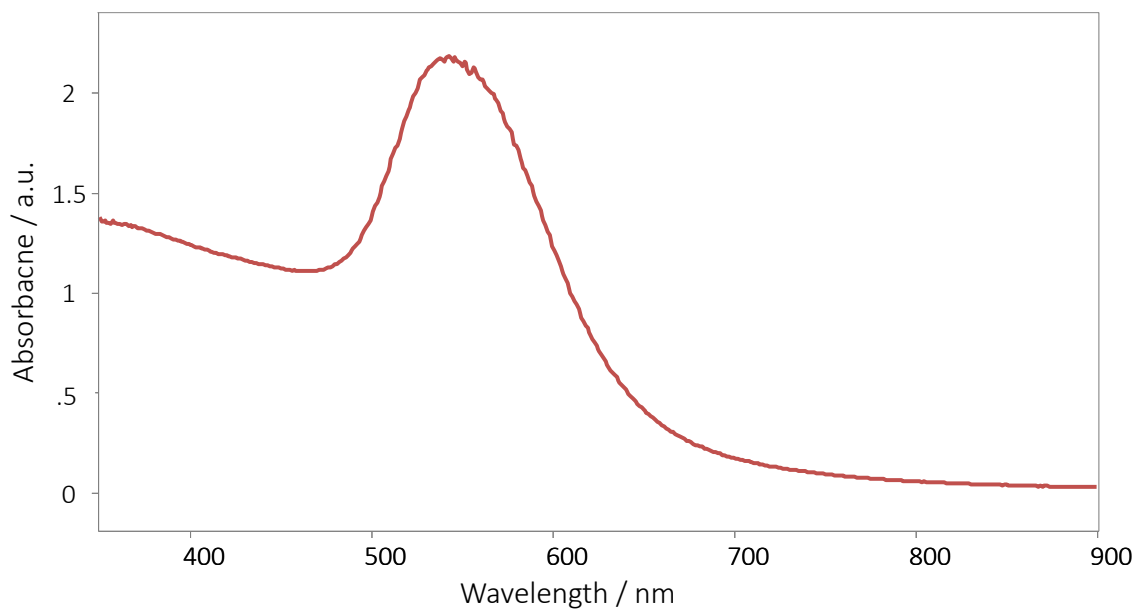


Figure 4.9. Absorption spectrum of the SHIN particles in 2013.

The absorption spectrum has barely changed at all between 2010 and 2013; after a simple Gaussian fit in GRAMS, the maximum is still at 551 nm, exactly where it was back in 2010 (see Figure 4.1)

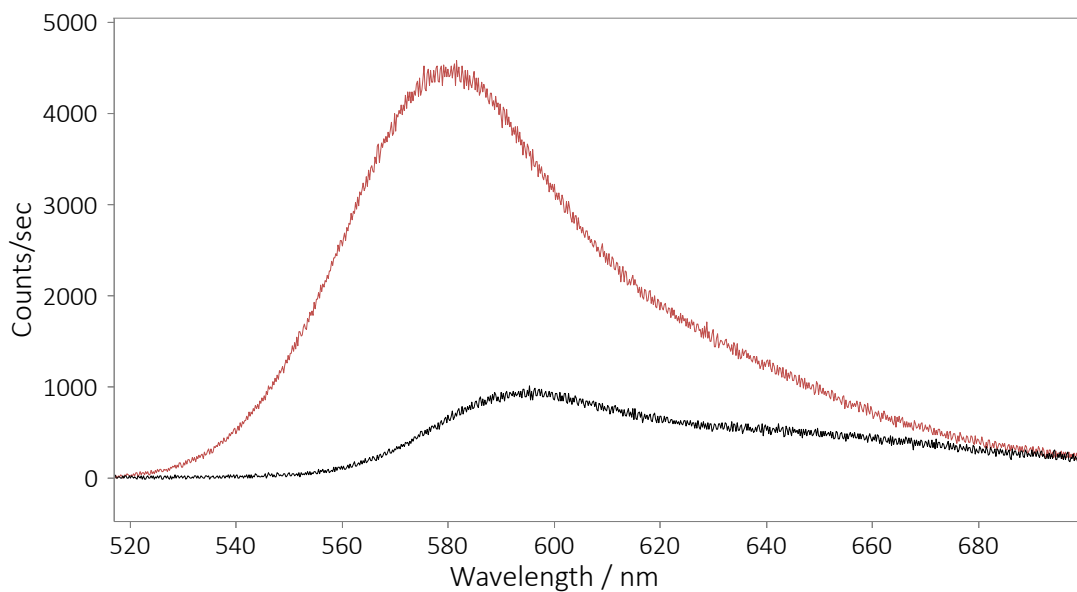


Figure 4.10. Quick (up to 700 nm only) test spectra with a R18:AA 1:10 LB film with the aged particles. The Au SHINs are still well capable of giving SHINEF. The red trace is the SHINEF and the black trace is the fluorescence of the reference LB film. Spectra acquired on April 2013 (originals are from June 2010)

4.4. Conclusions

In conclusion, average surface-enhanced fluorescence is demonstrated with silica coated gold nanoparticles (SHINEF) acting as smart dust on the surface of single Langmuir-Blodgett (LB) monolayer, and this project serves as the proof-of-concept for it. Coating gold and silver nanoparticles of different sizes and shapes (different plasmon absorptions) opens a wide scope of applications for SEF, where the shape of the core and the thickness of the coating can be tuned for specific tasks. The technique of spreading the enhancing nanostructure provides a new approach to experimental SEF.

4.5. References

1. Guerrero, A. R.; Aroca, R. F. *Angew. Chem. Int. Ed.* **2011**, *50*, 665.
2. Guerrero, A. R.; Aroca, R. F. *Angew. Chem. Ger. Edit.* **2011**, *123*, 691.
3. Li, J. F.; Huang, Y. F.; Ding, Y.; Yang, Z. L.; Li, S. B.; Zhou, X. S.; Fan, F. R.; Zhang, W.; Zhou, Z. Y.; Wu, D. Y.; Ren, B.; Wang, Z. L.; Tian, Z. Q. *Nature* **2010**, *464*, 392.
4. Fort, E.; Gresillon, S. *J. Phys. D: Appl. Phys.* **2008**, *41*, 013001/1.
5. Gersten, J.; Nitzan, A. *J. Chem. Phys.* **1981**, *75*, 1139.
6. Lakowicz, J. R. *Anal. Biochem.* **2001**, *298*, 1.
7. Fort, E.; Gresillon, S. *J. Phys. D: Appl. Phys.* **2008**, *41*, 013001/1.
8. Lakowicz, J. R.; Geddes, C. D.; Gryczynski, I.; Malicka, J.; Gryczynski, Z.; Aslan, K.; Lukomska, J.; Matveeva, E.; Zhang, J.; Badugu, R.; Huang, J. *J. Fluoresc.* **2004**, *14*, 425.
9. Wokaun, A.; Lutz, H. P.; King, A. P.; Wild, U. P.; Ernst, R. R. *J. Chem. Phys.* **1983**, *79*, 509.
10. Aroca, R.; Kovacs, G. J.; Jennings, C. A.; Loutfy, R. O.; Vincett, P. S. *Langmuir* **1988**, *4*, 518.
11. Anger, P.; Bharadwaj, P.; Novotny, L. *Phys. Rev. Lett.* **2006**, *96*, 113002.
12. Liz-Marzán, L. M.; Giersig, M.; Mulvaney, P. *Langmuir* **1996**, *12*, 4329.
13. Moskovits, M. *Nature* **2010**, *464*, 357.
14. Philpott, M. R. *J. Chem. Phys.* **1975**, *62*, 1812.
15. Brongersma, M. L.; Zia, R.; Schuller, J. A. *Appl. Phys. A-Mater.* **2007**, *89*, 221.

16. Meier, S. A. *Plasmonics: Fundamentals and Applications*; 1st ed.; Springer Science: New York, NY, 2007.
17. Willets, K. A.; Van Duyne, R. P. *Annu. Rev. Phys. Chem.* **2007**, *58*, 267.
18. Moskovits, M. J. *Chem. Phys.* **1978**, *69*, 4159.
19. Frens, G. *Nature, Phys. Sci.* **1973**, *241*, 20.
20. Grabar, K. C.; Freeman, R. G.; Hommer, M. B.; Natan, M. J. *Anal. Chem.* **1995**, *67*, 735.
21. Goulet, P. J. G.; Aroca, R. F. *Anal. Chem.* **2007**, *79*, 2728.
22. Aroca, R. *Surface-enhanced Vibrational Spectroscopy*; John Wiley & Sons: Chichester, 2006.
23. Volpati, D.; Job, A. E.; Aroca, R. F.; Constantino, C. J. L. *J. Phys. Chem. B* **2008**, *112*, 3894.
24. Goulet, P. J. G.; Aroca, R. F. *Anal. Chem.* **2007**, *79*, 2728.
25. Aroca, R. F.; Teo, G. Y.; Mohan, H.; Guerrero, A. R.; Albella, P.; Moreno, F. J. *Phys. Chem. C* **2011**, *115*, 20419.
26. Guerrero, A. R.; Zhang, Y.; Aroca, R. F. *Small* **2012**, *8*, 2964.

Chapter Five

Plasmon-Enhanced Fluorescence and Spectral Modification in SHINEF

This work has been published in the *Journal of Physical Chemistry C* in April 2011 under the same title.^[1] The materials presented here have been adapted with permission* (see *Permissions Obtained for Published Copyrighted Materials* section, page 154.).

5.1. Introduction

The introduction of shell-isolated gold nanoparticles to obtain enhanced fluorescence, called SHINEF,^[2,3] invites the question of fine tuning the properties of the coated nanoparticles for maximum enhancement, such as the core size and shape as well as shell thickness. In addition, the versatility provided by the easy use of the SHINs, offers a unique opportunity to investigate the question of spectral profile modification and extract further understanding of the nature of plasmon enhanced fluorescence. Here, we present experimental results with SHINs of different sizes and shell thickness, and the interpretation of results is helped by computational modeling using finite-difference time-domain and DDA methods. In addition, the question of spectral profile modification^[4,5] is examined using well defined two dimensional structures or Langmuir-Blodgett monolayers of two emitters (monomer and excimer) of the same fluorophore.

* Adapted with permission from: Plasmon-Enhanced Fluorescence and Spectral Modification in SHINEF. Aroca, R. F.; Teo, G. Y.; Mohan, H.; Guerrero, A. R.; Albella, P.; Moreno, F. *J. Phys. Chem. C* **2011**, *115*, 20419. Copyright © 2011 American Chemical Society

For this chapter, Geok Yi Teo and Haider Mohan performed synthesis of the spherical nanoparticles; Pablo Albella and Fernando Moreno provided the supporting theoretical calculations. The author performed synthesis and spectroscopy work with silica-coated gold nanorods showing spectral profile modification.

The emission of the fluorophore is strongly affected by its interactions with the electromagnetic environment. The fluorophore can completely lose its ability to emit by transferring its excitation energy to a metal surface^[6] (fluorescence quenching). However, some metals nanostructures sustaining localized surface plasmon resonances(LSPR)^[7,8] can enhance the emission under the right conditions of excitation, geometry and metal-molecule spacing, producing surface enhanced fluorescence (SEF). Once the LSPR is excited, the key parameter is the metal-molecule separation. In SHINEF, a plasmon enhancing nanostructure with a built in spacer is used for practical applications. In surface-enhanced Raman scattering (SERS),^[8-10] the highest enhancement comes from molecules either directly attached to the metal nanostructure or very close to it^[11] and consequently, the spectral properties (wavenumber and relative intensities) of the species adsorbed onto the metal nanoparticles may change on account of the chemical or physical interactions with the nanostructure, and, correspondingly, the far field scattering of electromagnetically enhanced SERS spectrum will contain the information that shed light on these molecule-nanostructure interactions. The spectral modification in SERS due to the properties of the far field scattering itself is difficult to separate in the observed SERS spectra, although it has been identified by several groups.^[12,13] For physisorbed molecules and submonolayer surface coverage the plasmon effects can be clearly captured in the far field scattering.^[14] In SHINEF (or SEF in general) the molecule is about 10 nm away from the metal surface, and the spectral modification is almost entirely due to the plasmonic modification of the observed enhanced spectrum.

5.2. Materials and Methods

All glassware used was cleaned with aqua regia (1:3 ratio of HNO₃: HCl) and rinsed thoroughly with ultrapure (Milli-Q, 18.2 MΩ·cm) water. The solvent used in all solutions preparation is ultrapure Milli-Q water unless stated otherwise. Tetrachloroauric acid (HAuCl₄·3H₂O), cetyltrimethyl-ammonium bromide (CTAB), sodium borohydride (NaBH₄), ascorbic acid, tetraethylorthosilicate (TEOS) and arachidic acid (AA) were purchased from Sigma-Aldrich and used without further purification.

SHIN particle synthesis. SHINs were prepared according to the method described by Grabar *et al.*^[15] and Li *et al.*^[11] with slight modifications. First, the gold core is prepared by the sodium citrate reduction method of tetrachloroauric acid. In a round-bottom flask equipped with a condenser, 250 mL of 5×10^{-4} M HAuCl₄, is brought to boil with vigorous magnetic stirring. An addition of 12.5 mL of 38.8 mM sodium citrate is made rapidly and the resulting solution is reddish-purple in colour. The solution is then boiled for another 10 minutes, removed from heat and stirring was continued for another 15 minutes. The solution was then cooled to room temperature and then characterized by its absorption maximum.

To coat the gold cores with silica, 3 mL of a freshly prepared 1 mM APTMS solution was added to 50 mL of the gold-citrate colloid under vigorous stirring for 10 minutes. The mixture of APTMS and gold colloid was then heated in a water bath to a temperature of between 90-95°C. Once it reached this temperature range, 6 mL of activated 0.54% aqueous sodium silicate solution (pH 10-11) was added to begin silica coating on the gold particles. Samples of 1mL each were collected every 15 minutes up until 3 hours. The samples were made concentrate by centrifugation at 12,000 rpm for 7 minutes and removing most of the supernatant. The unused portion of the gold-citrate colloid was kept and stored in the dark in case of future use. A second batch of 150 mL of 5×10^{-4} M HAuCl₄ gold cores was also prepared by the same method but only 3.4 mL of 38.8 mM of sodium citrate was added as a smaller volume was used. To silica coat the gold cores, the same procedure was followed but only 25 mL of the gold-citrate colloid was coated and samples were taken every 15 minutes up until 2 hours only. The TEM images of small and large coated gold nanoparticles are shown in Figure 5.1a. The gold nanoparticles used in spectral profile modification experiments were made from a third batch following the same method described above. A 50 mL solution of 0.01% HAuCl₄ was reacted with 800 μ L 1% sodium citrate; the resulting gold nanoparticles had plasmon absorption with maximum at 531 nm, the silica shell was ca. 11 nm.

Synthesis of nanorods. Nanorods are synthesized adapting the method proposed originally by Nikobaakht and El-Sayed.^[16] A seed solution is prepared by adding, under

constant stirring at 28°C, 50 µL of a 0.05 M HAuCl₄ solution into a flask containing 10 mL of a 0.100 M CTAB solution. To this solution we add 600 µL of a freshly-prepared ice-cold solution of NaBH₄ 10 mM. Upon addition of NaBH₄, the solution turns yellow-brownish. This solution was left undisturbed for a minute before use. A growth solution is prepared, in parallel to the seeds, by adding consecutively and under constant stirring at 28°C, 10 mL of a 0.100 M CTAB solution, 100 µL of a 0.004 M AgNO₃ solution, 100 µL of a 0.05 M HAuCl₄ solution, and 100 µL of 0.1 M ascorbic acid solution. The growth solution turns from yellow to colourless upon addition of ascorbic acid. After this was completed, 24 µL of the seeds solution were added to the growth solution, always stirring at 28°C. The solution started fading very slowly to blue, and the reaction is completed after about 30 minutes.

The silica-coating of this solution was done following Gautier et al.^[17] The resulting nanorods solution was alkalinized by adding tiny droplets of a 1 M NaOH solution until the pH reaches 10.5. At this point, three additions of TEOS 20%v/v in methanol were made with intervals of 30 minutes, adding 50 µL of TEOS every time. After the third addition, the solution was left to stand for 12 hours. After this, the solution was filtered through a Whatman No. 1 paper to remove the excess of CTAB, and concentrated by centrifugation at 12000 rpm, collecting the sediment. 3 µL of this concentrated solution was cast over the glass slide containing the mixed chloro-PTCD-arachidic acid LB film.

SEM images were taken with a FEI Quanta 200 Environmental scanning electron microscope equipped with an Everhart-Thornley secondary electron detector and a solid state backscatter detector. TEM images were obtained with a high resolution TEM instrument FEI Titan 80-300. UV-visible absorption spectra were recorded employing a Cary 50 scan UV-visible spectrophotometer. All fluorescence experiments were conducted using our micro-Raman Renishaw inVia system, with laser excitation at 514.5 and ca. 20 µW at the sample. All measurements were made in a backscattering geometry, using a 20× microscope objective probing an area of ca. 5 µm². 2D mapping results were collected through the rastering of a computer controlled 3-axis encoded (XYZ) motorized stage, with a step of 5 µm.

Langmuir monolayers of Octadecylrhodamine B dye (R18) and bis(3,4-dichlorobenzylimido)perylene (Cl-PTCD) mixtures with arachidic acid (*n*-eicosanoic acid) were prepared at the air-water interface of our Nima film balance (model 302M) described in section 2.4. Langmuir films were made in the air-water interface by spreading a solution in dichloromethane containing one part of the dye and 10 of arachidic acid on the surface of ultra-pure Milli-Q water subphase. The Langmuir film was left for ca. 30 minutes to ensure a complete evaporation of the solvent. The film was then compressed by a couple of moving barriers at a speed of 10 cm²/min. The Langmuir film is deposited onto a clean Corning glass slide under constant pressure to form the Langmuir-Blodgett (LB) film for SHINEF experiments.

Numerical solution of the far field (scattering cross section) and near field for SHINs are obtained by solving Maxwell's equations for a plane wave incident on the exact geometry of the SHIN (single, dimer and trimer). The simulations have been performed with use of finite-difference time-domain software (Lumerical) using optical data from Johnson and Christy^[18]. This numerical method is broadly established in computational electromagnetism to calculate the optical response of different nanostructures. It consists of a direct implementation of the Maxwell time-dependent curl equations to solve the temporal variations of electromagnetic waves within a finite space that contains a metal nanoparticle.^[12] In practice, the space including the scatterer is discretized into a grid that contains the basic element and the results depend both on the number of the cells used in the simulation and the simulation time. The results are fully convergent, and they may be considered an accurate solution of Maxwell's equations. Additionally, the results shown here have been tested with another solving method, the discrete dipole approximation^[19] (DDA), producing very good agreement.

5.3. Results and Discussion

For a molecule placed near field of a laser-irradiated gold nanostructure, the observed emission is a function of the metal-molecule distance^[20]. This distance dependence is the most important property of SEF, and by varying the distance between molecule and

nanostructure a continuous transition from fluorescence quenching to fluorescence enhancement has been experimentally demonstrated.^[20-23] In practice, SEF is clearly observed when the metal-molecule separation is about 5 nm or more.^[21] The power of the observed fluorescence for a neat molecular compound is directly proportional to absorption rate (κ_0), the number of the absorbing species (n_0) and the quantum yield (Φ_f):

$$P \propto \kappa_0 n_0 \Phi_f \quad (5.1)$$

For simplicity, let's make a distinction between two contributions to the observed SEF intensity. First, the absorption rate of a molecule located in the near field of nanostructure supporting can be modified, and simultaneously it can be an increase or decrease in the quantum yield, since both the radiative and non-radiative decays can be modified. There is abundant supporting experimental evidence that measured lifetimes decrease for molecules at or near metal nanostructures, changing Φ_f .^[23] The second contribution to the measured SEF is the re-radiated emission by the excited nanostructure. Notably the first contribution (near field) may enhance the absorption and the quantum yield; but since the molecule is at a distance from the metal, one does not expect dramatic changes in the spectral profile of the emission. However, the re-radiated emission carries the signature of the far field scattering of the nanostructure used to obtain SEF, i.e., the fluorescence enhancement factor (EF) has a strong frequency dependence can be simplified as the product of the two contributions:^[24]

$$EF_{\text{fluorescence}}(\omega)_s = G_{\text{rad}}^*(\omega_s) G_{\text{loc}}(\omega_L) \quad (5.2)$$

The subindex s is used to indicate the frequency dependence of the enhancement to the red of the excitation. The $G_{\text{loc}}(\omega_L)$ is the local field enhancement factor that modifies both the molecular absorption and the quantum yield. The modified radiative rate, $G_{\text{rad}}^*(\omega_s)$, adapted from Etchegoin *et. al.*^[4] and properly normalized, carries the strong frequency dependence due to LSPRs in the nanostructure.

5.3.1. Spherical Particles: Effect of the Core and Shell Sizes

SHINEF is a versatile experimental approach that permits to test the optical properties of simple model described above. First, we discuss the tuning of SHIN nanoparticles for maximum enhancement.

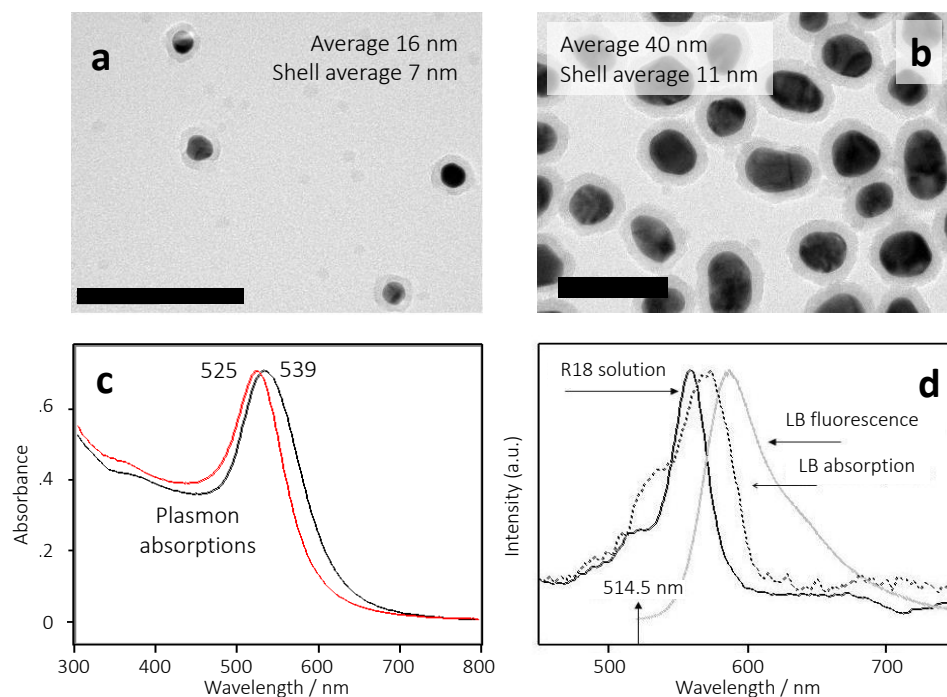


Figure 5.1. Characterization of the sphere-like Au SHINs to study the effect of the core size. a) TEM of small SHINs with absorption at 525 nm and b) SHINs with plasmon absorption at 539 nm. c) Absorption of small and large SHINs, and d) Absorption of the R18 in solution, and fluorescence of R18 in solution and of the LB film. Scalebars represent 100 nm.

SHINEF was recorded for two distinct gold core size and variable SiO₂ shell thickness spread onto a fluorophore R18 forming a mixed LB monolayer. The transmission electron microscopy of the SHIN particles is shown in Figure 5.1a for small core particles, with an average diameter of 16 nm. Figure 5.1b shows the large SHINs with an average diameter of 40 nm. A scanning electron microscopy image of the large SHINs is shown in Figure 5.2. The corresponding surface plasmon absorptions can be seen in Figure 5.1c. The molecular electronic absorption of R18 in solution, the absorption of the LB monolayer and the reference fluorescence spectrum of the monolayer is shown in Figure 5.1d. The uncoated colloids spread over the LB monolayer containing the R18 dye quench the fluorescence as expected. All coated gold nanoparticles or SHINs produce SHINEF.

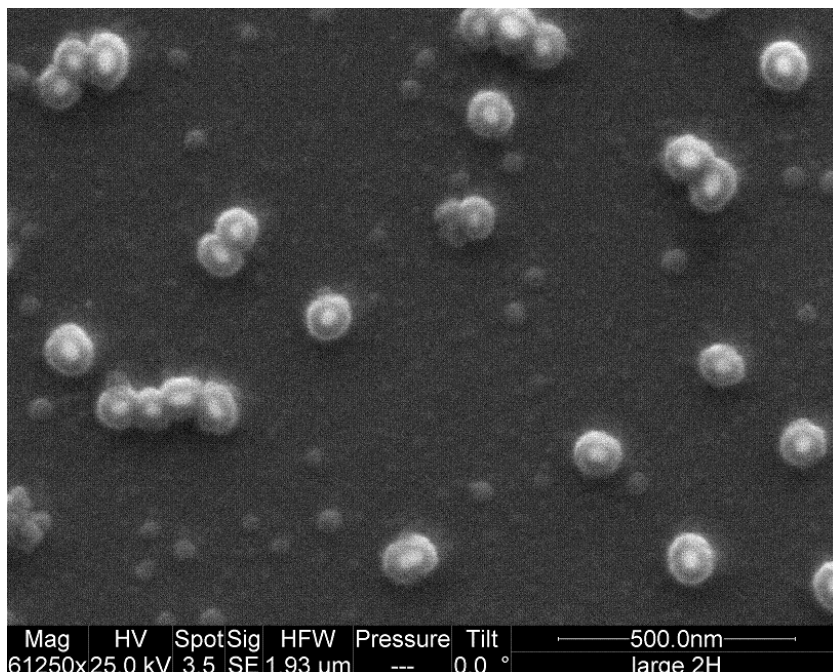


Figure 5.2. SEM image of the large SHINs.

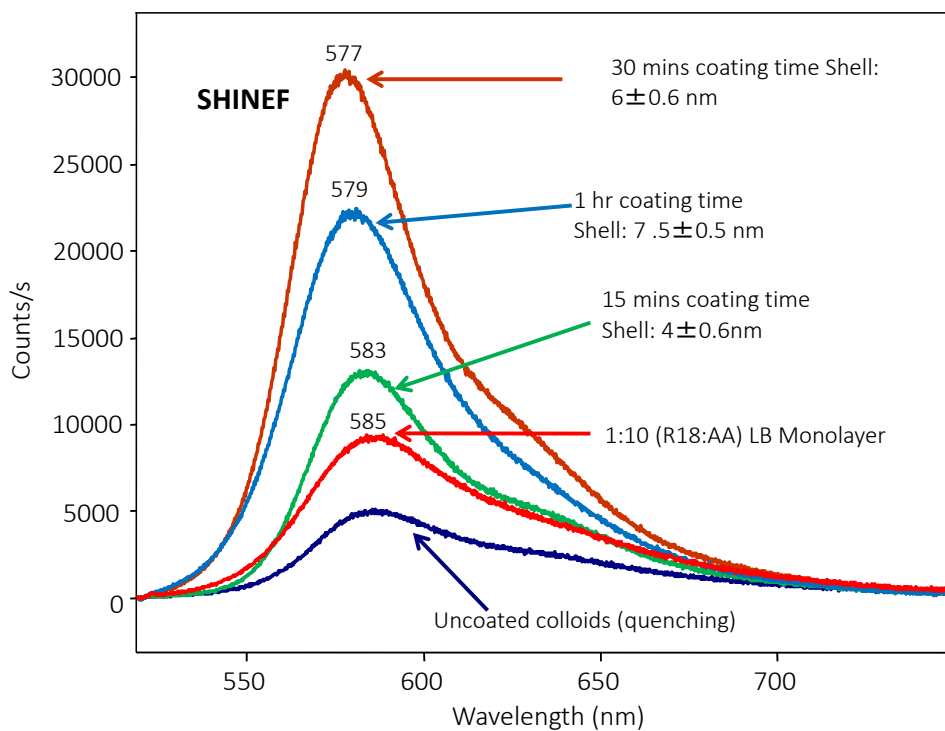


Figure 5.3. SHINEF from small core gold SHINs with different shell thickness. The LB reference fluorescence and the quenching effect of uncoated colloids are also included.

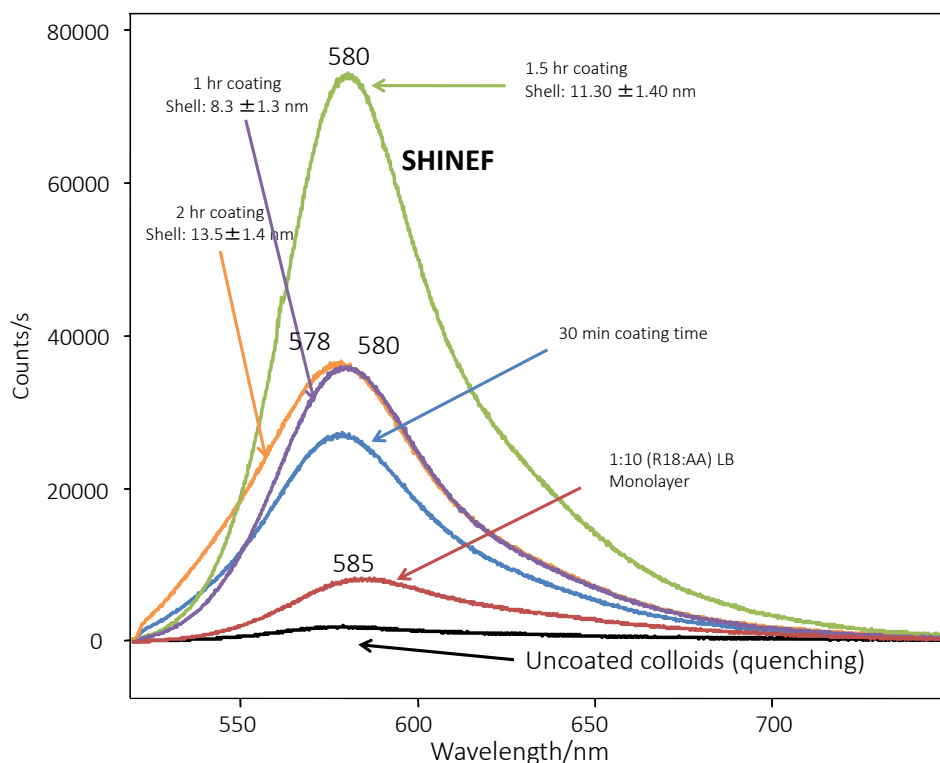


Figure 5.4. SHINEF from large core gold SHINs with different shell thickness. The LB reference fluorescence and the quenching effect of uncoated colloids are also included.

The SHINEF results for the small core SHINs with different coatings are shown in Figure 5.3. The best enhancement factor ($EF \sim 4$) was found for SHINs with a SiO_2 coating of ca. 6 to 7 nm. The spectral profile of the enhanced fluorescence spectrum of the R18 in the LB monolayer (Figure 5.3) is practically the same compared to the reference LB spectrum (with a very small “blue” shift in the band maximum).

Similarly, the SHINEF of large diameter SHINs is recorded by spreading the SHINs over the mixed R18 LB monolayer and the results can be seen in Figure 5.4. Again, the uncoated colloids produce quenching, while all coated gold nanoparticles give SHINEF. However, the best absolute average enhancement ($EF \sim 10$) is obtained for SHINs with an average core of ca. 40 nm and a coating thickness of 11 nm of SiO_2 . Once more, the spectral profile of R18

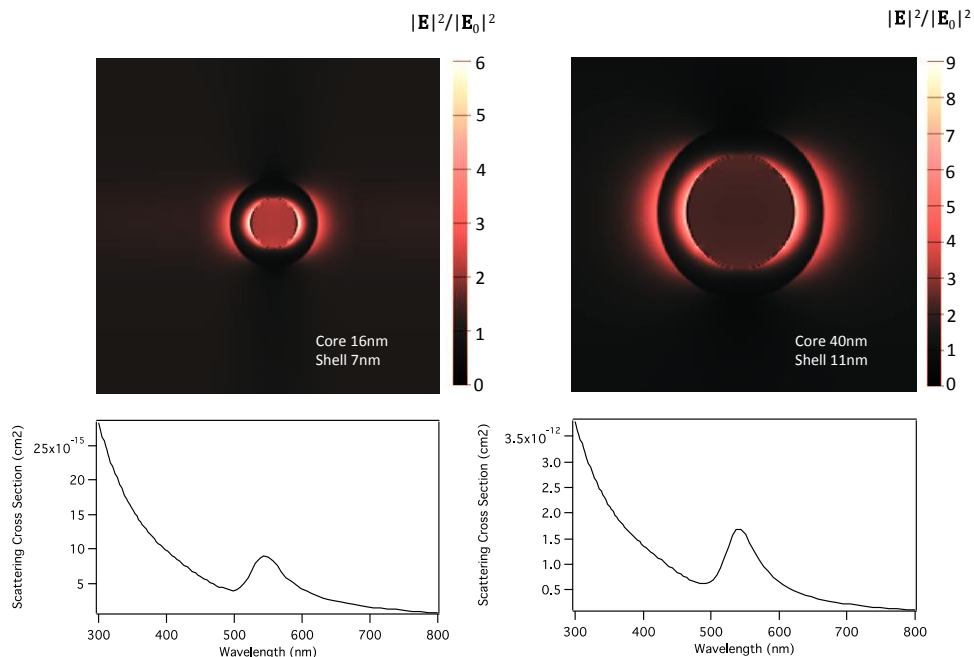


Figure 5.5. Calculated near field enhancement of small and large SHINs at 515 nm excitation and far field scattering of the small and large SHIN particles.

SHINEF is the same as that of the reference LB fluorescence. Notably, the absolute enhancement factor of the large coated SHINs was consistently higher than that of the corresponding small SHINs.

The experimental results are supported by the computational results indicating that the large core particles have a higher local field enhancement compare to the small SHINs as illustrated in Figure 5.5. The top of the figure shows near field relative intensity ($|E|^2 = |E_{loc}/E_0|^2$) patterns corresponding to small nanoshells (left) and larger nanoshells (right) respectively. Both patterns have been calculated by means of the FDTD method. Two areas of enhancement can be seen. One inside the particle, close to the metallic surface, which is “refracted” producing the other area of enhancement outside the particle. This external enhancement is what is seen by the fluorescent molecules. According to the numerical results, the ratio between these external enhancements for large and small SHINs is of the order of 2.

In addition, we also show in Figure 5.5 plots of the far field scattering cross sections corresponding to the same SHINs which again demonstrate that larger SHINs scatter light more efficiently than smaller ones. Notably, the far field scattering contribution from SHIN-

dimers and also SHIN-trimers it is even more intense than that of SHIN monomers; however, all scatterings have the same spectral profile.

In summary, both the near field contribution and the re-radiated emission are generously proportioned for the large SHINs and they are more efficient enhancers of fluorescence. In both cases, the almost negligible spectral profile modification of R18 is seen as a minor blue shift (5 nm) of the centre of the fluorescence band. It is important to point out that the optimum shell thickness is found *not to be the same* for small (ca. 6 nm) and large SHINs (ca. 11 nm).

5.3.2. Nanorods and Spectral Profile Modification

The fluorophore used to study the spectral profile modification is Cl-PTCD, shown in Figure 5.6. The fluorescence spectra of the solution and that of the mixed LB monolayer are also given in the figure. The fluorophore sample presents two very distinct emitters: the monomer emission and the excimer emission that is prominent in aggregated samples

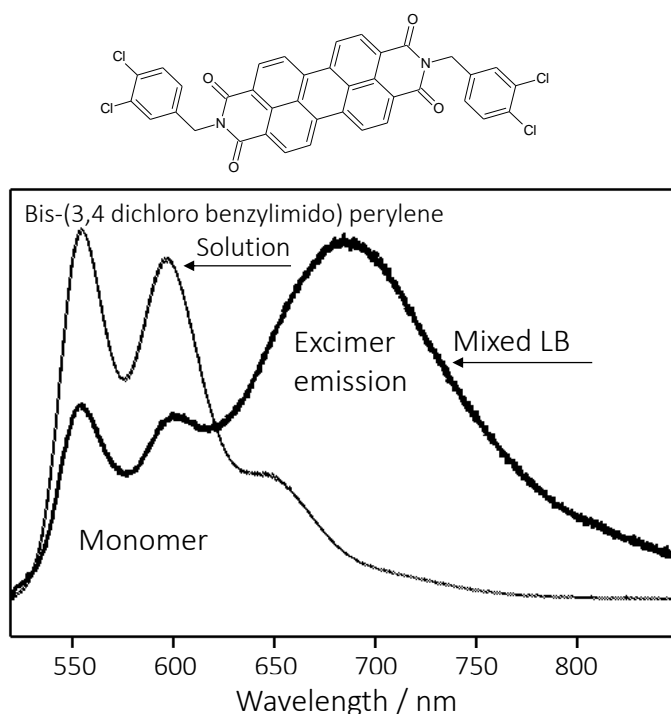


Figure 5.6. Fluorescence spectrum of the Cl-PTCD solution (monomer) and fluorescence from the Cl-PTCD mixed LB showing the monomer and excimer components of the emission.

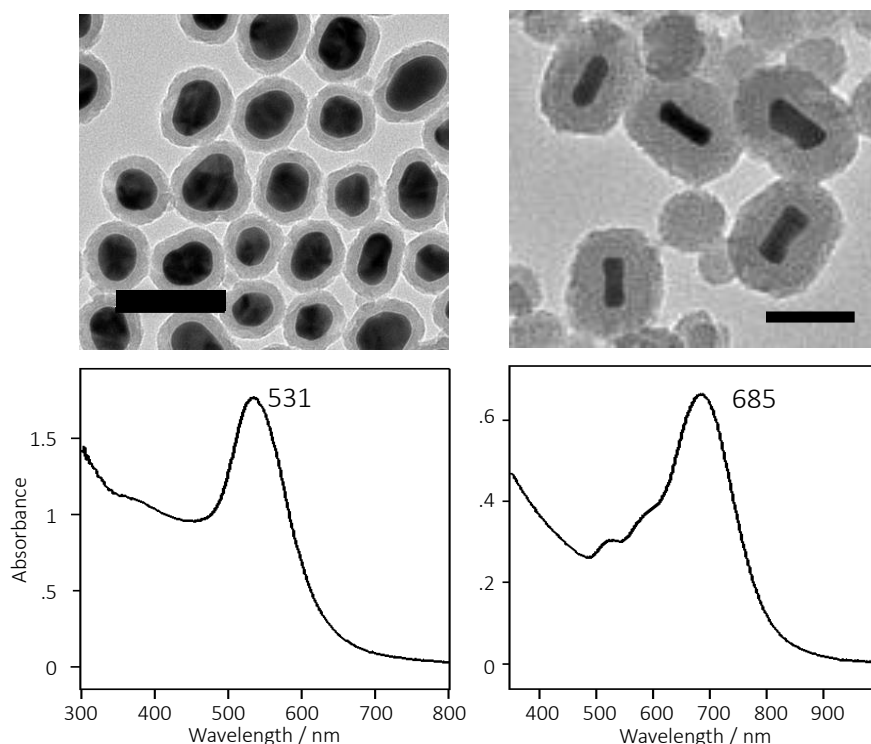


Figure 5.7. TEM of SHINs particles with absorption at 531 nm and SHIN nanorods with plasmon absorption at 685 nm. Scale bars represent 100 nm.

such as the LB monolayer. It is important to notice here that the spectral profile of the fluorescence of the mixed LB monolayer Cl-PTCD/arachidic acid is the result of the superposition of two spectra: the fluorescence of the monomer (dominant in dilute solutions), and that of the excimer dominant in aggregated samples. This spectral profile can be changed by varying the mole ratio in the mixed film. In the series of 3,4,9,10-perylenetetracarboxylic diimide (PTCD) derivatives planar π -stacking^[25] is an important model that helps to understand the excimer formation. For this particular PTCD derivative with a bulky substituent on the PTCD chromophore, the 1:10 ratio of Cl-PTCD:AA provided a spectral profile where the emission of both monomer and excimer are clearly seen (Figure 5.6), a condition for a good reference point to study the effect of the far field scattering of SHIN nanoparticles against that of SHIN nanorods. In other words, to observe the effect of the re-radiated emission from the nanostructure, we employed SHINs with a far field scattering profile closely matching the fluorescence shape (spectral profile) of each one of the emitters.

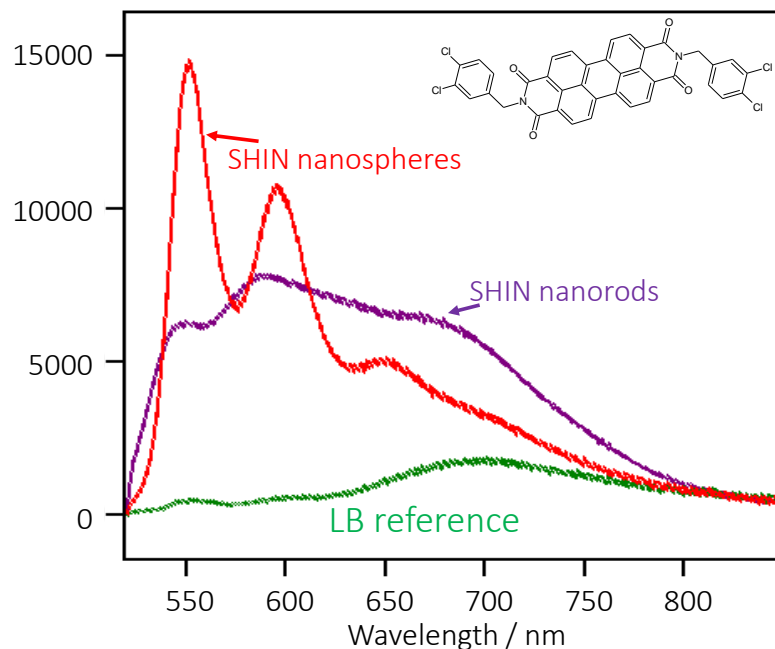


Figure 5.8. Spectral profile modification in SHINEF with shelled nanospheres and nanorods. The former enhance preferentially the monomer and the latter the excimer, the emissions from a mixed Cl-PTCD/AA (1:10 molar ratio).

The TEM of the SHINs are shown in Figure 5.7. The round SHINs correspond to the large core gold nanoparticles discussed above and their scattering is in the 500-600 nm region of the spectrum. The SHIN nanorods absorb around 685 nm and their scattering would be around the 700 nm spectral region. The SHINEF results illustrating the spectral profile modification are presented in Figure 5.8. We selected for the figure one representative SHINEF spectrum from the point-by-point mapping of the SHINEF spectra obtained by spreading the SHIN particles onto the LB monolayer. The complete series of the spectra from each map are shown in Figures 5.9 and 5.10. It is seen that when round SHINs are used the spectrum of the monomer in the monolayer is preferentially enhanced, since the monomer emission is in close match with the far-field scattering of the nanoparticles. On the other hand, when the nanorods are used for SHINEF, the excimer component in the fluorescence spectrum becomes prominent, changing the profile of the observed spectrum. It should be pointed out that each SHINEF spectrum is an average fluorescence spectrum collected using a microscope objective that collects the emitted light from a surface area of ca. $5 \mu\text{m}^2$. Therefore, these spectra represent the emission collected from

a “large” surface area of the monolayer, avoiding the problem of points with hefty aggregation or extreme dilution.

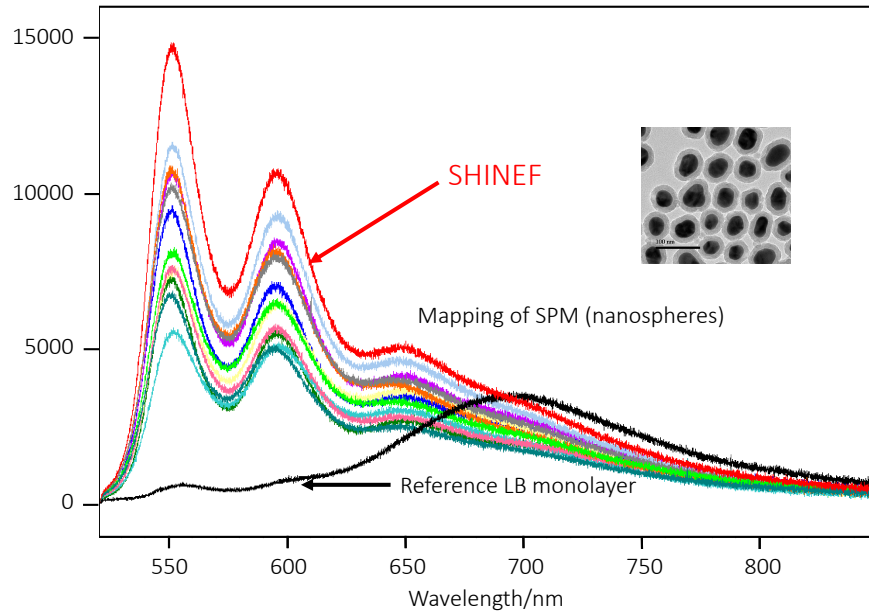


Figure 5.9 All spectra in the map with spherical AuSHINs on a Cl-PTCD:AA 1:10 LB film. It is hardly possible to see the emission of the excimer

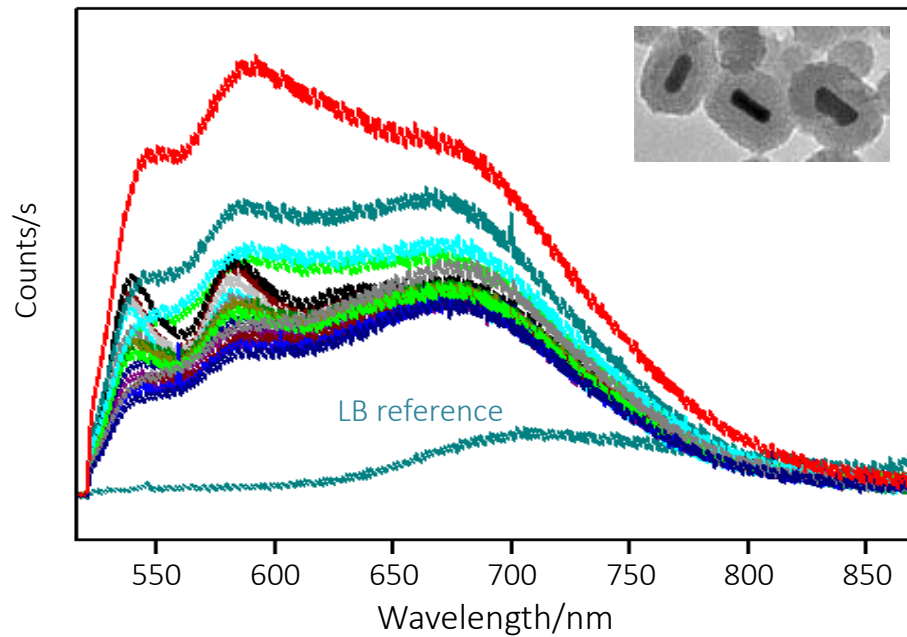


Figure 5.10. All spectra in the mapping with AuSHIN nanorods on a Cl-PTCD:AA 1:10 LB film. The emission of the excimer is clearly seen due to the spectral profile modification induced by the nanorods.

5.4. Conclusions

The versatility of SHINEF is demonstrated for two different SHIN sizes. Small gold particles of about 16 nm diameters can be used for SHINEF with shell thickness between 6 to 7 nm, although thinner coating down to 4 nm and thicker coating will also render the effect. The SHINEF efficiency increases with increasing core size. Core gold sizes of ca. 40 nm and shell thickness around 11 nm gave higher enhancement. These SHIN particles seem to have ideal dimensions for practical applications. The plasmonic effect leading to spectral profile modification is demonstrated with SHINs of different shapes. In other words, observed enhanced fluorescence will show a spectral profile modification modulated by the unique far field scattering of nanostructure. In this respect the use of SHINs of different shapes, such as rods, can help produce SHINEF in specific spectral regions, or target specific analytes in the visible or near infrared spectrum.

5.5. References

1. Aroca, R. F.; Teo, G. Y.; Mohan, H.; Guerrero, A. R.; Albella, P.; Moreno, F. J. *Phys. Chem. C* **2011**, *115*, 20419.
2. Guerrero, A. R.; Aroca, R. F. *Angew. Chem. Ger. Edit.* **2011**, *123*, 691.
3. Guerrero, A. R.; Aroca, R. F. *Angew. Chem. Int. Ed.* **2011**, *50*, 665.
4. Le Ru, E. C.; Etchegoin, P. G.; Grand, J.; Félidj, N.; Aubard, J.; Lévi, G. *J. Phys. Chem. C* **2007**, *111*, 16076.
5. Tam, F.; Goodrich, G. P.; Johnson, B. R.; Halas, N. J. *Nano Lett.* **2007**, *7*, 496.
6. Chance, R. R.; Prock, A.; Silbey, R. In *Advances in Chemical Physics*; John Wiley & Sons, Inc.: 1978, p 1.
7. Willets, K. A.; Van Duyne, R. P. *Annu. Rev. Phys. Chem.* **2007**, *58*, 267.
8. Moskovits, M. *Rev. Mod. Phys.* **1985**, *57*, 783.
9. Le Ru, E. C.; Etchegoin, P. G. *Principles of Surface Enhanced Raman Spectroscopy (and related plasmonic effects)*; Elsevier: Amsterdam, 2009.
10. Aroca, R. *Surface-enhanced Vibrational Spectroscopy*; John Wiley & Sons: Chichester, 2006.

11. Li, J. F.; Huang, Y. F.; Ding, Y.; Yang, Z. L.; Li, S. B.; Zhou, X. S.; Fan, F. R.; Zhang, W.; Zhou, Z. Y.; Wu, D. Y.; Ren, B.; Wang, Z. L.; Tian, Z. Q. *Nature* **2010**, *464*, 392.
12. Zhao, J.; Pinchuk, A. O.; McMahon, J. M.; Li, S. Z.; Ausman, L. K.; Atkinson, A. L.; Schatz, G. C. *Acc. Chem. Res.* **2008**, *41*, 1710.
13. Le Ru, E. C.; Galloway, C.; Etchegoin, P. G. *Phys. Chem. Chem. Phys.* **2006**, *8*, 3083.
14. Rubim, J. C.; Aroca, R. F. *Phys. Chem. Chem. Phys.* **2008**, *10*, 5412.
15. Grabar, K. C.; Freeman, R. G.; Hommer, M. B.; Natan, M. J. *Anal. Chem.* **1995**, *67*, 735.
16. Nikoobakht, B.; El-Sayed, M. A. *Chem. Mater.* **2003**, *15*, 1957.
17. Gautier, C.; Cunningham, A.; Si-Ahmed, L.; Robert, G.; Burgi, T. *Gold Bull.* **2010**, *43*, 94.
18. Johnson, P. B.; Christy, R. W. *Phys. Rev. B* **1972**, *6*, 4370.
19. Yurkin, M. A.; Hoekstra, A. G. *J. Quant. Spectrosc. Radiat. Transfer* **2011**, *112*, 2234.
20. Wokaun, A.; Lutz, H. P.; King, A. P.; Wild, U. P.; Ernst, R. R. *J. Chem. Phys.* **1983**, *79*, 509.
21. Anger, P.; Bharadwaj, P.; Novotny, L. *Phys. Rev. Lett.* **2006**, *96*, 113002.
22. Aroca, R.; Kovacs, G. J.; Jennings, C. A.; Loutfy, R. O.; Vincett, P. S. *Langmuir* **1988**, *4*, 518.
23. Ray, K.; Badugu, R.; Lakowicz, J. R. *Langmuir* **2006**, *22*, 8374.
24. Le Ru, E. C.; Etchegoin, P. G.; Grand, J.; Felidj, N.; Aubard, J.; Levi, G. *J. Phys. Chem. C* **2007**, *111*, 16076.
25. Gerstenberg, M. C.; Schreiber, F.; Leung, T. Y. B.; Bracco, G.; Forrest, S. R.; Scoles, G. *Phys. Rev. B* **2000**, *61*, 7678.

Chapter Six

Plasmon Enhanced Raman-Fluorescence Ratio with Shell-Isolated Silver Nanoparticles

This work has been published in the journal *Small*, in October 2012 under the title “Experimental Confirmation of Local Field Enhancement Determining Far Field Measurements with Shell-Isolated Silver Nanoparticles”^[1] This material has been adapted from that paper with permission* from John Wiley & Sons (see *Permissions Obtained for Published Copyrighted Materials* section, page 154.).

6.1. Introduction

The plasmonic enhancement of fluorescence or scattering involves the same enhancement mechanism^[2,3] which is governed by the local field enhancements in nanostructures sustaining localized surface plasmon resonances (LSPR).^[2,4] It is the localized field enhancement that is responsible for surface-enhanced spectroscopic processes such as SHINERS^[5] and SHINEF.^[6,7]

As was first pointed out by Gersten and Nitzan,^[8,9] and later also by Kerker *et al.*,^[2] the Raman benefits from the enhancement of both incident and scattered fields, and the enhancement factor for nanospheres is approximately: $EF \approx \frac{E_{loc}^2 E_{loc}'^2}{E_0^4} = 16|g|^2 |g'|^2$, where E_0 is the incident field and E_{loc} the enhanced local field, that leads to a Raman enhancement proportional to the fourth power of the factor $|E_{loc}/E_0|$, i.e., gives the

* © 2012 John Wiley and Sons.

Yun Zhang contributed to this project by performing most of the synthesis work of the Ag SHINs that were employed in this paper.

$|E|^4 = |E_{loc}/E_0|^4$ approximation, extensively discussed and used even for nanostructures other than spheres.^[10] However, surface enhanced fluorescence (SEF) can only benefit from the enhanced local field and should be proportional to $|E|^2 = |E_{loc}/E_0|^2$, with EFs (commonly between 1 and 100) much more modest than those commonly observed in SERS.^[10,11] Experimentally, a direct comparison between these EFs has not been possible for molecules directly adsorbed onto metallic nanostructures due to the “first layer” effects: a) the chemical interaction of the molecule with the metal nanoparticle may change the nature of the adsorbate (formation of surface complex) giving a different vibrational Raman signature; b) in the case of SEF, fluorescence quenching becomes overriding for such small distances and the particle surface is well approximated by a plane boundary.^[12-14]

However, with the advent of new shell-isolated nanostructures (SHINs), one could compare the local field enhancement at a fixed distance (greater than 5 nm)^[10] from the metal surface with measurements carried out in the far field.^[15] Therefore, eliminating the “first layer effects” that may dramatically change the corresponding spectra, it would be possible to extract the local field factor $|E|$ common to these two enhancements measured in the far field. The use of shell-isolated nanoparticles (SHIN) guarantees a separation between the target molecule and the metal surface. In this report, we first extend our previous work on gold-SHINs introducing the fabrication of shell isolated *silver* nanoparticles (Ag-SHINs). The next step is to find a molecule that would simultaneously render SHINERS and SHINEF in the same spectrum. To explore the evaluation of the $|E|$ factor, we choose the crystal violet (CV) molecule, which has a low quantum yield, allowing the Raman and the fluorescence to be observed in the same spectrum by selecting the appropriate laser line (see Figure 6.1). Therefore, with Ag-SHINs, the plasmon enhanced vibrational Raman is observed “unperturbed” from the reference spectrum in solution and the SHINEF is collected for molecules located outside the zone of strong quenching or dramatic changes in the lifetime. In addition, by working in solution we are measuring reproducible average properties. The experimental results confirm that the plasmon-enhanced fluorescence is proportional to the square of the local field enhancement while

the plasmon-enhanced Raman scattering is given by the fourth power of the local field enhancement.

6.2. Materials and Methods

AgNO₃ and tetraethylorthosilicate (TEOS, 98%) were purchased from Sigma-Aldrich and used without further purification. Crystal violet (CV) was purchased from Fisher Scientific and Octadecyl Rhodamine B (R18) was obtained from Invitrogen. Unless otherwise specified, solutions are aqueous and the water employed is Milli-Q quality (18.2 MΩ·cm). All glassware was cleaned using *aqua regia* and rinsed with abundant Milli-Q water. The core silver colloids were prepared according to the method of Leopold and Lendl^[16] by reduction of silver nitrate with hydroxylamine at alkaline pH. Briefly, hydroxylamine solution 1.5×10⁻³ M (45ml) was added to the beaker and droplets of a 1 M NaOH solution to adjust the hydroxylamine solution to pH 10.5. Then, 1 × 10⁻² M (1 mL) AgNO₃ solution was added dropwise and it was stirred for 25 minutes. To coat the silver colloids we followed the procedure reported by Wang *et al.*^[17] with minor modifications. Briefly, to the silver nanoparticles solution described above we added 150 mL ethanol, then we adjusted the pH back to 10.5 with the same NaOH solution, and then we added 200 μL of TEOS to the mixture. The mixture was allowed to stand at room temperature for 1 hour, and then it was centrifuged at 11000 rpm for 7 minutes, to concentrate the particles. SEM images were taken with the FEI Quanta 200 Environmental scanning electron microscope described at section 2.2.2. TEM images were obtained with the high resolution TEM instrument FEI Titan 80-300 described in section 2.2.1.

Langmuir monolayers of Octadecylrhodamine B dye (R18) mixtures with arachidic acid (n-eicosanoic acid) were prepared at the air-water interface of our Nima film balance (model 302M) described in section 2.4. We used a 1:10 mixture with arachidic acid as described in section 2.4.2 and as done previously.^[6,7,18] The Langmuir film was allowed to sit for ca. 30 minutes to ensure a complete evaporation of the solvent. The film was then compressed by a couple of moving barriers at a speed of 10 cm²/min. The Langmuir film is deposited onto a quartz slide under constant pressure to form the Langmuir-Blodgett (LB)

film for SHINEF experiments. The slides were cleaned using Piranha solution (7:3 mixture of sulfuric acid and hydrogen peroxide). UV-visible absorption spectra were recorded employing our Cary 50 scan UV-visible spectrophotometer described in section.

All Raman and fluorescence experiments were conducted using our micro-Raman Renishaw inVia system, with laser excitation at 514.5 and ca. 20 μW at the sample as described in sections 2.5.1 and 2.5.2. All measurements were made in a backscattering geometry, using either a 20 \times microscope objective probing an area of ca. 5 μm^2 , or a macro objective with an adapter for measurement in quartz cuvettes. 2D mapping results were collected through the rastering of a computer-controlled 3-axis encoded (XYZ) motorized stage, with a step of 5 μm . For the solution measurements, the concentration of CV was always 1.2×10^{-5} M, with a total of 1 mL being measured. We used increasing amounts of the concentrated nanoparticle (SHINs) solution until achieving a maximum SHINEF signal. For the enhancement factor calculations, we fit the Raman and fluorescence bands using the peak fitting function of the GRAMS program (Thermo Galactic Inc.), using one Gaussian curve for the Raman peaks and two for the fluorescence peaks, having previously done baseline and offset corrections.

Geometry optimizations and calculated Raman spectra were obtained using the Gaussian 09^[19] suite of programs, using density functional theory at the B3LYP/6-311+G(d,p) level of theory. No scaling factor correction was employed.

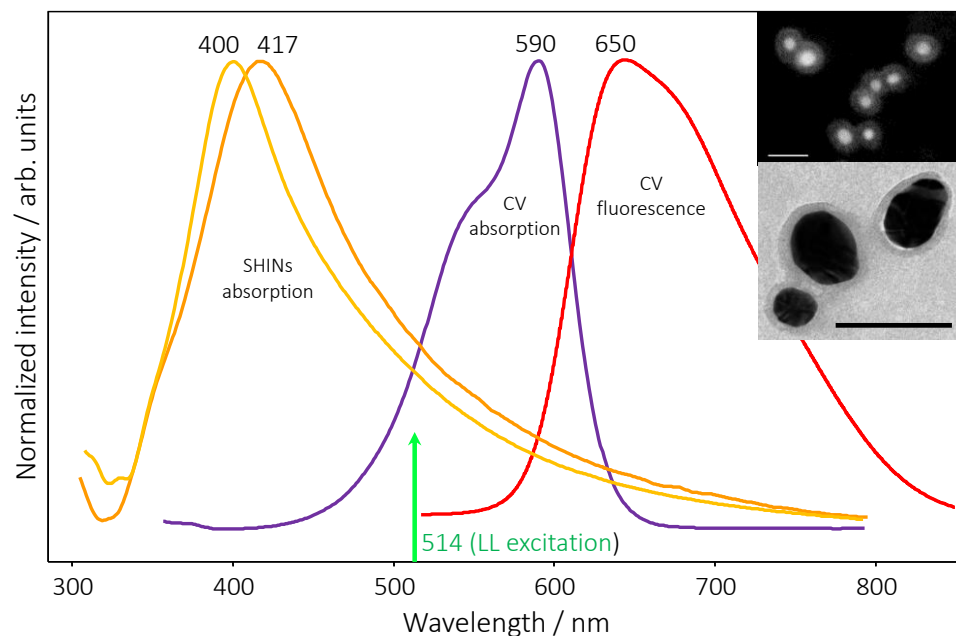


Figure 6.1. Characterization of the SHIN particles and the dyes employed. Absorption spectra of the silver particles before and after coating, along with the absorption and normal fluorescence spectra in aqueous solution of CV and the laser line excitation at 514.5 nm. Inset: SEM and TEM images of the coated particles. The bar in the images represents 100 nm in each case.

6.3. Results and Discussion

6.3.1. Ag-SHINs.

The plasmon absorption spectra of the silver SHINs before and after coating are shown in Figure 6.1, where the insets illustrate SEM and TEM images for the Ag-SHINs. Absorption peaks are due to the plasmon of the nanoparticles. The red shift of the absorption peak from 400 to 417 nm is consistent with a change in the dielectric medium due to the silica coating and the presence of ethanol. Electron microscopy images show particles deviating slightly from the spherical shape, to varying degrees of modification of the aspect ratio, but

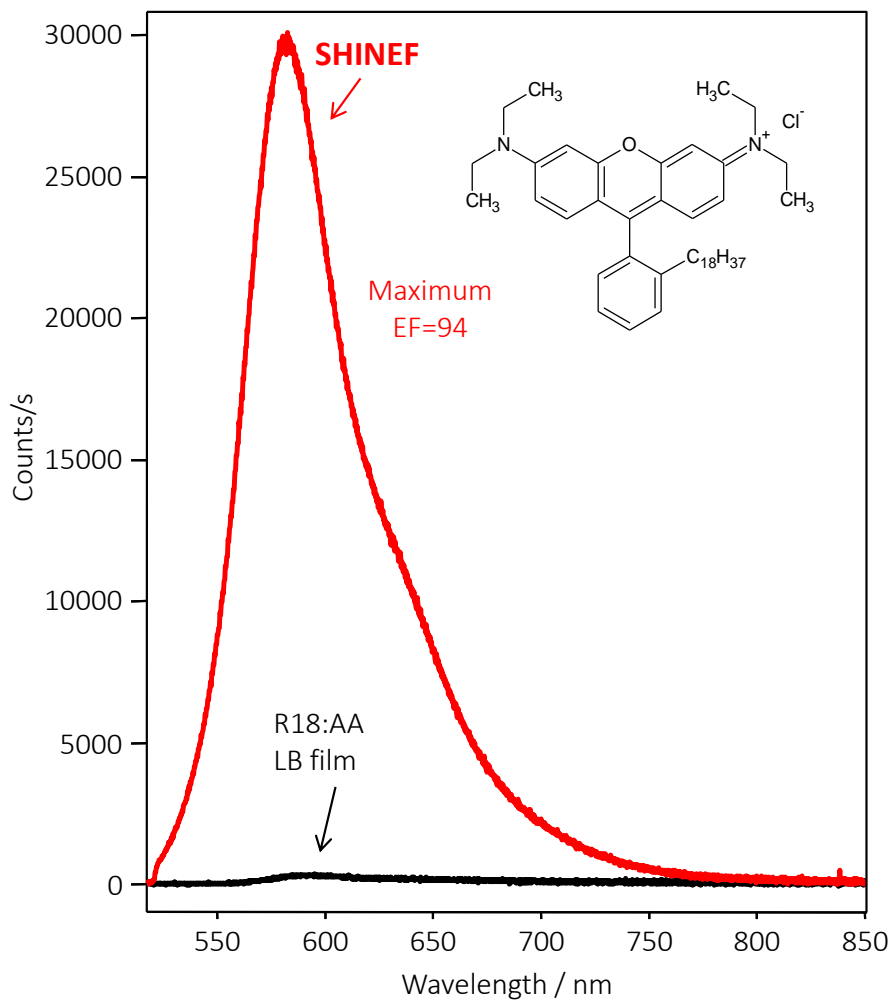


Figure 6.2. SHINEF of a R18:arachidic acid 1:10 mixed LB film using our silver SHINs, showing the maximum EF of 94.

always within 50-80 nm in diameter. SEM images clearly show that the particles are coated with silica. The TEM images confirm the SEM results for the silver cores with homogeneous silica coating around the silver nanoparticles, giving a shell thickness of approximately 6 nm in average.

The newly synthesized silver SHINs were first tested for SHINEF in conditions similar to our previous work.^[6,7,18,20] Namely, drops of the Ag-SHIN solution nanoparticles are cast onto a Langmuir-Blodgett film of R18 formed on a glass slide. The reference fluorescence and the SHINEF are shown in Figure 6.2, resulting in a maximum EF of 94, for SHINEF. Since casting does not provide a homogenous spreading, the EF varies on different sections of

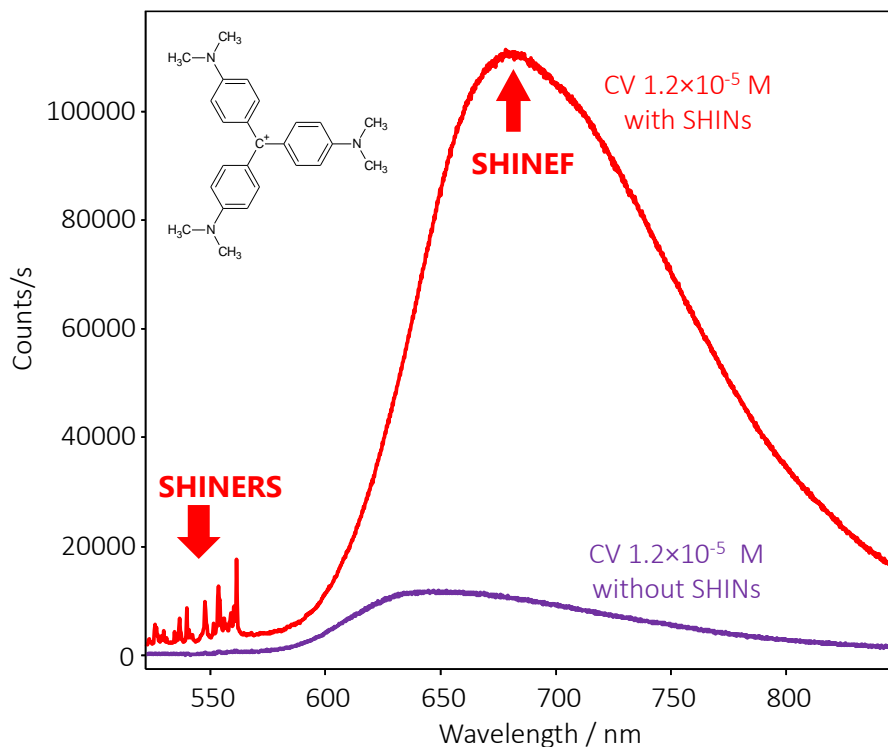


Figure 6.3. Combined SHINERS and SHINEF spectra for an aqueous solution of CV, and comparison with normal Raman and fluorescence spectra.

the LB films covered with Ag-SHINs, and 94 is an upper cotta. Given that R18 has a high intrinsic quantum yield, the strong fluorescence signal (SHINEF) does not allow seeing SHINERS for R18.

In a later repetition of this experiment (done long after the publication of our *Small* paper) in the same conditions using similar SHINs, we obtained a maximum enhancement factor of 100. This is shown in Figure 6.4. Repetition of the LB test for SHINEF with a mixed R18:AA LB film. Figure 6.4.

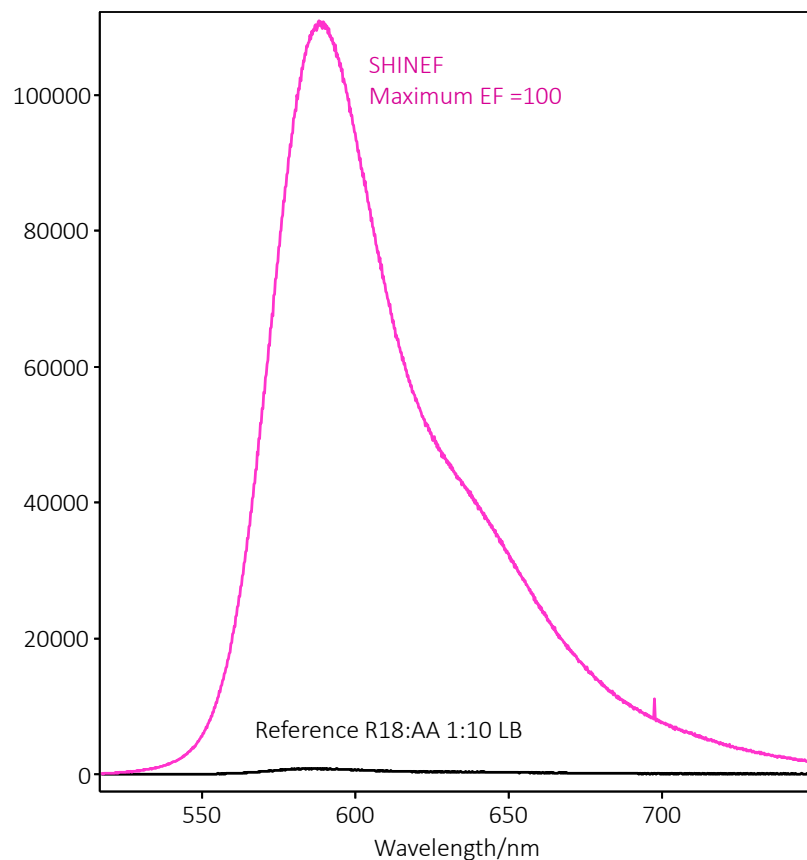


Figure 6.4. Repetition of the LB test for SHINEF with a mixed R18:AA LB film.

6.3.2. Local field enhancement in SHINERS and SHINEF.

The absorption and normal fluorescence of CV in aqueous solution, with a maximum absorbance peak at 590 nm and a “mirror image” fluorescence peak at 644 nm can be seen in Figure 6.1. As expected, the absorbance peak of CV shows a shoulder at around 550 which has been recently explained in terms of splitting of the E-symmetry of optically active states in polar solvents.^[21] The same experimental procedure was followed for all SHINERS/SHINEF measurements in solution: a volume of the CV solution was first measured (reference), and then aliquots of the Ag-SHIN solution were added until a plateau of enhanced intensity was achieved, and that is shown in Figure 6.3. The reference Raman scattering and fluorescence spectra of CV solutions without SHINs are also included in Figure 6.3. The advantage of exciting with the 514.5 nm laser line is that CV’s low quantum yield ($\sim 5 \times 10^{-5}$ in water)^[22-24] allows the observation of both Raman scattering and fluorescence in the same spectrum. There is a spectral window to observe the normal

Raman and SHINERS spectra between 514.5 nm and 600 nm (19436 cm^{-1} and 16436 cm^{-1}), after that the fluorescence or SHINEF spectra are recorded. At this point the Raman scattering of water in these aqueous solutions is prominent and interferes with the measurement at the beginning of the fluorescence bands, therefore it was removed from Figure 6.3 by spectral subtraction using the GRAMS software.

The normal Raman spectrum of CV shows all the corresponding bands of CV as previously investigated,^[21,25] which also agree very well with our own theoretical calculations (Figure 6.5), and the SHINERS spectrum does not show any significant modifications when compared to normal Raman spectrum. In the same manner, the fluorescence spectrum of CV shows a broad asymmetric peak with a maximum at $\sim 650\text{ nm}$ with a FWHM of 119 nm , while the SHINEF spectrum shows a maximum at 670 nm with a FWHM of 106 nm .

The EF calculations were obtained by dividing the integrated areas under the vibrational band at 1374 cm^{-1} in SHINERS over regular Raman, and similarly the integrated SHINEF band over that of the unenhanced fluorescence. The integration is performed using

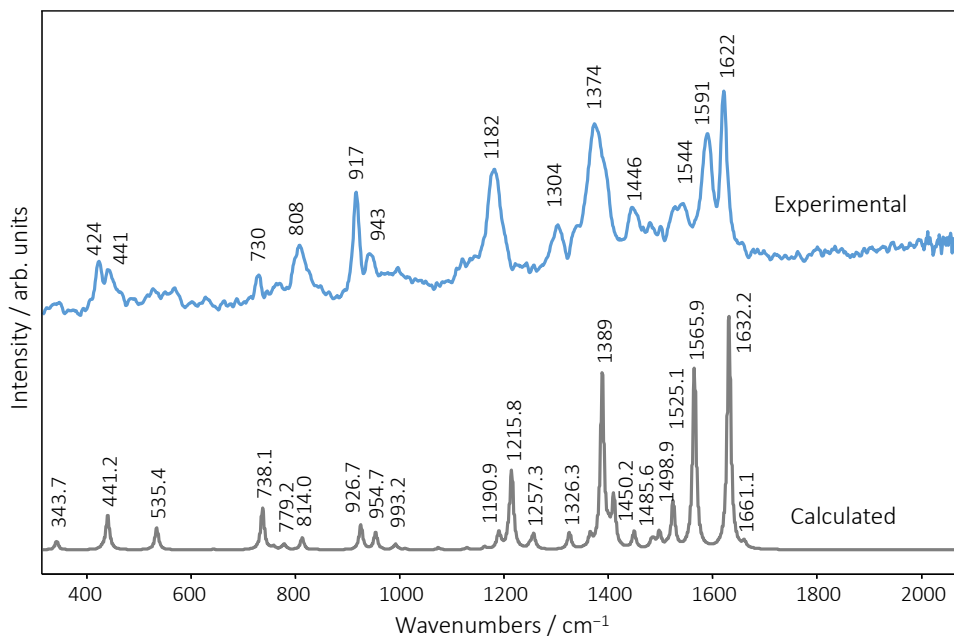


Figure 6.5. Comparison of the experimental CV SHINERS spectrum with a calculated spectrum for CV.

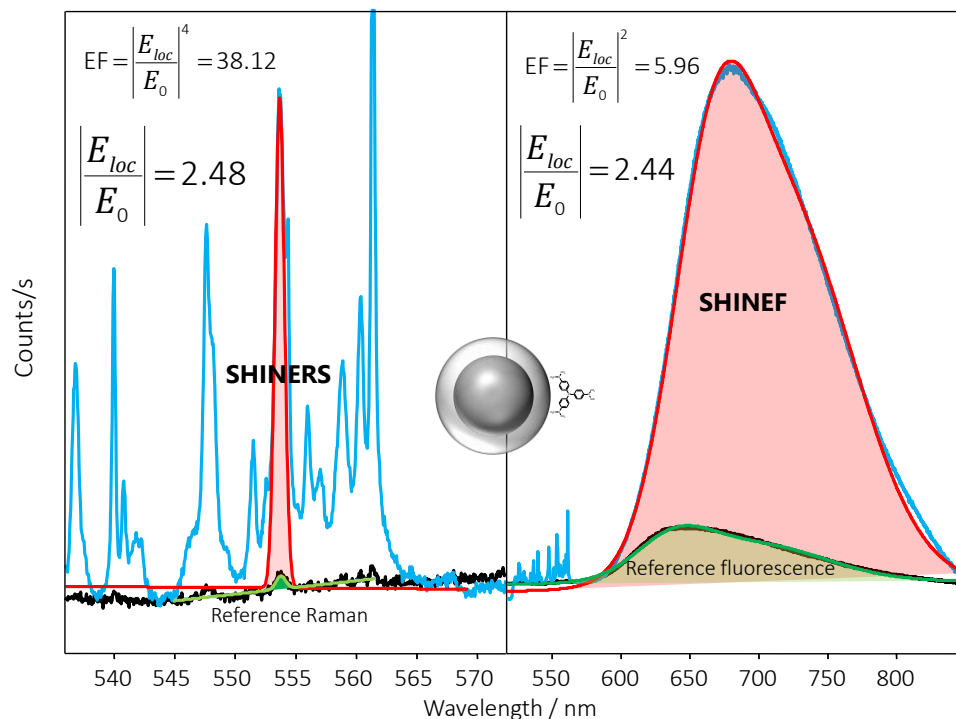


Figure 6.6. Theoretical fits and EF calculations for both SHINERS and SHINEF. The result proves the known E^2/E^4 relationship for SEF/SERS enhancement factors.

a Gaussian fit to the experimental spectra. Taking the fourth root of the SHINERS EF and the square root of the SHINEF EF yields comparable numbers: 2.48 and 2.44 respectively, as shown in Figure 6.6, which corresponds to the local field enhancement factor $|E|$. Notably, separate measurements of SHINERS and SHINEF with increasing concentrations of Ag-SHINs in solution always produce a field enhancement factor $|E|$ in keeping with the E^2/E^4 relationship, with minor differences well within the experimental error. Several examples are given in Table 6.1 (for the data published in our *Small* paper), and even more examples in Chapter 7 of this thesis.

SHINERS EF	$E_{loc} = \sqrt[4]{\text{SHINERS EF}}$	SHINEF EF	$E_{loc} = \sqrt{\text{SHINEF EF}}$
38.12	2.48	5.96	2.44
237.56	3.92	15.07	3.88
14.53	1.95	3.66	1.91
19.48	2.10	5.23	2.28

Table 6.1. Calculations for different repetitions of the SHINERS/SHINEF experiment.

It is important to reiterate that these results are for experiments carried out in solution (aqueous), a state that avoids clustering of nanoparticles and plasmon coupling, and, correspondingly, gives *average* values of the local field enhancement. The averaging in the solution measurements helps to obtain reproducible results in the far field that appear to reflect the local field enhancement at the Ag-SHINs. The selection of the 514.5 nm laser line that allows for the perfect separation of the SHINEF and SHINERS spectra is also in resonance with the tail of the plasmon and the molecular electronic absorption (Figure 6.1). In Chapter 7 we employ Malachite Green as a dye and excite with the 632.8 nm laser line; the SHINERS and SHINEF spectra overlap.

When casting the CV solutions, including the SHINs, over a quartz slide both SHINERS and SHINEF are still observed, as shown in Figure 6.7. However, the evaluation of the EF is complicated due to the lack of proper reference spectra, for when casting a CV solution

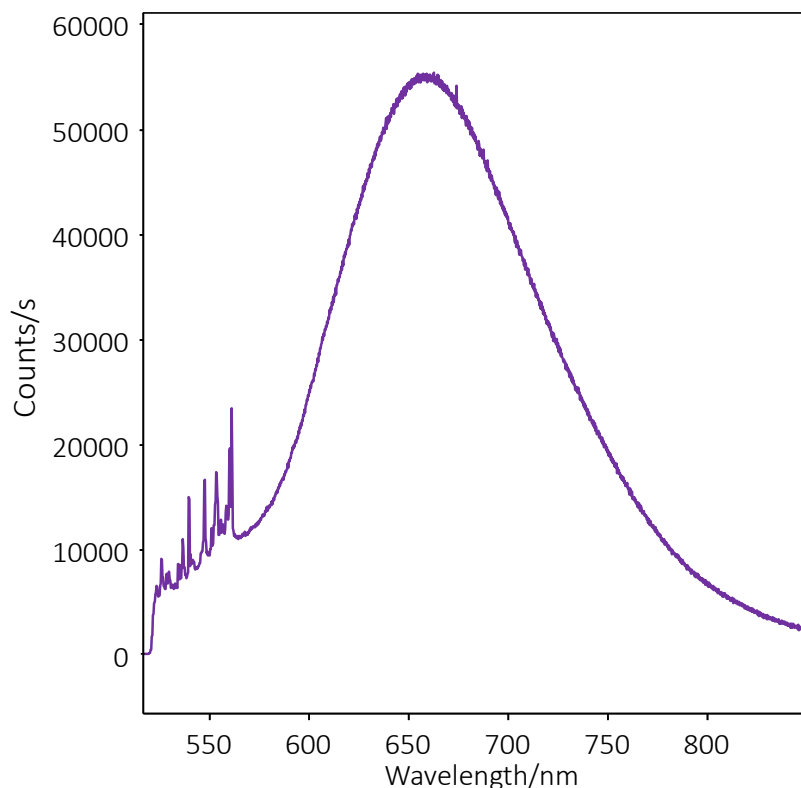


Figure 6.7. SHINERS and SHINEF spectra for a mix of SHINs and CV solution cast over a quartz slide.

one cannot obtain a homogeneous coverage like in an LB film, and here LB is out of the question because CV is soluble in water.

As an addition to the results presented in our *Small* paper, in Figures 6.8, 6.9 and 6.10 we show the spectra of SERS when using uncoated silver nanoparticles, with both the 514.5 nm and 632.8 nm laser lines, nBPTCD molecules, showing spectral profile modification in a similar way to that shown in Chapter 5, and we also show SHINEF with CV obtained with gold SHINs, that do not give anywhere near as much SHINEF/SHINERS when in aqueous solution.

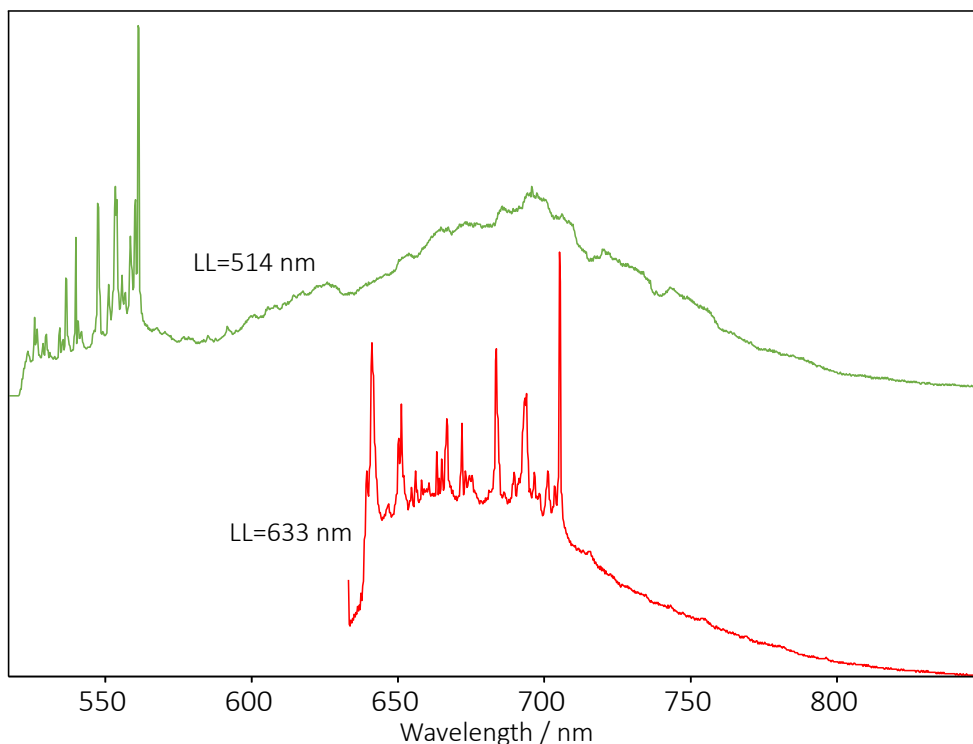


Figure 6.8. Spectra taken with uncoated Ag colloids. The spectrum in red was taken with the 514.5 nm Ar-ion laser line, and that below was taken with the 632.8 nm He-Ne laser line. The spectrum in green shows good SERS of CV but little fluorescence, which has been quenched by the naked nanoparticles. The red spectrum below also shows the SERS on top of the fluorescence band region.

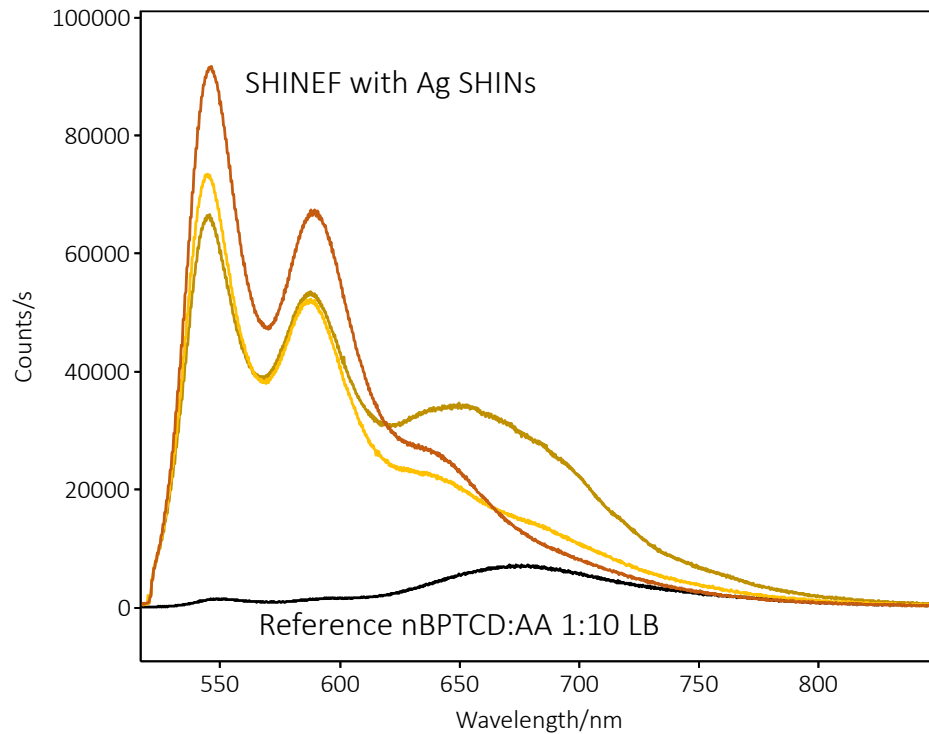


Figure 6.9. SHINEF of a LB film of nBPTCD:AA 1:10 with the new Ag-SHINs. This is similar to that presented in Chapter 4, but this time with Ag SHINs. The presence of the excimer is rarely encountered in the SHINEF (we show one example there) but it is always seen in the LB film without SHINs. This is another example of the spectral profile modification described in Chapter 5

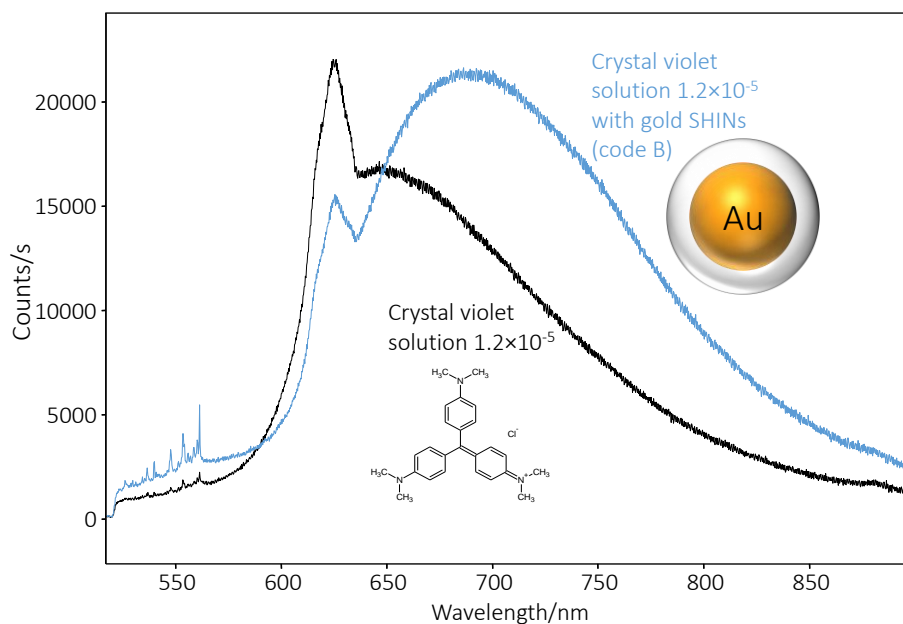


Figure 6.10. SHINEF of CV in aqueous solution with Au SHINs. The Au SHINs used here are the “code B” particles used for our *Angewandte Chemie* paper (see Chapter 4). The SHINEF EF cannot reach the values obtained with silver, because silver is a better EM enhancer than gold (section 1.4). Note also how the Raman scattering of water has not been subtracted here, showing a maximum at about 625 nm

6.4. Conclusions

Simultaneous recording of SHINERS and SHINEF for a low quantum yield molecule and experimental measurements in solution, provide direct evidence for a local field enhancement factor $|E|$ that in the far field gives surface enhanced fluorescence proportional to $|E|^2 = |E_{loc}/E_0|^2$, and surface enhanced Raman scattering proportional to $|E|^4 = |E_{loc}/E_0|^4$. In addition, it is shown that Ag-SHINs may provide larger enhancement factors that may help future developments in SHINEF applications.

6.5. References

1. Guerrero, A. R.; Zhang, Y.; Aroca, R. F. *Small* **2012**, *8*, 2964.
2. Kerker, M.; Wang, D. S.; Chew, H. *Appl. Optics* **1980**, *19*, 4159.
3. Moskovits, M. *Rev. Mod. Phys.* **1985**, *57*, 783.
4. Willets, K. A.; Van Duyne, R. P. *Annu. Rev. Phys. Chem.* **2007**, *58*, 267.
5. Li, J. F.; Huang, Y. F.; Ding, Y.; Yang, Z. L.; Li, S. B.; Zhou, X. S.; Fan, F. R.; Zhang, W.; Zhou, Z. Y.; Wu, D. Y.; Ren, B.; Wang, Z. L.; Tian, Z. Q. *Nature* **2010**, *464*, 392.
6. Guerrero, A. R.; Aroca, R. F. *Angew. Chem. Ger. Edit.* **2011**, *123*, 691.
7. Guerrero, A. R.; Aroca, R. F. *Angew. Chem. Int. Ed.* **2011**, *50*, 665.
8. Gersten, J.; Nitzan, A. *J. Chem. Phys.* **1980**, *73*, 3023.
9. Gersten, J.; Nitzan, A. *J. Chem. Phys.* **1981**, *75*, 1139.
10. Le Ru, E. C.; Etchegoin, P. G. *Chem. Phys. Lett.* **2006**, *423*, 63.
11. Schatz, G. C.; Van Duyne, R. P. In *Handbook of Vibrational Spectroscopy*; Chalmers, J. M., Griffiths, P. R., Eds.; John Wiley & Sons, Ltd: 2002; Vol. Volume 1, p 759.
12. Bharadwaj, P.; Novotny, L. *Opt. Express* **2007**, *15*, 14266.
13. Moskovits, M. *Nature* **2011**, *469*, 307.
14. Wokaun, A.; Lutz, H. P.; King, A. P.; Wild, U. P.; Ernst, R. R. *J. Chem. Phys.* **1983**, *79*, 509.
15. Chance, R. R.; Prock, A.; Silbey, R. In *Advances in Chemical Physics*; John Wiley & Sons, Inc.: 1978, p 1.
16. Leopold, N.; Lendl, B. *J. Phys. Chem. B* **2003**, *107*, 5723.

17. Wang, R.; Tang, J. G.; Liu, J. X.; Wang, Y.; Huang, Z. *J. Dispersion Sci. Technol.* **2011**, *32*, 532.
18. Aroca, R. F.; Teo, G. Y.; Mohan, H.; Guerrero, A. R.; Albella, P.; Moreno, F. *J. Phys. Chem. C* **2011**, *115*, 20419.
19. Frisch, M. J.; Trucks, G. W.; Schlegel, H. B.; Scuseria, G. E.; Robb, M. A.; Cheeseman, J. R.; Scalmani, G.; Barone, V.; Mennucci, B.; G. A. Petersson, H. N., M. Caricato, X. Li, H. P. Hratchian, A. F. Izmaylov, J. Bloino, G. Zheng, J. L. Sonnenberg, M. Hada, M. Ehara, K. Toyota, R. Fukuda, J. Hasegawa, M. Ishida, T. Nakajima, Y. Honda, O. Kitao, H. Nakai, T. Vreven, J. A. Montgomery, Jr., J. E. Peralta, F. Ogliaro, M. Bearpark, J. J. Heyd, E. Brothers, K. N. Kudin, V. N. Staroverov, R. Kobayashi, J. Normand, K. Raghavachari, A. Rendell, J. C. Burant, S. S. Iyengar, J. Tomasi, M. Cossi, N. Rega, J. M. Millam, M. Klene, J. E. Knox, J. B. Cross, V. Bakken, C. Adamo, J. Jaramillo, R. Gomperts, R. E. Stratmann, O. Yazyev, A. J. Austin, R. Cammi, C. Pomelli, J. W. Ochterski, R. L. Martin, K. Morokuma, V. G. Zakrzewski, G. A. Voth, P. Salvador, J. J. Dannenberg, S. Dapprich, A. D. Daniels, Ö. Farkas, J. B. Foresman, J. V. Ortiz, J. Cioslowski, and D. J. Fox; Gaussian, Inc.: Wallingford, CT, 2009.
20. Ross, B. M.; Lee, L. P. *Opt. Lett.* **2009**, *34*, 896.
21. Campo, J.; Painelli, A.; Terenziani, F.; van Regemorter, T.; Beljonne, D.; Goovaerts, E.; Wenseleers, W. *J. Am. Chem. Soc.* **2010**, *132*, 16467.
22. Baptista, M. S.; Indig, G. L. *J. Phys. Chem. B* **1998**, *102*, 4678.
23. Galloway, C. M.; Etchegoin, P. G.; Le Ru, E. C. *Phys. Rev. Lett.* **2009**, *103*.
24. Meyer, S. A.; Le Ru, E. C.; Etchegoin, P. G. *J. Phys. Chem. A* **2010**, *114*, 5515.
25. Kleinman, S. L.; Ringe, E.; Valley, N.; Wustholz, K. L.; Phillips, E.; Scheidt, K. A.; Schatz, G. C.; Van Duyne, R. P. *J. Am. Chem. Soc.* **2011**, *133*, 4115.

Chapter Seven

Exploring the Origin of the Observed SEF: A Study in Aqueous Solutions

The results presented in this chapter have not been published yet at the moment this thesis was submitted. The aggregation results are to be published soon.

7.1. Introduction

While not as ubiquitous as SERS, SEF does indeed generate quite a bit of research worldwide. A quick literature search using Web of Knowledge (Thomson Reuters Inc) for the keywords surface-enhanced fluorescence, metal-enhanced fluorescence, plasmon-enhanced fluorescence, and surface-enhanced phosphorescence (encompassing all plasmon-enhanced luminescence) yields the results shown below:

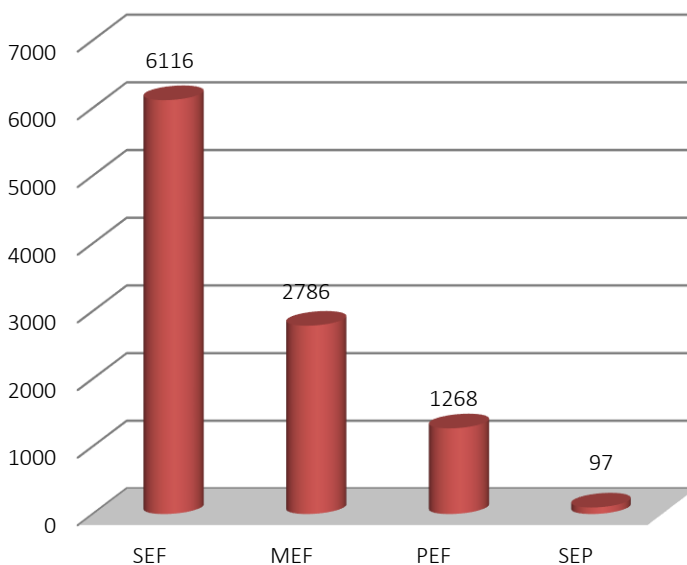


Figure 7.1. Number of results of plasmon-enhanced luminescence, separated by keyword.

More than thirty years after its first observation,^[1] the precise contributions that make up the observed SEF signal still generates an animated discussion. It is known that it is caused by the same plasmonic enhancement generating SERS, but it is clear that there are different processes at play, for in Raman there is no quenching or lifetimes of the processes. Then the question is not yet settled as to what is the origin of the radiation measured in the far field. Is it the fluorophore? Is it the radiating nanostructure? If both, what are the factors that control the magnitude of their contributions?

Let us recall again Moskovits (and collaborators') definition of SERS: "*As it is currently understood SERS is primarily a phenomenon associated with the enhancement of the electromagnetic field surrounding small metal (or other) objects optically excited near an intense and sharp dipolar resonance such as a surface plasmon polariton. The enhanced re-radiated dipolar fields excite the adsorbate, and if the resulting molecular radiation remains at or near resonance with the enhancing object, the scattered radiation will again be enhanced (hence the most intense SERS is really frequency-shifted elastic scattering by the metal). Under appropriate circumstances the field enhancement will scale as E^4 where E is the local optical field.*"^[2] This is extended to SEF in the sense that we are observing the elastic scattering (of fluorescence) by the metal. Like its cousin SERS, SEF also has a component due to the re-radiated dipolar field. But there are several aspects in the observed SEF that require special attention.

7.1.1. Properties of the Fluorophore

We start this discussion with the characteristic properties of a fluorophore, namely the fluorescence lifetime and the quantum yield. Before the discovery of SEF, it was Chance, Prock and Silbey^[3] who in 1978 first described theoretically the interaction of molecules with metallic surfaces. The quenching of the fluorescence signals is accompanied by a significant reduction in the fluorescence lifetimes. "*The decrease in the lifetime when the distance become small is due to nonradiative transfer of energy from the excited molecule to the metal. (...) It has been shown that the surface-plasmon modes of the metal dielectric interface are those that couple to the near field of the emitting molecule*".^[3] Therefore, the

most relevant idea in this classical report is the *coupling of excited molecules to surface plasmons*. Their model explained well the observations previously made by Drexhage^[4] of a fluorescent europium complex, separated from the metallic surface by several monolayers of fatty acids delivered by LB deposition.

When changing from plane metallic surfaces to coinage metal nanoparticles to produce SEF, we switch from plane metal surface plasmons to localized surface plasmon resonances (LSPR),^[5] which we discussed previously. The reduction in the lifetime remains a consistent observation in almost every SEF experiment in the literature. For instance, looking at the SEF reports published between 2011 and 2013,^[6-37] in almost all cases, the lifetime decreases when compared to the normal (in the absence of nanostructures) fluorescence lifetime. This is usually described relating it to the quantum yield. Let us recall from Chapter 1 the expressions for both:

$$\Phi = \frac{\Gamma}{\Gamma + k_{nr}} \quad (7.1)$$

$$\tau = \frac{1}{\Gamma + k_{nr}} \quad (7.2)$$

where Γ is the radiative decay rate and k_{nr} is the non-radiative decay. The difference is that in metallic surfaces the plasmons are non-radiative and result in fluorescence quenching, while in the case of metallic nanostructures the plasmons are radiative and the fluorescence can be enhanced.^[38] This quenching of the molecular fluorescence leads to the fundamental property of the observed SEF, the **molecule-metal distance dependence**.^[39,40] In Chapter 6^[41] we demonstrated using far field measurements of scattering and fluorescence from the same molecular system that the scattering scales as the fourth power of the local field enhancement while the fluorescence is proportional to the square of the local field enhancement. These results can only be obtained at a metal-molecule separation where the quenching is negligible.

For the isolated molecule, the quantum yield determines what portion of this energy is reemitted as fluorescence (chapter 1), and the observed light intensity is:^[42]

$$I_0 = I_{exc} \cdot \varepsilon(\omega) \cdot \Phi_0 \quad (7.3)$$

Electromagnetic coupling between the fluorophore and the nanostructure modulates the decay rate Γ by a factor χ , which we append to the decay rate in equations (7.1) and (7.2). The presence of the metal will change the quantum yield, giving:

$$\Phi_{SEF} = \frac{\chi\Gamma}{\chi\Gamma + k_{nr}} \quad (7.4)$$

$$\tau_{SEF} = \frac{1}{\chi\Gamma + k_{nr}} \quad (7.5)$$

In the case of excitation of LSPR, the local field enhancement (Chapter 6) is: $|E| = |E_{loc}/E_0|$. For our shell-isolated nanoparticles (SHINs), the k_{nr} remains unchanged due to the silica coating. Therefore, the observed fluorescence ratio would be:^[42]

$$\frac{I_{SEF}}{I_0} = \langle |E|^2 \rangle \frac{\Phi_{SEF}}{\Phi_0} = \langle |E|^2 \rangle \frac{\chi(\Gamma + k_{nr})}{\chi\Gamma + k_{nr}} \quad (7.6)$$

Equation (7.6) can be used to discuss the results obtained in SHINEF, that is, the regime when metal quenching is not a major factor. There are, however, experimental results that may require further refinements of the theory for a full understanding of the components that make up the observed enhanced signal.

From these expressions one obtains that in SEF the quantum yield Φ increases and the lifetime τ decreases. The problem is that these expressions set a limit as to how much fluorescence can be enhanced, that being the intrinsic quantum yield of the fluorophore; it cannot emit more photons than it absorbs. This would imply that fluorophores with a low quantum yield like crystal violet would be the most benefited from SEF, and those with a quantum yield approaching unity, like Rhodamine 6G, should not be very likely to produce any SEF. However, this is in open contradiction with experimental evidence: published data indicates that both high and low quantum yield molecules can produce SEF, case in point our own reports from Chapters 4 and 5. In those cases the enhancing nanostructure must play a role not accounted for in this description.

There are also reports of enhanced excitation of the molecule by the nanoparticle that leads to enhanced absorption.^[43] More absorption may lead to more emission.

7.1.2. Role of the nanostructure

The nanostructure is, of course, at the heart of SEF observation. Probably the most important property to discuss is the effect that comes from the contribution of spatial locations with extremely high concentration of the local field, what constitutes a *hot spot*.^[44] There is experimental evidence that hot spots may bring about unusually high enhancement factors in SEF, similar to their known effect for SERS. Gill and Le Ru^[45] have described it for nanoparticle aggregates in a silver island film, with EF values of up to 740 for Rhodamine 6G-labeled DNA. They also make the case that under the conditions of hot spots it should be possible to obtain high EF values even for high quantum yield molecules. Kinkhabwala *et al.* has also observed large enhancements from bowtie-like nanoparticles^[46] reporting an EF of 1,340 for dye in the near infrared, and Zhang *et al.* have even reported an EF of 2,970 for indocyanine green using a nanopillared architecture device.^[47]

It has also been demonstrated experimentally that the nanostructure can modify the spectral profile of the observed enhanced fluorescence, giving rise to what has been termed spectral profile modification (SPM). Le Ru and Etchegoin observed that for several fluorophores, their emission profile is modified by the plasmon that enhances it, to the point that the original shape of the fluorophore may not be recognized, using differently-shaped nanolithographic substrates.^[48] Indeed this motivated our own investigation into that subject, which was described in Chapter 5, and indeed we showed the spectral profile modification of the fluorescence of a perylene dye when enhanced by two different nanoparticles with different plasmon absorptions and scattering.^[49] Similarly, plasmon and emission tuning is recommended to maximize the enhancement efficiency.^[50] LSPR have normally a much broader FWHM than molecular bands.

In our own previous report^[41] (Chapter 6 of this thesis) we demonstrated for experiments carried out in aqueous solution, using far field measurements of scattering and fluorescence from the same molecular system, that the scattering scales as the fourth power of the local field enhancement while the fluorescence is proportional to the square of the local field enhancement.

In this Chapter we discuss the results of our study of several factors affecting the observed SEF, using as enhancing nanostructures the shell-isolated nanoparticles (SHINs) described first in Chapter 4,^[51,52] performing all the study in aqueous solution, in a similar fashion to what we described in Chapter 6.^[41]

7.2. Materials and Methods

Crystal violet (CV, total dye content 90%) was purchased from Fisher Scientific. Malachite green, Eosin Y and Pyronin Y (Total dye content 50%) were purchased from Sigma-Aldrich and used as received. Unless otherwise specified, solutions are aqueous and the water employed is Milli-Q quality (18.2 M Ω -cm). All glassware was cleaned using aqua regia and rinsed with abundant Milli-Q water.

The core silver colloids were prepared by reduction of silver nitrate with sodium citrate, similarly to the classical Lee-Meisel method.^[53] 18 mg of AgNO₃ were dissolved in 100 mL of water, and the solution was brought to a vigorous boil for approximately one hour. After that, the solution was removed from the heat and 6 mL of a 1 mM solution of 3-aminopropyltriethoxysilane (APTES) was added. Then it was let to stir for approximately half an hour, and then it was brought to a boil and was added 24 mL of activated sodium silicate solution 0.54% w/v. The activation is done by bringing the pH of the solution down from its original pH (>11) to 10.5 by adding the beads of an acidifying resin (Amberlite IR-120). The boiling was continued for 3 hours. Finally, the resulting SHIN particles were centrifuged at 12000 rpm for 7 minutes, to concentrate the particles, reducing 36 mL of the original colloid to two 1.5 mL microcentrifuge tubes. Aliquots of this concentrated dispersion were used for the solution SHINEF experiments. For the experiment with Sulforhodamine B, since the dye has a negative charge we further functionalized the SHINs, taking 50 mL of the original colloidal solution and adding 3 mL more of APTES 1 mM solution, and then we filtered and centrifuged the solution in the same manner described.

UV-visible absorption spectra were recorded employing our Varian Cary 50 scan UV-visible spectrophotometer described in section 2.5.3 of Chapter 2.

All Raman and fluorescence experiments were conducted using our micro-Raman Renishaw inVia system, with laser excitation at 514.5 nm. All measurements were made in a backscattering geometry, using a macro objective with an adapter for measurement in quartz cuvettes, displayed in Chapter 2 section 2.5.1. The mount for the cuvette was fixed to the microscope stage to make sure the focusing of the laser was the same for all measurements, and ensure their reproducibility.

For the experiments with dyes, the concentration of the dye was always constant, with a total of 1 mL being measured. In this case, for different experiments we used different concentrations of dye, but for a same set of experiments, the concentration was kept constant. We used increasing amounts of the concentrated nanoparticle (SHINs) adding various amounts.

For the enhancement factor and quantum yield calculations, we fit the absorption, Raman and fluorescence bands using the peak fitting function of the GRAMS program (Thermo Galactic Inc.), using one Gaussian curve for the Raman peaks and three for the absorption and fluorescence peaks, having previously done baseline and offset corrections.

The calculation of quantum yield was done using the comparative method used typically,^[54,55] using aqueous solutions of Eosin Y dissolved in a 0.1 M NaOH solution as a comparison standard, which has a known literature value of 0.19.^[55,56] In the experiments where we calculated quantum yield we employed the formula:

$$\Phi_{sample} = \Phi_{ref} \times \frac{I_{sample}}{I_{ref}} \times \frac{\mathcal{E}_{ref}}{\mathcal{E}_{sample}} \times \frac{n_{sample}^2}{n_{ref}^2} \quad (7.7)$$

where Φ are the quantum yields for the sample and the reference, I are the fluorescence intensities (expressed as area-under-the-curve; we obtained these by peak-fitting Gaussian curves in GRAMS), and \mathcal{E}^* are the extinction values for the molecules. We took these as the areas under the curve for the fluorescent molecules also, which we always ran between 300 and 800 nm; finally, n are the refractive indices of the solvents for the sample and the reference. Since we always used water as solvent, we took these these values as equal. Indeed the difference between the refractive index of water and that of a 0.1 M NaOH

* Here we employed handwritten uppercase to distinguish it from the electric field.

solution is negligible (0.72% difference from distilled water, as measured by Panda *et al.*^[57]). The measurements were done in a quartz cuvette (Hellma Analytics), recording first the absorption spectrum in our Varian Cary 50 spectrometer and then taken immediately to our Renishaw inVia instrument for the measurement of fluorescence. Between measurements the cuvette was cleaned with copious Milli-Q water and then blow-dried with air.

7.3. Results and Discussion

7.3.1. Characterization of the SHINs and absorption of MG and CV

Sample absorption spectra of the SHINs employed for the experiments in this chapter are shown in Figure 7.2, compared to the absorption spectra of the low-quantum yield dyes, crystal violet (CV) and malachite green (MG). The first batch of SHINs with the maximum at 404 and a shoulder at ca. 450 was employed for the excitation power comparison and quantum yield measurements. The second batch with a maximum at 424 nm was that employed in the NaCl aggregation experiments (section 7.3.6). SEM images for both batches are very similar; the particle size was at an average of ca. 75 nm but there were many outliers in terms of sizes and shapes. This is a characteristic of the silver-citrate reduction method. For this set of experiments, we preferred this method over the silver-hydroxylamine method we had used previously, as this method gives more stable particles that can be used for more experiments. We synthesized a new batch for the aggregated colloid experiments, as the first batch was used in its entirety. The coatings were more regular though, being around 10 nm for the two batches synthesized using the same procedure.

CV shows a maximum of extinction at 591 nm and MG at 617. The 514.5 nm laser line excitation falls right at the beginning of the absorption peak making the excitation right in resonance. It falls slightly off the absorption peak of MG, but it is well in resonance with the excitation of the 632.8 nm laser line

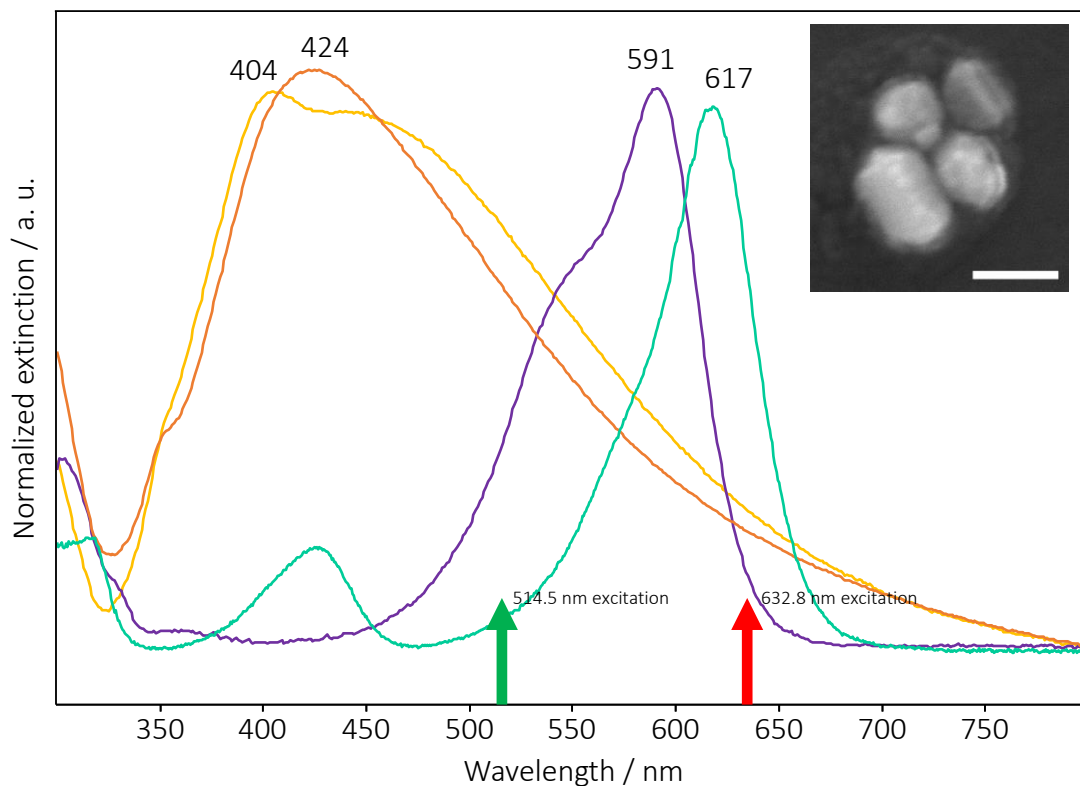


Figure 7.2. Characterization of the Ag SHINs and the CV and MG dyes. The yellow traces are the two batches of colloids, the violet line is CV, and the cyan trace is MG. Inset: SEM picture of the SHIN particles employed. The scale bar represents 100 nm.

7.3.2. Local field SERS/SEF relationship

First, we added increasing amounts of the solution of CV, in a similar way as we did in our previous report (Chapter 6^[41]). The concentration of CV in solution at all times was 1.2×10^{-5} M. Figure 7.3 shows the spectra of the SHINEF obtained, and Table 7.1 shows the enhancement factors and the fulfillment of the E^2/E^4 relationship as described before.

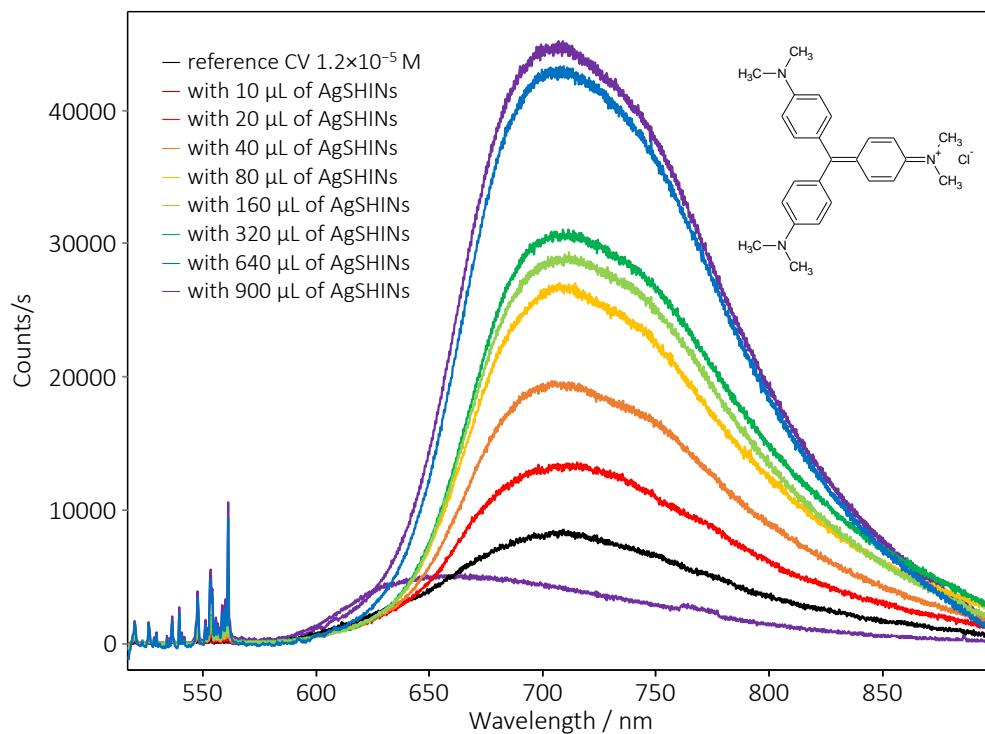


Figure 7.3. SHINEF of CV in solution with increasing amounts of SHINs, using the 514.5 nm laser line.

μL SHINs added	SHINERS EF	E_{loc} $= \sqrt[4]{\text{SERS EF}}$	SHINEF EF	E_{loc} $= \sqrt{\text{SEF EF}}$	E_{loc} percent diff.
10	4.23	1.43	1.62	1.27	11.8
20	7.71	1.67	2.38	1.54	7.72
40	13.7	1.92	3.43	1.85	3.74
80	18.3	2.06	4.53	2.13	2.69
160	25.1	2.24	5.31	2.30	2.90
320	24.0	2.22	5.07	2.25	1.73
640	60.4	2.79	7.61	2.76	1.05
900	65.2	2.84	7.92	2.81	0.979

Table 7.1. SHINERS and SHINEF enhancement factors and local field calculations for CV. LL=514.5 nm.

The agreement between the two calculated E_{loc} is good, with the percent difference between the two $((a - b)/\frac{(a+b)}{2}) \times 100$ diminishing dramatically after 40 μL of SHINs are added.

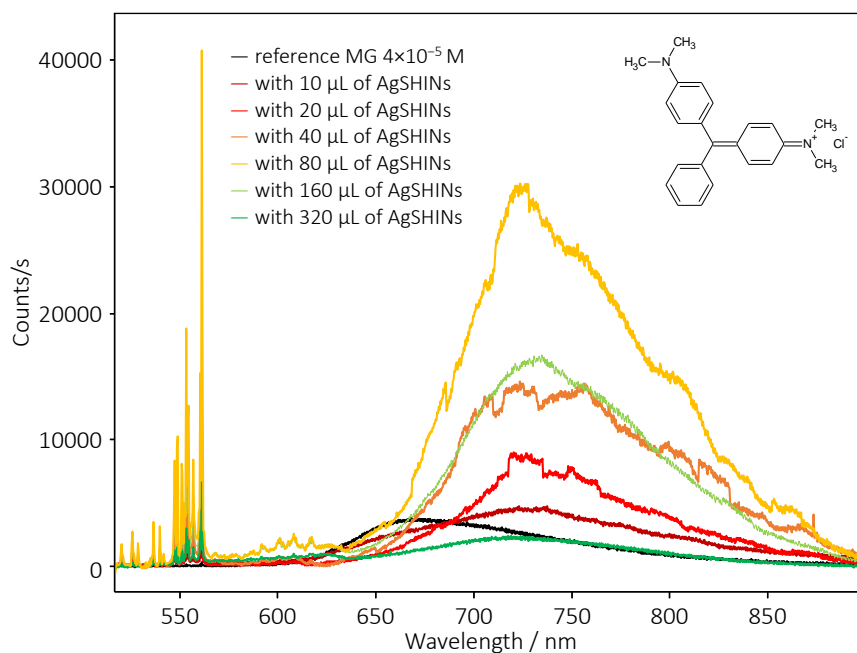


Figure 7.4. SHINEF of MG in solution with increasing amounts of SHINs, using the 514.5 nm laser line.

We also performed the same experiment using malachite green, at a concentration of 4×10^{-5} M that was kept constant for the full series of experiments. In this case, we employed both 514.5 nm and 632.8 laser lines, which gave different results. These are shown in Figures 7.4 and 7.5, and Tables 7.2 and 7.3. With the 514.5 nm laser line, the SEF enhancement was comparable to that obtained for CV, but the Raman enhancement was much higher. This is explained by the fact that the excitation laser line is further away from the centre of the absorption peak. The local field relationship is not held. However, the situation is different when exciting with the 632.8 nm laser line.

μL SHINs added	SHINERS EF	$E_{loc} = \sqrt[4]{\text{SERS EF}}$	SEF EF	$E_{loc} = \sqrt{\text{SEF EF}}$	E_{loc} percent diff.
10	8.33	1.70	1.41	1.19	35.6
20	29.1	2.32	1.94	1.39	50.2
40	47.4	2.62	3.63	1.91	31.7
80	124	3.34	7.19	2.68	21.8
160	88.8	3.07	4.09	2.02	41.1
320	21.4	2.15	0.61	0.78	93.5

Table 7.2. SHINERS and SHINEF enhancement factors and local field calculations for MG. LL=514.5 nm.

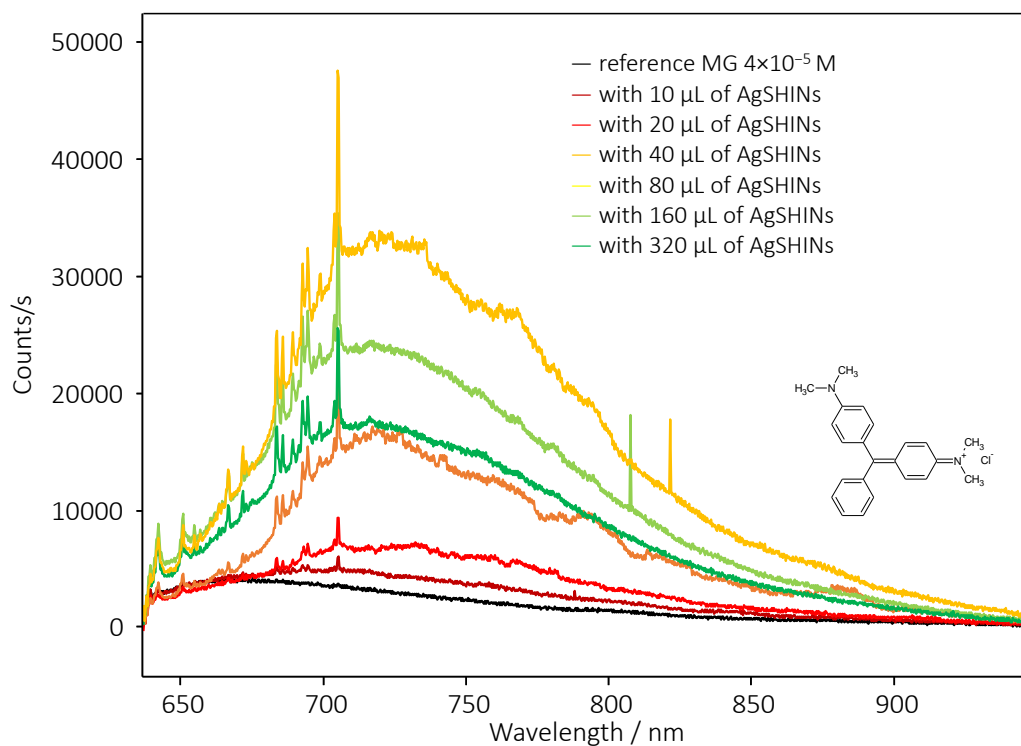


Figure 7.5. SHINEF of MG in solution with increasing amounts of SHINs, using the 632.8 nm laser line.

μL SHINs added	SHINERS EF	$E_{loc} = \sqrt[4]{\text{SERS EF}}$	SHINEF EF	$E_{loc} = \sqrt{\text{SEF EF}}$	E_{loc} percent diff.
10	3.73	1.39	1.37	1.17	16.9
20	11.1	1.82	1.88	1.372	28.4
40	27.6	2.29	3.91	1.98	14.8
80	65.4	2.84	8.21	2.87	0.765
160	49.3	2.65	6.15	2.48	6.65
320	36.5	2.45	4.58	2.14	13.8

Table 7.3. SHINERS and SHINEF enhancement factors and local field calculations for MG. LL=632.8 nm.

At the point of maximum enhancement, the percent difference between the two local field calculations is very small indeed; therefore one observes that the E^2/E^4 relationship holds when the excitation laser line is in resonance with the electronic absorption of the molecule.

7.3.3. Excitation power

We performed the experiment of CV SHINEF with the 514.5 nm laser line at different powers, to see whether they had any impact in the SEF EF. The result is shown in Table 7.4.

		Excitation power (μW)			
		21.6	40.3	134	1410
μL particles added	10	2.19	1.40	1.54	1.62
	20	2.52	2.52	2.89	2.38
	40	3.84	3.20	4.04	3.43
	80	4.00	4.04	4.67	4.52
	160	5.17	5.17	5.37	5.31
	320	5.65	4.59	5.34	5.07
	640	7.44	6.93	8.19	7.61
	900	7.54	6.55	8.13	7.92

Table 7.4. SHINEF EF as a function of the amount of SHINs added and excitation power.

The EF values do not show a noticeable trend; the fairest conclusion is that the excitation power does not seem to have much of an impact in the enhancement factor that is possible to achieve. The result helps to understand the factor of direct excitation. If direct excitation plays a key role in the observed SHINEF, there should be a direct correlation between incident power and observed enhancement.

7.3.4. Quantum Yield and Absorption Enhancement

We performed first these measurements with CV, in similar conditions to the previous experiment, only we adjusted the concentrations of both the standard and the sample fluorophore so we could measure correctly the absorption and the fluorescence using the same excitation power. For that reason, in this part we worked with CV at half of the concentration of the previous experiments, that is, at 6×10^{-5} M. In these cases we measured both absorption and fluorescence for the solutions.

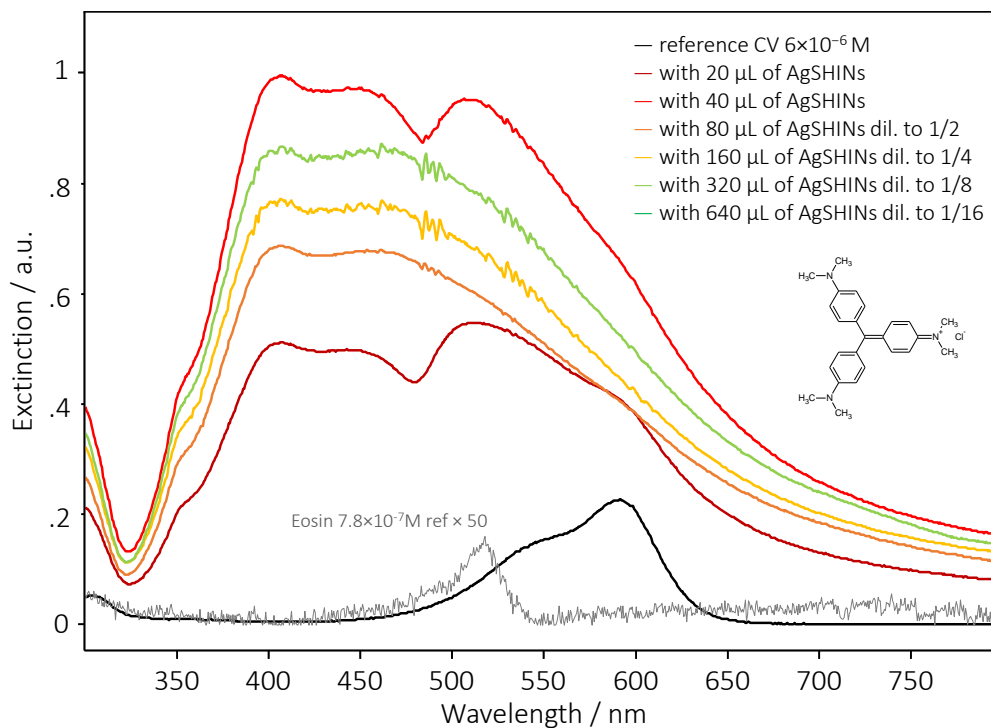


Figure 7.6. Extinction spectra of CV 6×10^{-6} M with SHINs added, to study the effect of quantum yield.

The plot of the extinction spectra for the CV with SHINs is shown in Figure 7.6. When adding the SHINs to the dye solution, the high extinction coefficient of the nanoparticles saturate quickly the spectrometer, and because of that we diluted the solutions where the absorption was too intense. That intensity also makes it hard to see the CV at all beyond 80 μL of SHINs added; after that, only the SHINs' extinction is seen. Indeed, if we subtract the absorption of the SHINs (Figure 7.7), it is possible to see what happens to the CV dye. The secondary peak of CV, the "shoulder" becomes much more prominent when CV is adsorbed to the SHINs. But between 20 and 40 μL of SHINs added, the area under the curve is very similar indeed, which shows the way to conclude that most likely there is no enhancement of the absorption detected in the SHINEF in solution for CV.

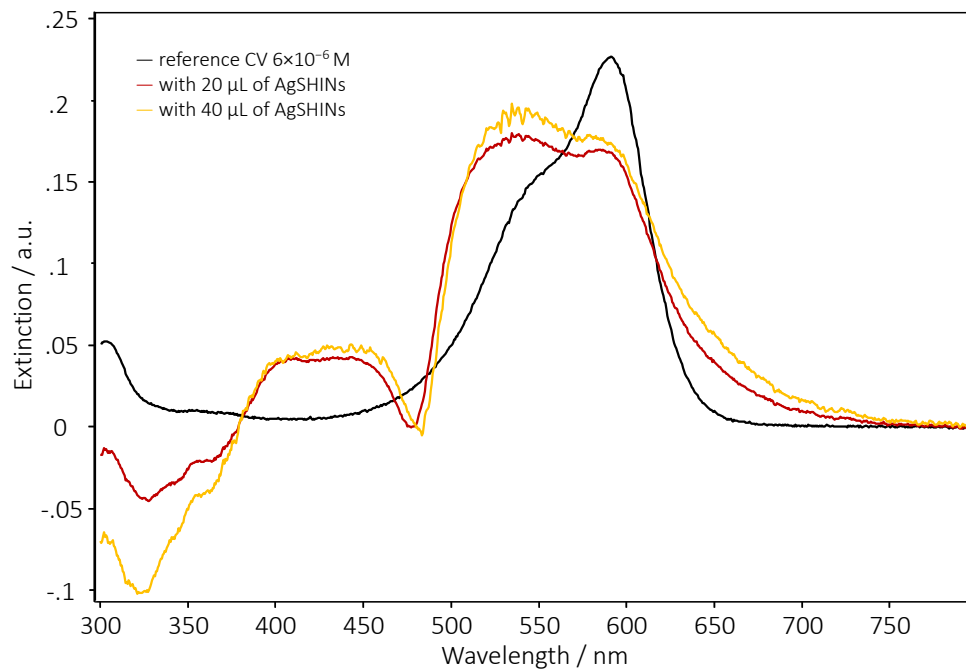


Figure 7.7. Extinction spectra of CV 6×10^{-6} M with 20 and 40 μL of SHINs added, after subtraction of the SHINs.

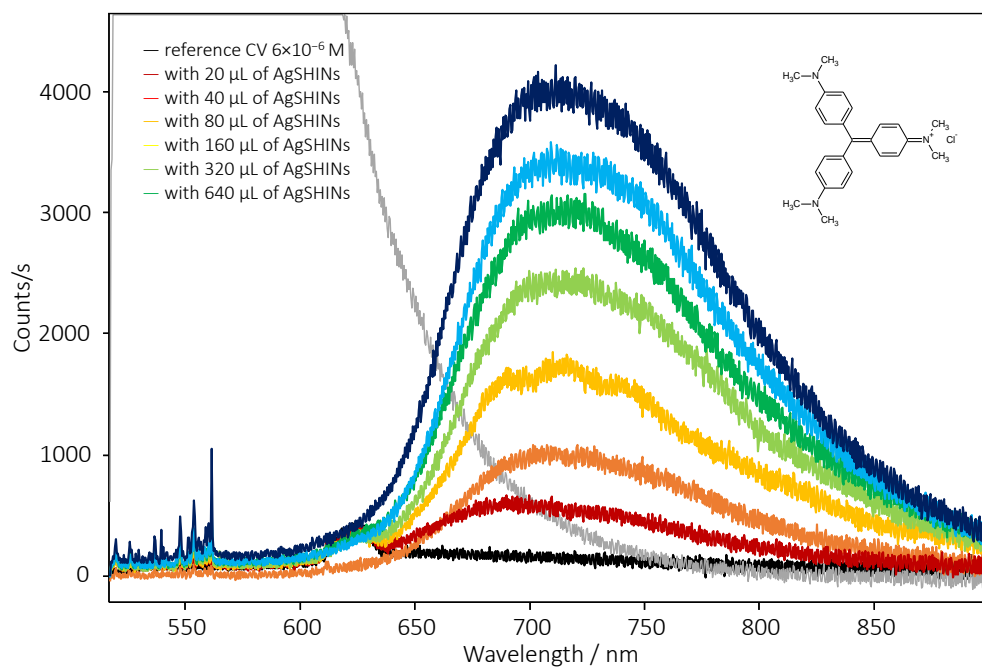


Figure 7.8. Fluorescence spectra of CV 6×10^{-6} M measuring quantum yield. The gray trace is the fluorescence of Eosin Y.

Fluorescence spectra of CV 6×10^{-6} M are plotted in Figure 7.8. The quantum yield can be reliably calculated only for 20 and 40 μL of SHINs added, after subtracting the extinction of the SHIN particles. Beyond that, the nanoparticles' extinction overwhelms that of CV and the quantum yield cannot be calculated reliably. The values provided below for quantum yield assume the average of the area under the curve for the absorption of CV, for 20 and 40 μL of SHINs added. Since those values are very similar, it could be reasonable to assume the same area to calculate the quantum yield in the rest of the solutions.

μL added	SHINEF EF	QY	QY EF
0 (ref CV)	-	2.57×10^{-5}	-
20	8.79	1.78×10^{-4}	6.94
40	13.6	2.80×10^{-4}	10.9
80	19.7	4.06×10^{-4}	15.8
160	24.7	5.09×10^{-4}	19.8
320	28.7	5.92×10^{-4}	23.0
640	33.8	6.97×10^{-4}	27.1

Table 7.5. CV SHINEF EF, quantum yields and QY enhancement factors with increasing amounts of SHINs added. Results with 80 μL and above are greyed out as the quantum yield was calculated with an estimated area.

The calculated quantum yield for CV of 2.57×10^{-5} is in fair (given how low it is) agreement with the literature value of $\sim 5 \times 10^{-5}$.^[58-60] It is noticeable that the increase in quantum yield (QY) follows closely the SHINEF EF, and the discrepancy may be due only to the ascent of the shoulder of CV when adsorbed to silica.

We performed a similar experiment with MG to measure the QY. This time we excited with the 514.5 nm laser line only, because that is the one that excites the reference Eosin Y, at the concentration of 2×10^{-4} M. This is shown in Figures 7.9 to 7.11 and Table 7.6. As we can see in Figure 7.10, after the subtraction of the SHINs, the area under the curve is almost exactly the same as that of MG alone. The picture here is clearer because there is less overlap between the extinction of the SHINs and that of the dye. For the same reason, this time the SEF EF matches much more closely to the QY EF, they are indeed the same.

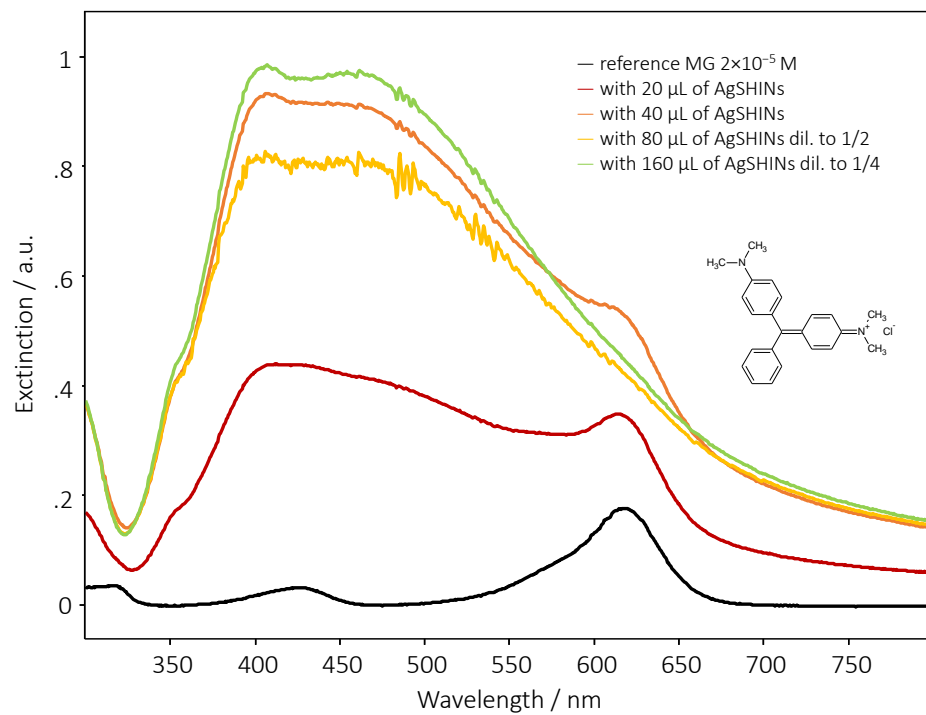


Figure 7.9. Extinction spectra of MG with SHINs added, to study the effect of quantum yield

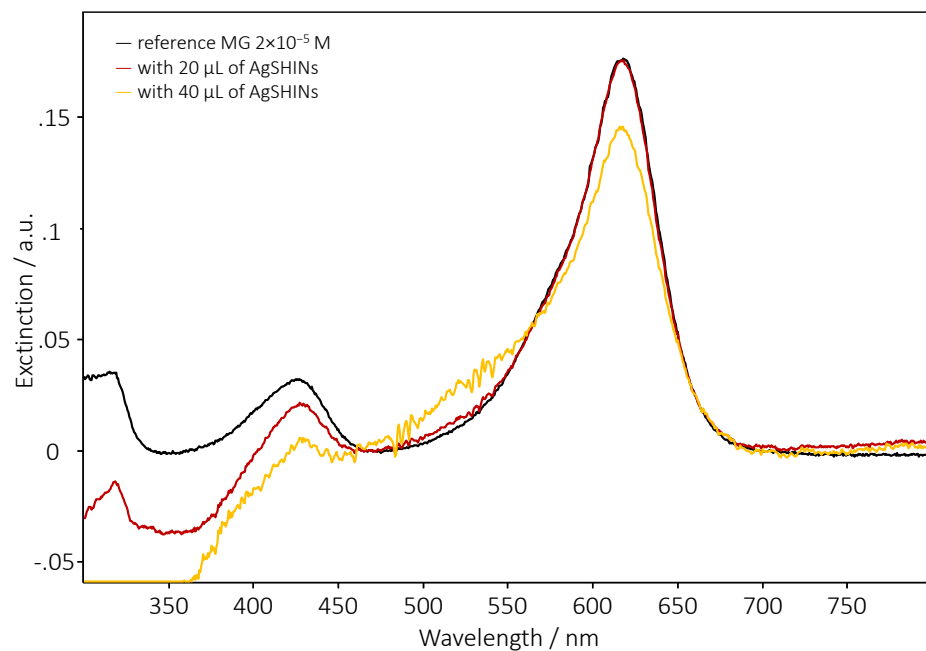


Figure 7.10. Extinction spectra of MG 2×10^{-5} M with 20 and 40 μL of SHINs added, after subtraction of the SHINs.

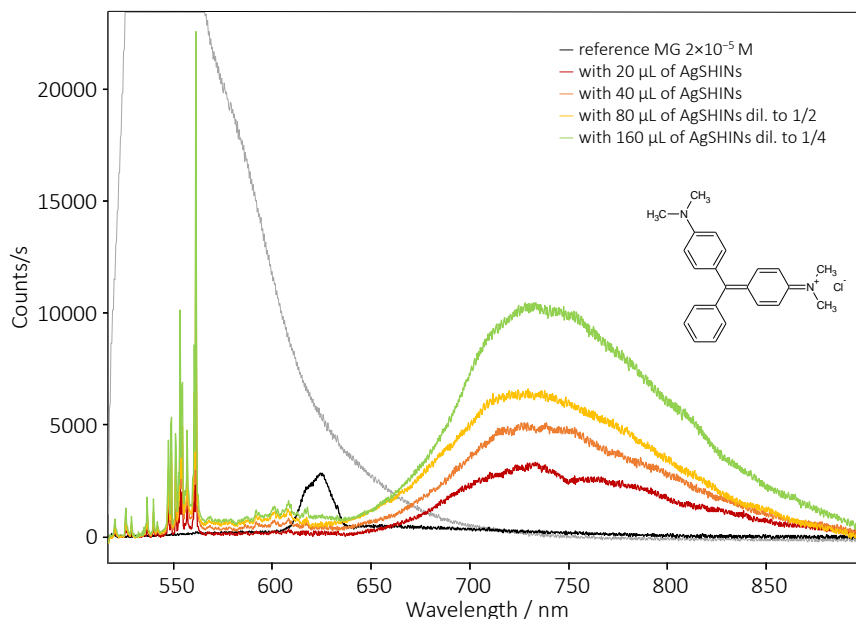


Figure 7.11. Fluorescence spectra of MG 2×10^{-5} M measuring quantum yield. The gray trace is the fluorescence of the standard Eosin Y.

μL added	SHINEF EF	QY	QY EF
0 (ref CV)	-	7.25×10^{-5}	-
20	7.10	5.06×10^{-4}	6.98
40	11.2	8.43×10^{-4}	11.6
80	14.8	1.07×10^{-3}	14.7
160	24.6	1.78×10^{-3}	24.6

Table 7.6. MG SEF EF, quantum yields and QY EFs with increasing amounts of SHINs added.

The calculated quantum yield for MG of 7.25×10^{-5} is also quite close to that reported previously of 7.9×10^{-5} .^[61] There was no change in the area under the curve for the dye extinction in the first points before 80 μL . To summarize, here we find no evidence of enhanced absorption.

7.3.5. High Quantum Yield Dyes

We tried a set of experiments in solution using dyes with higher intrinsic quantum yields, in this case Pyronin Y and Sulforhodamine B. For the former we calculated a quantum yield of 0.32 (somewhat below the literature value of 0.47^[62]) and for the latter 0.23 (reference literature value is 0.27^[63]). We did not observe SHINEF of the dyes, as shown in Figure 7.12 and Figure 7.13.

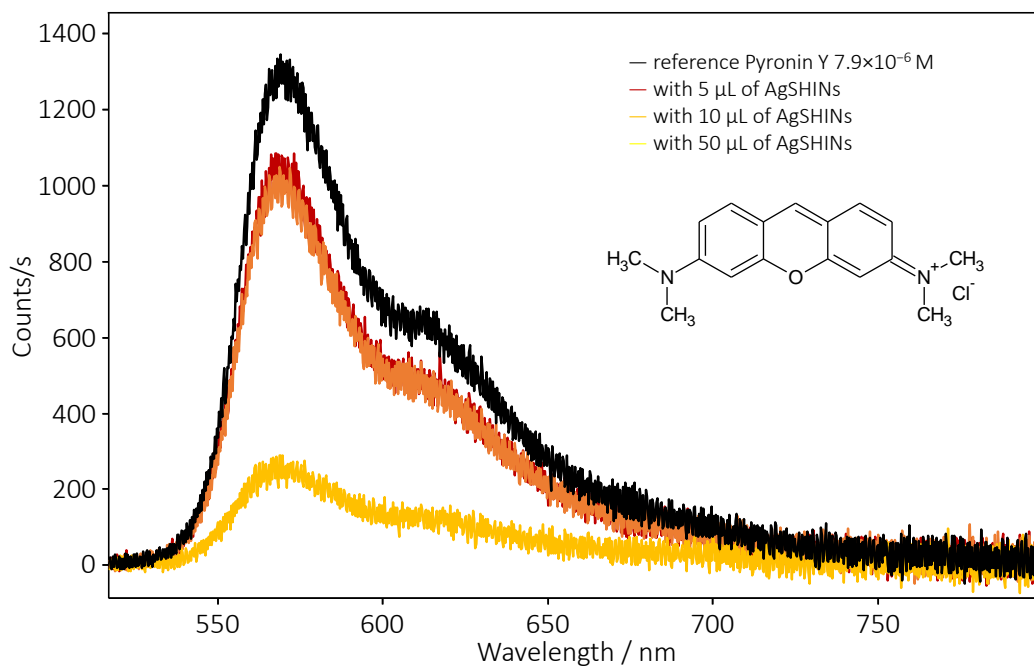


Figure 7.12. Fluorescence of Pyronin Y with increasing SHINs added.
 No enhancement was observed, only quenching.

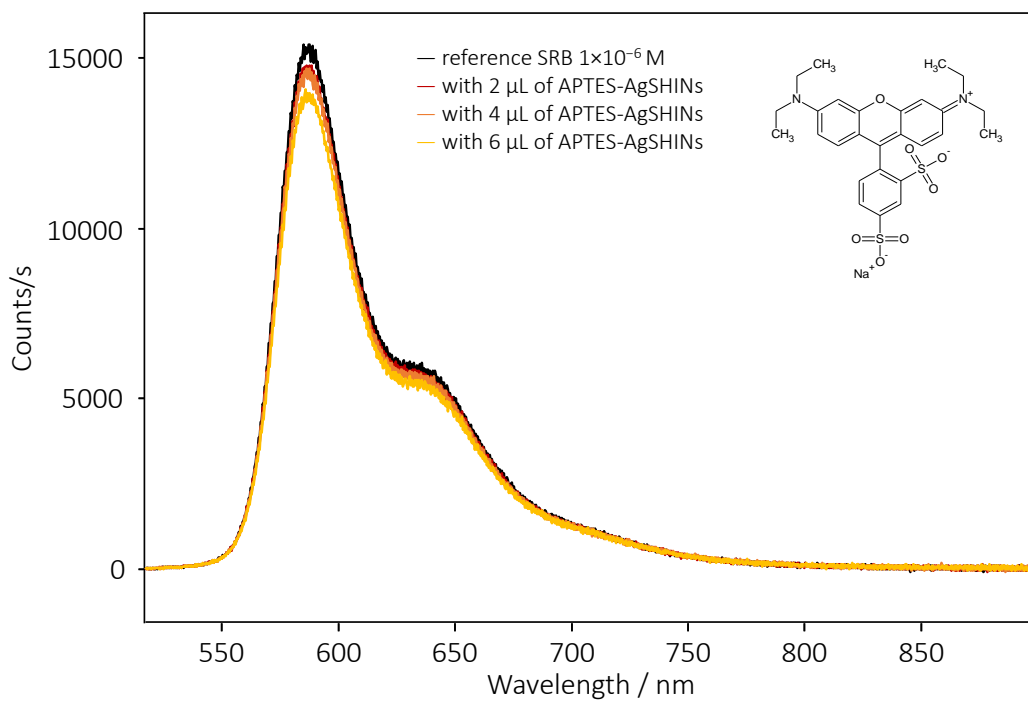


Figure 7.13. Fluorescence of Sulforhodamine B with increasing APTES-Ag SHINs added.
 Again, no enhancement was observed, only quenching.

7.3.6. Enhancement by Nanoparticle Aggregates

It is well known that it is possible to induce partial aggregation in a colloidal dispersion by adding electrolytes like NaCl, and these aggregates provide the hot spots that are associated with the large enhancement factors in SERS. Indeed this is how Kneipp in 1997 obtained single-molecule detection.^[64] As we mentioned, recently, Furtaw and collaborators^[65] have demonstrated SEF in the near infrared using nanoparticle aggregates in solution. This is the first time, however, that we attempt this with our SHIN particles to obtain SEF. The results are shown in Figures 7.14 and 7.15, and Table 7.7.

The spectra clearly show the presence of partial aggregation of the SHINs, seen in the increase of absorption in the region between 650 and 800 nm, and the decrease of the peak at 424 for the non-aggregated SHINs.

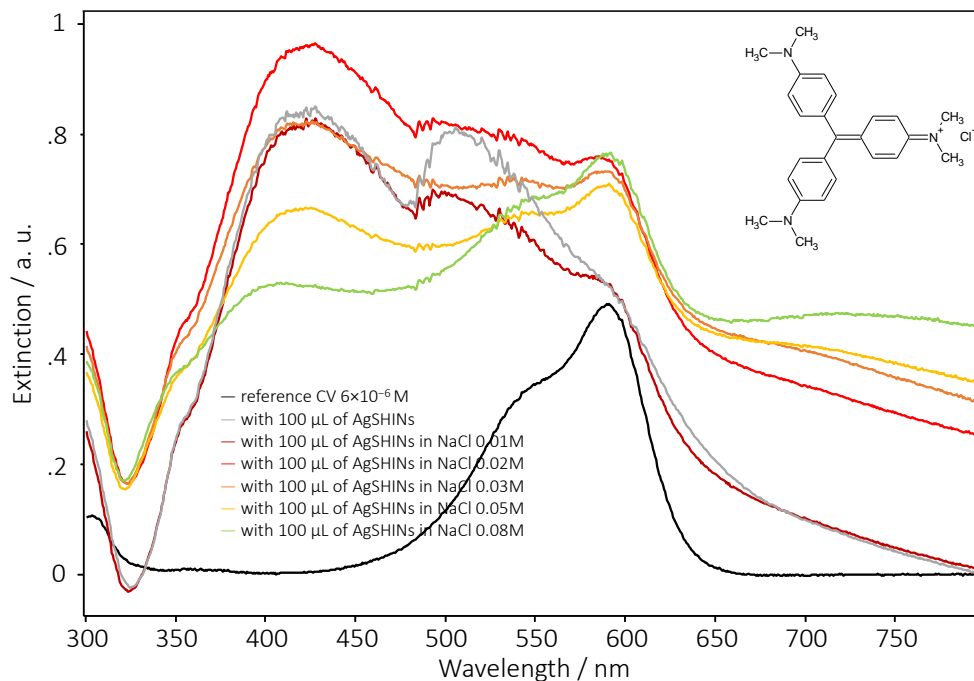


Figure 7.14. Extinction spectra for CV with 100 μL of SHINs and increasing concentrations of NaCl

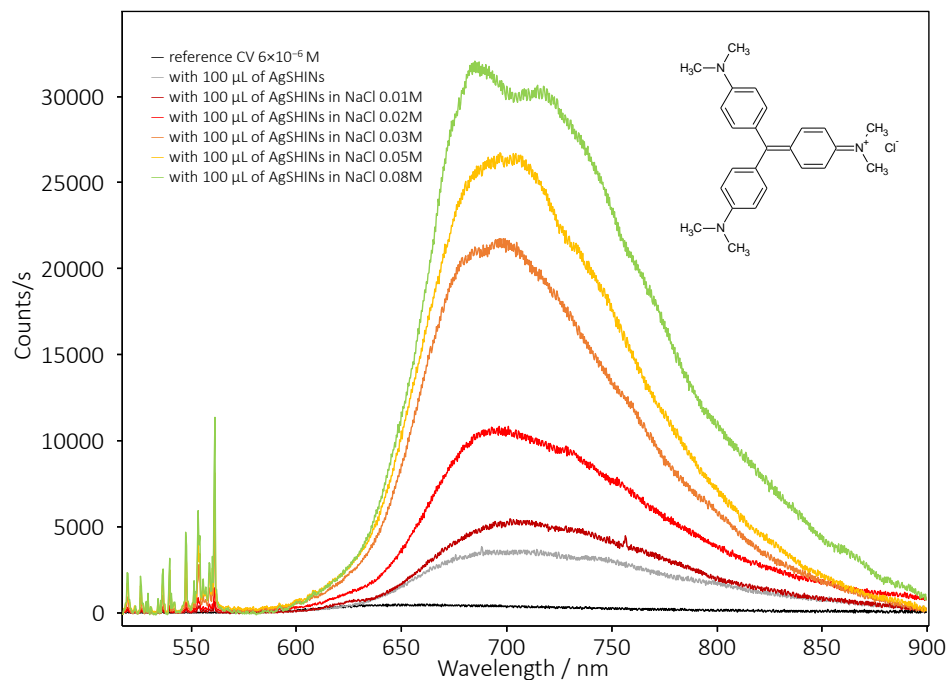


Figure 7.15. Fluorescence spectra for CV with 100 μL of SHINs and increasing concentrations of NaCl.

NaCl conc. / M	EF
0 (only SHINs)	7.09
0.01	9.51
0.02	19.0
0.03	34.6
0.05	43.0
0.08	55.9

Table 7.7. Enhancement factors for CV with 100 μL of SHINs and increasing concentrations of NaCl

The maximum enhancement factor obtained for CV of almost 56 is a clear evidence that particle aggregates giving rise to hot spots give much more enhancement than individual particles, which was the case in all SERS experiments using silver or gold colloids. NaCl 0.08 M was the concentration at which we observed the highest enhancement factor. Beyond this (0.1 M and above) we observed a decrease in the enhancement (data not shown).

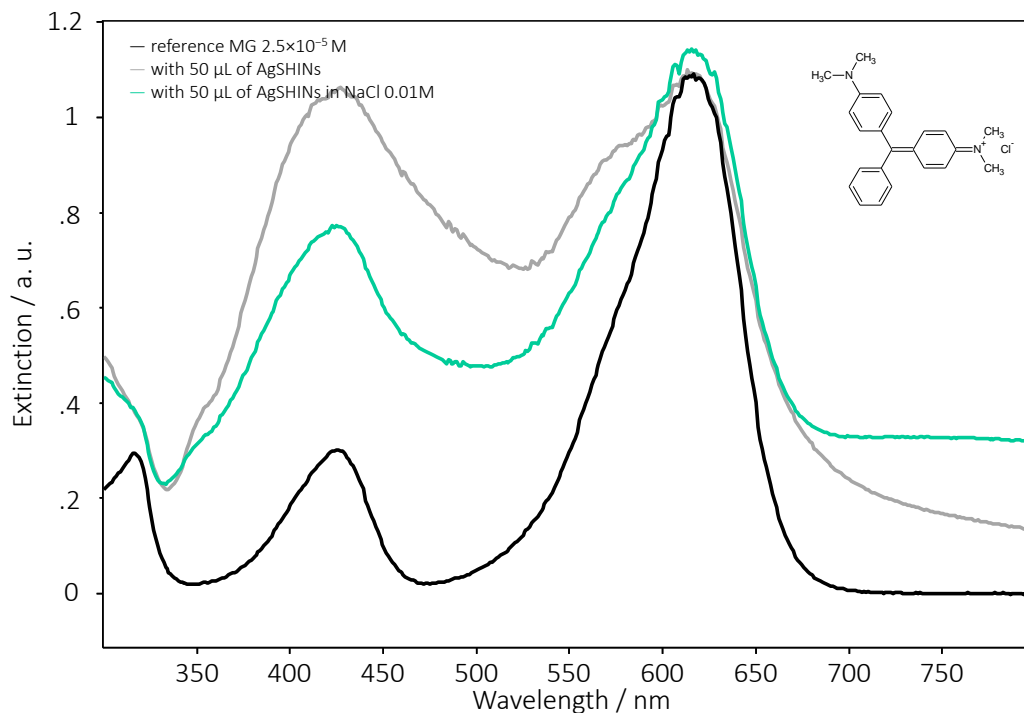


Figure 7.16. Extinction spectra for MG with 50 μL of SHINs and NaCl 0.01 M

For completeness, we also attempted this experiment with MG. With the 514.5 nm laser line, we obtained even more enhancement. We performed the experiment in a different order, though. In the case of the CV, we added first the dye, then the SHINs, then the NaCl, then completing with water up to 1 mL, yielding the result shown above. When performing that strategy with MG, no SEF enhancement was obtained; indeed the fluorescence was quenched (data not shown). However, if one aggregates the colloid first, by adding the SHINs first, then the NaCl to aggregate them, and only then the MG dye, and finally the water, then the SHINEF was augmented as expected. We obtained the maximum EF at a concentration of 0.01M of NaCl, as shown in Figure 7.17. Again, the absorption spectrum shows clearly the presence of SHIN aggregates in the 650-800 nm region.

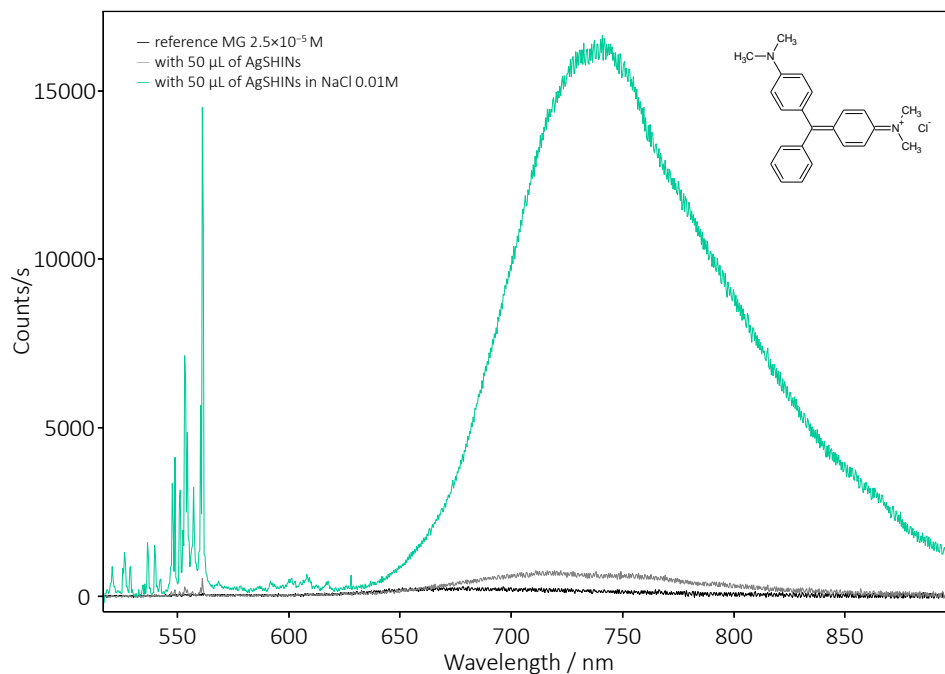


Figure 7.17. Fluorescence spectra for MG with 50 μL of SHINs and NaCl 0.01 M, with the 514.5 nm laser line. The maximum enhancement factor recorded for MG was 66.5, with 0.01 M of NaCl.

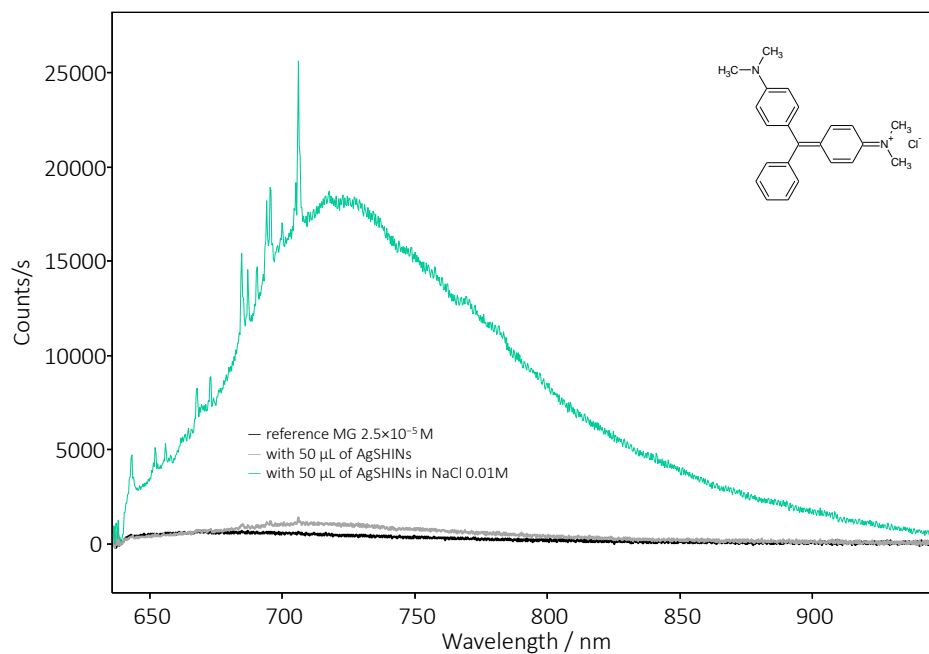


Figure 7.18. Fluorescence spectra for MG with 50 μL of SHINs and NaCl 0.01 M, with the 632.8 nm laser line. The maximum enhancement factor recorded for MG was 25.3, with 0.01 M of NaCl.

The enhancement factors obtained here are the highest we have ever recorded in aqueous solution, being much higher than those without NaCl. Indeed the EF values obtained in this way are now comparable to those we have previously obtained in our group for mixed LB films using Ag SHINs.^[41,66-68] Clearly this enhancement is due to the presence of hot spots in the SHIN aggregates.

7.4. Conclusions

Perhaps the most important piece of evidence presented here is the role of SHIN's aggregation, which is necessary to achieve larger enhancements. These results open the door for further investigation of aggregation in solution using inorganic salts (also organics or surfactants) to tune SHINEF applications in solution. The second interesting result is the lack of a direct correlation between the power of the incident radiation and the observed SHINEF intensity, casting doubt on the suggestion that SEF is simply due to enhanced excitation of the molecule by the nanoparticle.

The question of high quantum yield versus low quantum yield is still open. The results presented here, in solution, with a limited number of high QY molecules is in favor of the low QY molecules. Indeed, there are many reports of SEF and SHINEF using high quantum yield dyes, especially our own studies presented in Chapters 4^[51,52] and 5.^[49] However, we have to remember that all of those studies were performed in solid state, with the nanostructures and the excited molecules forming thin layers. The solid state has little mobility, while in solution the molecules are moving constantly in Brownian motion. Future work in this area, including hot spots, will help to clarify the regimes of solid and liquid and the role of different contributing factors.

7.5. References

1. Glass, A. M.; Liao, P. F.; Bergman, J. G.; Olson, D. H. *Opt. Lett.* **1980**, *5*, 368.
2. Douketis, C.; Haslett, T. L.; Wang, Z.; Moskovits, M.; Iannotta, S. *J. Chem. Phys.* **2000**, *113*, 11315.

3. Chance, R. R.; Prock, A.; Silbey, R. In *Advances in Chemical Physics*; John Wiley & Sons, Inc.: 1978, p 1.
4. Drexhage, K. H. *J. Lumin.* **1970**, 1–2, 693.
5. Willets, K. A.; Van Duyne, R. P. *Annu. Rev. Phys. Chem.* **2007**, 58, 267.
6. Ahmed, S. R.; Cha, H. R.; Park, J. Y.; Park, E. Y.; Lee, D.; Lee, J. *Nanoscale Res. Lett.* **2012**, 7.
7. Akbay, N.; Lakowicz, J. R.; Ray, K. *J. Phys. Chem. C* **2012**, 116, 10766.
8. Capehart, S. L.; Coyle, M. P.; Glasgow, J. E.; Francis, M. B. *J. Am. Chem. Soc.* **2013**, 135, 3011.
9. Elmalk, A. T.; Salverda, J. M.; Tabares, L. C.; Canters, G. W.; Aartsma, T. J. *J. Chem. Phys.* **2012**, 136.
10. Ganguly, M.; Pal, A.; Negishi, Y.; Pal, T. *Langmuir* **2013**, 29, 2033.
11. Gartia, M. R.; Eichorst, J. P.; Clegg, R. M.; Liu, G. L. *Appl. Phys. Lett.* **2012**, 101.
12. Gill, R.; Tian, L. J.; Somerville, W. R. C.; Le Ru, E. C.; van Amerongen, H.; Subramaniam, V. *J. Phys. Chem. C* **2012**, 116, 16687.
13. Guo, P.; Xu, J.; Zhuang, X.; Hu, W.; Zhu, X.; Zhou, H.; Tang, L.; Pan, A. *J. Mater. Chem.* **2013**, 1, 566.
14. Huang, Y. F.; Ma, K. H.; Kang, K. B.; Zhao, M.; Zhang, Z. L.; Liu, Y. X.; Wen, T.; Wang, Q.; Qiu, W. Y.; Qiu, D. *Colloid Surf. A-Physicochem. Eng. Asp.* **2013**, 421, 101.
15. Hui, Y. Y.; Lu, Y.-C.; Su, L.-J.; Fang, C.-Y.; Hsu, J.-H.; Chang, H.-C. *Appl. Phys. Lett.* **2013**, 102, 013102.
16. Karolin, J. O.; Geddes, C. D. *J. Fluoresc.* **2012**, 22, 1659.
17. Kaur, G.; Verma, R. K.; Rai, D. K.; Rai, S. B. *J. Lumin.* **2012**, 132, 1683.
18. Kowalska, D.; Krajnik, B.; Olejnik, M.; Twardowska, M.; Czechowski, N.; Hofmann, E.; Mackowski, S. *ScientificWorldJournal* **2013**, 2013, 12.
19. Lee, Y. B.; Lee, S. H.; Lee, S.; Lee, H.; Kim, J.; Joo, J. *Appl. Phys. Lett.* **2013**, 102.
20. Li, R. Q.; Wang, C. L.; Xu, S. H.; Wang, Z. Y.; Shao, H. B.; Cui, Y. P. *Chin. J. Chem.* **2012**, 30, 1490.

21. Masuo, S.; Tanaka, T.; Machida, S.; Itaya, A. *J. Photochem. Photobiol. A-Chem.* **2012**, *237*, 24.
22. Petryayeva, E.; Algar, W. R.; Medintz, I. L. *Appl. Spectrosc.* **2013**, *67*, 215.
23. Rich, R.; Li, J.; Fudala, R.; Gryczynski, Z.; Gryczynski, I.; Mandecki, W. *Anal. Bioanal. Chem.* **2012**, *404*, 2223.
24. Shen, J.; Li, Z. Q.; Chen, Y. R.; Chen, X. H.; Chen, Y. W.; Sun, Z.; Huang, S. M. *Appl. Surf. Sci.* **2013**, *270*, 712.
25. Sreenivasan, V. K. A.; Zvyagin, A. V.; Goldys, E. M. *J. Phys.-Condes. Matter* **2013**, *25*.
26. Szlajak, R.; Tutaj, K.; Grudzinski, W.; Gruszecki, W.; Luchowski, R. *J. Nanopart. Res.* **2013**, *15*, 1.
27. Tang, L. J.; Xu, J. Y.; Guo, P. F.; Zhuang, X. J.; Tian, Y.; Wang, Y. C.; Duan, H. G.; Pan, A. *L. Opt. Express* **2013**, *21*, 11095.
28. Teng, Y.; Ueno, K.; Shi, X.; Aoyo, D.; Qiu, J. R.; Misawa, H. *Ann. Phys.-Leipzig* **2012**, *524*, 733.
29. Tombe, S.; Antunes, E.; Nyokong, T. *J. Mol. Catal. A: Chem.* **2013**, *371*, 125.
30. Tsung Chen, I.; Chang, P.-H.; Chang, Y.-C.; Guo, T.-F. *Sci. Rep.* **2013**, *3*.
31. Wang, Y.; Li, S. S.; Yeh, Y. C.; Yu, C. C.; Chen, H. L.; Li, F. C.; Chang, Y. M.; Chen, C. W. *Nanoscale* **2013**, *5*, 1687.
32. Zhang, D. K.; Hu, X. Y.; Ji, R. N.; Zhan, S. C.; Gao, J. H.; Yan, Z. Y.; Liu, E. Z.; Fan, J.; Hou, X. *J. Non-Cryst. Solids* **2012**, *358*, 2788.
33. Zhang, J.; Fu, Y.; Li, G.; Zhao, R. Y. *Biochem. Biophys. Res. Commun.* **2012**, *425*, 696.
34. Zhang, J.; Fu, Y.; Mandavi, F. *J. Phys. Chem. C* **2012**, *116*, 24224.
35. Zhang, J.; Fu, Y.; Ray, K.; Wang, Y.; Lakowicz, J. R. *J. Phys. Chem. C* **2013**, *117*, 9372.
36. Zhang, Z. L.; Zheng, H. R.; Dong, J.; Yan, X. Q.; Sun, Y.; Xu, H. X. *Sci. China-Phys. Mech. Astron.* **2012**, *55*, 767.
37. Zheng, S.; Zhou, Y.; Yin, D.; Xu, X.; Qi, Y.; Peng, S. *J. Alloys Compd.* **2013**, *566*, 90.
38. Wokaun, A.; Lutz, H. P.; King, A. P.; Wild, U. P.; Ernst, R. R. *J. Chem. Phys.* **1983**, *79*, 509.
39. Anger, P.; Bharadwaj, P.; Novotny, L. *Phys. Rev. Lett.* **2006**, *96*, 113002.
40. Wokaun, A.; Lutz, H. P.; King, A. P. *Springer Ser. Chem. Phys.* **1983**, *33*, 86.

41. Guerrero, A. R.; Zhang, Y.; Aroca, R. F. *Small* **2012**, *8*, 2964.
42. Bardhan, R.; Grady, N. K.; Halas, N. J. *Small* **2008**, *4*, 1716.
43. Schaadt, D. M.; Feng, B.; Yu, E. T. *Appl. Phys. Lett.* **2005**, *86*, 063106.
44. Cang, H.; Labno, A.; Lu, C. G.; Yin, X. B.; Liu, M.; Gladden, C.; Liu, Y. M.; Zhang, X. *Nature* **2011**, *469*, 385.
45. Gill, R.; Le Ru, E. C. *Phys. Chem. Chem. Phys.* **2011**, *13*, 16366.
46. Kinkhabwala, A.; Yu, Z.; Fan, S.; Avlasevich, Y.; Müllen, K.; Moerner, W. E. *Nat. Photonics* **2009**, *3*, 654.
47. Zhang, W.; Ding, F.; Li, W.-D.; Wang, Y.; Hu, J.; Chou, S. Y. *Nanotechnology* **2012**, *23*, 225301.
48. Le Ru, E. C.; Etchegoin, P. G.; Grand, J.; Félidj, N.; Aubard, J.; Lévi, G. *J. Phys. Chem. C* **2007**, *111*, 16076.
49. Aroca, R. F.; Teo, G. Y.; Mohan, H.; Guerrero, A. R.; Albella, P.; Moreno, F. *J. Phys. Chem. C* **2011**, *115*, 20419.
50. Tam, F.; Goodrich, G. P.; Johnson, B. R.; Halas, N. J. *Nano Lett.* **2007**, *7*, 496.
51. Guerrero, A. R.; Aroca, R. F. *Angew. Chem. Ger. Edit.* **2011**, *123*, 691.
52. Guerrero, A. R.; Aroca, R. F. *Angew. Chem. Int. Ed.* **2011**, *50*, 665.
53. Lee, P. C.; Meisel, D. *J. Phys. Chem.* **1982**, *86*, 3391.
54. Brouwer, A. M. *Pure Appl. Chem.* **2011**, *83*, 2213.
55. Parker, C. A.; Rees, W. T. *Analyst* **1960**, *85*, 587.
56. Weber, G.; Teale, F. W. J. *Trans. Faraday Soc.* **1957**, *53*, 646.
57. Sarojini, P.; Gouranga Chandra, M.; Gourisankar, R.; Kiranmayee, S. *Lat. Am. J. Phys. Educ.* **2011**, *5*, 734.
58. Baptista, M. S.; Indig, G. L. *J. Phys. Chem. B* **1998**, *102*, 4678.
59. Galloway, C. M.; Etchegoin, P. G.; Le Ru, E. C. *Phys. Rev. Lett.* **2009**, *103*.
60. Meyer, S. A.; Le Ru, E. C.; Etchegoin, P. G. *J. Phys. Chem. A* **2010**, *114*, 5515.
61. Babendure, J. R.; Adams, S. R.; Tsien, R. Y. *J. Am. Chem. Soc.* **2003**, *125*, 14716.
62. Reija, B.; Al-Soufi, W.; Novo, M.; Vázquez Tato, J. *J. Phys. Chem. B* **2005**, *109*, 1364.
63. Mohanty, J.; Jagtap, K.; Ray, A. K.; Nau, W. M.; Pal, H. *ChemPhysChem* **2010**, *11*, 3333.

64. Kneipp, K.; Wang, Y.; Kneipp, H.; Perelman, L. T.; Itzkan, I.; Dasari, R. R.; Feld, M. S. *Phys. Rev. Lett.* **1997**, *78*, 1667.
65. Furtaw, M. D.; Anderson, J. P.; Middendorf, L. R.; Bashford, G. R. *Plasmonics* **2013**, *1*.
66. Mohan, H. Plasmon Enhanced Fluorescence (PEF) of High and Low Quantum Yield Molecules. M.Sc. Thesis, University of Windsor, Windsor, Ontario, 2013.
67. Al-Saleh, A. A. SERS/SERRS probes and SERS substrates in Langmuir monolayers. M.Sc. Thesis, University of Windsor, Windsor, Ontario, 2013.
68. Zhang, Y. Synthesis of Metallic Nanostructures for Applications in Ultrasensitive Detection. M.Sc. Thesis, University of Windsor, Windsor, Ontario, 2013.

Chapter Eight

Concluding Remarks

We have come a long way exploring plasmon-enhanced spectroscopy, crossing the paths of SERS and SEF through naked and shelled, gold and silver nanoparticles. In Chapter 3^[1] we reported SERS of hydroxyproline, after overcoming many difficulties related to the reproducibility of the SERS spectra of amino acids. In order to do this, we employed gold colloidal nanoparticles, without stabilizing agent, in order to improve the adsorption of the amino acid. The result was a protocol that allowed us to obtain SERS spectra of hydroxyproline with negligible variations in different trials. We were able to provide the full characterization for an amino acid not previously described in the literature. Indeed the next report on hydroxyproline was only published one month after the publication of ours (Cárcamo *et al.*^[2]).

The research developed in Chapters 4 to 7 has yielded a whole new avenue of research, which we have called SHINEF. First we provided the proof of concept for their use, using the signature technique of our lab, plasmon-enhanced spectroscopy on Langmuir-Blodgett films.^[3,4] Later we investigated the plasmonic properties of SHINEF, studying the effects of the core size, shell size and shape.^[5] The exploration of SHINEF in aqueous solution, and using silver nanoparticles instead of gold has provided with the experimental confirmation of the long hypothesized E^2/E^4 relationship, as well as yielding enhancement factors much larger than those obtained from gold nanoparticles.^[6] Finally, we have explored several different factors that play a role in the origin of SEF, showing greater enhancement for SHINEF after inducing nanoparticle aggregation. As we discussed at the end of Chapter 7, the results of SHINEF in aqueous solution and in solid state for high and low quantum yield molecules are not in agreement, and further work in the subject is necessary.

The versatility of the SHINEF and SHINERS techniques is not trivial, and will be harnessed in future work for many potential applications.^[7] The great enhancement of the fluorescence signal provided by the technique should allow for applications in many fields: everyone who needs enhanced sensitivity in fluorescence and Raman should be able to take advantage of SHINEF and SHINERS. We look forward especially to applications in biomedical science. Fluorescent probes are routinely used for biological analyses; one could imagine multiple scenarios where SHINs could be used to enhance the sensitivity ranges of the fluorescence assays. *In vitro* and *ex vivo* analyses are always a possibility for the direct application of SHINEF; however, toxicity tests of the SHIN particles would need to be performed in order to assess for possible direct *in vivo* use.

Another pending issue that needs to be solved towards the application of SHINEF is the effective delivery of SHINs to a substrate producing a homogeneous, reproducible coverage. Our work in dry substrates was performed all by casting droplets of our SHIN colloidal dispersions on glass, but this provides a coverage that is quite imperfect. Haider Mohan's thesis paved the way through the spraying of concentrated SHIN solutions,^[8] and further research is already being carried out in our group towards a better implementation of that idea.

The ultimate possibilities of SHINEF are yet to be explored. We look forward to a brighter future where plasmonics will have a positive, much larger impact in our everyday lives.

References

1. Guerrero, A. R.; Aroca, R. F. *J. Raman Spectrosc.* **2012**, *43*, 478.
2. Cárcamo, J. J.; Aliaga, A. E.; Clavijo, E.; Garrido, C.; Gómez-Jeria, J. S.; Campos-Vallette, M. M. *J. Raman Spectrosc.* **2012**, *43*, 750.
3. Guerrero, A. R.; Aroca, R. F. *Angew. Chem. Ger. Edit.* **2011**, *123*, 691.
4. Guerrero, A. R.; Aroca, R. F. *Angew. Chem. Int. Ed.* **2011**, *50*, 665.

5. Aroca, R. F.; Teo, G. Y.; Mohan, H.; Guerrero, A. R.; Albella, P.; Moreno, F. J. *Phys. Chem. C* **2011**, *115*, 20419.
6. Guerrero, A. R.; Zhang, Y.; Aroca, R. F. *Small* **2012**, *8*, 2964.
7. Moskovits, M. *Nature* **2010**, *464*, 357.
8. Mohan, H. Plasmon Enhanced Fluorescence (PEF) of High and Low Quantum Yield Molecules. M.Sc. Thesis, University of Windsor, Windsor, Ontario, 2013.

Permissions Obtained for Published Copyrighted Materials

1. Surface-Enhanced Raman Scattering of Hydroxyproline (Chapter 3)

JOHN WILEY AND SONS LICENSE

Jan 10, 2013

This is a License Agreement between Ariel R Guerrero ("You") and John Wiley and Sons ("John Wiley and Sons") provided by Copyright Clearance Center ("CCC"). The license consists of your order details, the terms and conditions provided by John Wiley and Sons, and the payment terms and conditions.

All payments must be made in full to CCC. For payment instructions, please see information listed at the bottom of this form.

License Number	3065380991265
License date	Jan 10, 2013
Licensed content publisher	John Wiley and Sons
Licensed content publication	Journal of Raman Spectroscopy
Paper title	Surface-Enhanced Raman Scattering of Hydroxyproline
Licensed content author	Ariel R. Guerrero, Ricardo F. Aroca
Licensed content date	Oct 27, 2011
Start page	478
End page	481
Type of use	Dissertation/Thesis
Requestor type	Author of this Wiley article
Format	Print and electronic
Portion	Full article
Will you be translating?	No
Order reference number	

Total

0.00 USD

TERMS AND CONDITIONS

(These terms and conditions are the same for all three papers published in Wiley journals, that is, Journal of Raman Spectroscopy (SERS of Hydroxyproline, Chapter 3), Angewandte Chemie International Edition (SHINEF, Chapter 4) and Small (Experimental confirmation of near-field... Chapter 6) and will be reproduced here only once.)

This copyrighted material is owned by or exclusively licensed to John Wiley & Sons, Inc. or one of its group companies (each a "Wiley Company") or a society for whom a Wiley Company has exclusive publishing rights in relation to a particular journal (collectively WILEY"). By clicking "accept" in connection with completing this licensing transaction, you agree that the following terms and conditions apply to this transaction (along with the billing and payment terms and conditions established by the Copyright Clearance Center Inc., ("CCC's Billing and Payment terms and conditions"), at the time that you opened your Rightslink account (these are available at any time at <http://myaccount.copyright.com>)

Terms and Conditions

1. The materials you have requested permission to reproduce (the "Materials") are protected by copyright.
2. You are hereby granted a personal, non-exclusive, non-sublicensable, non-transferable, worldwide, limited license to reproduce the Materials for the purpose specified in the licensing process. This license is for a one-time use only with a maximum distribution equal to the number that you identified in the licensing process. Any form of republication granted by this licence must be completed within two years of the date of the grant of this licence (although copies prepared before may be distributed thereafter). The Materials shall not be used in any other manner or for any other purpose. Permission is granted subject to an appropriate acknowledgement given to the author, title of the material/book/journal and the publisher. You shall also duplicate the copyright notice that appears in the Wiley publication in your use of the Material. Permission is also granted on the understanding that nowhere in the text is a previously published source acknowledged for all or part of this Material. Any third party material is expressly excluded from this permission.
3. With respect to the Materials, all rights are reserved. Except as expressly granted by the terms of the license, no part of the Materials may be copied, modified, adapted (except for minor reformatting required by the new Publication), translated, reproduced, transferred or distributed, in any form or by any means, and no derivative works may be made based on the Materials without the prior permission of the respective copyright owner. You may not alter, remove or suppress in any manner any copyright, trademark or other notices displayed by the Materials. You may not license, rent, sell, loan, lease, pledge, offer as security, transfer or assign the Materials, or any of the rights granted to you hereunder to any other person.
4. The Materials and all of the intellectual property rights therein shall at all times remain the exclusive property of John Wiley & Sons Inc or one of its related companies (WILEY) or their respective licensors, and your interest therein is only that of having possession of and the right to reproduce the Materials pursuant to Section 2 herein during the continuance of this Agreement. You agree that you own no right, title or interest in or to the Materials or any of the intellectual property rights therein. You shall have no rights hereunder other than the license as provided for above in Section 2. No right, license or interest to any trademark, trade name, service mark or other branding ("Marks") of WILEY or its licensors is granted hereunder, and you agree that you shall not assert any such right, license or interest with respect thereto.

5. NEITHER WILEY NOR ITS LICENSORS MAKES ANY WARRANTY OR REPRESENTATION OF ANY KIND TO YOU OR ANY THIRD PARTY, EXPRESS, IMPLIED OR STATUTORY, WITH RESPECT TO THE MATERIALS OR THE ACCURACY OF ANY INFORMATION CONTAINED IN THE MATERIALS, INCLUDING, WITHOUT LIMITATION, ANY IMPLIED WARRANTY OF MERCHANTABILITY, ACCURACY, SATISFACTORY QUALITY, FITNESS FOR A PARTICULAR PURPOSE, USABILITY, INTEGRATION OR NON-INFRINGEMENT AND ALL SUCH WARRANTIES ARE HEREBY EXCLUDED BY WILEY AND ITS LICENSORS AND WAIVED BY YOU.

6. WILEY shall have the right to terminate this Agreement immediately upon breach of this Agreement by you.

7. You shall indemnify, defend and hold harmless WILEY, its Licensors and their respective directors, officers, agents and employees, from and against any actual or threatened claims, demands, causes of action or proceedings arising from any breach of this Agreement by you.

8. IN NO EVENT SHALL WILEY OR ITS LICENSORS BE LIABLE TO YOU OR ANY OTHER PARTY OR ANY OTHER PERSON OR ENTITY FOR ANY SPECIAL, CONSEQUENTIAL, INCIDENTAL, INDIRECT, EXEMPLARY OR PUNITIVE DAMAGES, HOWEVER CAUSED, ARISING OUT OF OR IN CONNECTION WITH THE DOWNLOADING, PROVISIONING, VIEWING OR USE OF THE MATERIALS REGARDLESS OF THE FORM OF ACTION, WHETHER FOR BREACH OF CONTRACT, BREACH OF WARRANTY, TORT, NEGLIGENCE, INFRINGEMENT OR OTHERWISE (INCLUDING, WITHOUT LIMITATION, DAMAGES BASED ON LOSS OF PROFITS, DATA, FILES, USE, BUSINESS OPPORTUNITY OR CLAIMS OF THIRD PARTIES), AND WHETHER OR NOT THE PARTY HAS BEEN ADVISED OF THE POSSIBILITY OF SUCH DAMAGES. THIS LIMITATION SHALL APPLY NOTWITHSTANDING ANY FAILURE OF ESSENTIAL PURPOSE OF ANY LIMITED REMEDY PROVIDED HEREIN.

9. Should any provision of this Agreement be held by a court of competent jurisdiction to be illegal, invalid, or unenforceable, that provision shall be deemed amended to achieve as nearly as possible the same economic effect as the original provision, and the legality, validity and enforceability of the remaining provisions of this Agreement shall not be affected or impaired thereby.

10. The failure of either party to enforce any term or condition of this Agreement shall not constitute a waiver of either party's right to enforce each and every term and condition of this Agreement. No breach under this agreement shall be deemed waived or excused by either party unless such waiver or consent is in writing signed by the party granting such waiver or consent. The waiver by or consent of a party to a breach of any provision of this Agreement shall not operate or be construed as a waiver of or consent to any other or subsequent breach by such other party.

11. This Agreement may not be assigned (including by operation of law or otherwise) by you without WILEY's prior written consent.

12. Any fee required for this permission shall be non-refundable after thirty (30) days from receipt.

13. These terms and conditions together with CCC's Billing and Payment terms and conditions (which are incorporated herein) form the entire agreement between you and WILEY concerning this licensing transaction and (in the absence of fraud) supersedes all prior agreements and representations of the parties, oral or written. This Agreement may not be amended except in writing signed by both parties. This Agreement shall be binding upon and inure to the benefit of the parties' successors, legal representatives, and authorized assigns.

14. In the event of any conflict between your obligations established by these terms and conditions and those established by CCC's Billing and Payment terms and conditions, these terms and conditions shall prevail.

15. WILEY expressly reserves all rights not specifically granted in the combination of (i) the license details provided by you and accepted in the course of this licensing transaction, (ii) these terms and conditions and (iii) CCC's Billing and Payment terms and conditions.

16. This Agreement will be void if the Type of Use, Format, Circulation, or Requestor Type was misrepresented during the licensing process.

17. This Agreement shall be governed by and construed in accordance with the laws of the State of New York, USA, without regards to such state's conflict of law rules. Any legal action, suit or proceeding arising out of or relating to these Terms and Conditions or the breach thereof shall be instituted in a court of competent jurisdiction in New York County in the State of New York in the United States of America and each party hereby consents and submits to the personal jurisdiction of such court, waives any objection to venue in such court and consents to service of process by registered or certified mail, return receipt requested, at the last known address of such party.

2. Surface-Enhanced Fluorescence with Shell-Isolated Nanoparticles (Chapter 4)

JOHN WILEY AND SONS LICENSE

Jan 10, 2013

This is a License Agreement between Ariel R Guerrero ("You") and John Wiley and Sons ("John Wiley and Sons") provided by Copyright Clearance Center ("CCC"). The license consists of your order details, the terms and conditions provided by John Wiley and Sons, and the payment terms and conditions.

All payments must be made in full to CCC. For payment instructions, please see information listed at the bottom of this form.

License Number	3065390495964
License date	Jan 10, 2013
Licensed content publisher	John Wiley and Sons
Licensed content publication	Angewandte Chemie International Edition
Paper title	Surface Enhanced Fluorescence with Shell-Isolated Nanoparticles (SHINEF)
Licensed content author	Ariel R. Guerrero, Ricardo F. Aroca

Licensed content date	Dec 15, 2010
Start page	665
End page	668
Type of use	Dissertation/Thesis
Requestor type	Author of this Wiley article
Format	Print and electronic
Portion	Full article
Will you be translating?	No
Order reference number	
Total	0.00 USD

3. Plasmon-Enhanced Fluorescence and Spectral Modification in SHINEF (Chapter 5)

COPYRIGHT CLEARANCE CENTER – RIGHTSLINK®

Title: Plasmon-Enhanced Fluorescence and Spectral Modification in SHINEF
Authors: Ricardo F. Aroca, Geok Yi Teo, Haider Mohan, Ariel R. Guerrero, Pablo Albella, and Fernando Moreno
Publication: The Journal of Physical Chemistry C
Publisher: American Chemical Society
Date: Oct 1, 2011

PERMISSION/LICENSE IS GRANTED FOR YOUR ORDER AT NO CHARGE.

This type of permission/license, instead of the standard Terms & Conditions, is sent to you because no fee is being charged for your order. Please note the following:

- Permission is granted for your request in both print and electronic formats, and translations.
- If figures and/or tables were requested, they may be adapted or used in part.
- Please print this page for your records and send a copy of it to your publisher/graduate school.

- Appropriate credit for the requested material should be given as follows: "Reprinted (adapted) with permission from (COMPLETE REFERENCE CITATION). Copyright (YEAR) American Chemical Society." Insert appropriate information in place of the capitalized words.
- One-time permission is granted only for the use specified in your request. No additional uses are granted (such as derivative works or other editions). For any other uses, please submit a new request.

4. Plasmon Enhanced Raman-Fluorescence Ratio with Shell-Isolated Silver Nanoparticles (Chapter 6)

JOHN WILEY AND SONS LICENSE

Jan 10, 2013

This is a License Agreement between Ariel R Guerrero ("You") and John Wiley and Sons ("John Wiley and Sons") provided by Copyright Clearance Center ("CCC"). The license consists of your order details, the terms and conditions provided by John Wiley and Sons, and the payment terms and conditions.

All payments must be made in full to CCC. For payment instructions, please see information listed at the bottom of this form.

License Number	3065391481203
License date	Jan 10, 2013
Licensed content publisher	John Wiley and Sons
Licensed content publication	Small
Paper title	Experimental Confirmation of Local Field Enhancement Determining Far Field Measurements with Shell-Isolated Silver Nanoparticles
Licensed content author	Ariel R. Guerrero, Yun Zhang, Ricardo F. Aroca
Licensed content date	Jul 6, 2012

Start page	2964
End page	2967
Type of use	Dissertation/Thesis
Requestor type	Author of this Wiley article
Format	Print and electronic
Portion	Full article
Will you be translating?	No
Order reference number	
Total	0.0 USD

Vita Auctoris

Ariel Rodrigo Guerrero Hernández was born in 1983 in Santiago, Chile. He completed his secondary education at the *Instituto Nacional "General José Miguel Carrera"* school in December 2000 in Santiago, Chile, and in March 2001 he entered the program of Chemistry and Pharmacy (*Química y Farmacia*) at the University of Chile (*Universidad de Chile*), in the Faculty of Chemical and Pharmaceutical Sciences (*Facultad de Ciencias Químicas y Farmacéuticas*) where he completed the requirements for his bachelor's degree (*Licenciado en Farmacia, Bachelor of Pharmacy*) in December 2004, completed his coursework in 2006 having ranked first among his generation both at his university and also nationally, as recognized by the Chilean College of Pharmacists, and obtained his professional title of Chemist-Pharmacist (*Químico Farmacéutico*) in August 2008. Later in the same month, he joined the University of Windsor, Ontario, Canada, specifically the Materials and Surface Science Group in the Department of Chemistry and Biochemistry, where he has been performing research under Dr. Ricardo Aroca's supervision since.

As a hobby, Ariel dabbles as a visual artist, specializing in realistic portraiture with dry media. Ariel also sings, plays the guitar and composes music.

List of Publications

Scientific Journal Articles:

1. Peptides and metallic nanoparticles for biomedical applications. Kogan, M. J.; Olmedo, I.; Hosta, L.; **Guerrero, A. R.**; Cruz, L. J.; Albericio, F. *Nanomedicine* **2007**, *2*, 287.
2. Exploring the Surface Charge on Peptide-Gold Nanoparticle Conjugates by Force Spectroscopy. **Guerrero, A. R.**; Caballero, L.; Adeva, A.; Melo, F.; Kogan, M. J. *Langmuir* **2010**, *26*, 12026.
3. Surface-Enhanced Fluorescence with Shell-Isolated Nanoparticles (SHINEF). **Guerrero, A. R.**; Aroca, R. F. *Angew. Chem. Int. Ed.* **2011**, *50*, 665.

Also published in the German edition: *Angew. Chem. Ger. Edit.* **2011**, *123*, 691.

4. Plasmon-Enhanced Fluorescence and Spectral Modification in SHINEF. Aroca, R. F.; Teo, G. Y.; Mohan, H.; **Guerrero, A. R.**; Albella, P.; Moreno, F. J. *Phys. Chem. C* **2011**, *115*, 20419.
5. Surface-Enhanced Raman Scattering of Hydroxyproline. **Guerrero, A. R.**; Aroca, R. F. *J. Raman Spectrosc.* **2012**, *43*, 478.
6. Experimental Confirmation of Local Field Enhancement Determining Far Field Measurements with Shell-Isolated Silver Nanoparticles. **Guerrero, A. R.**; Zhang, Y.; Aroca, R. F. *Small* **2012**, *8*, 2964.

Book Chapter:

- The Power of Functional Resins in Organic Synthesis. Tulla-Puche, J. and Albericio, F., editors. John Wiley & Sons Inc., 2008. Chapter 3: Nanoparticles Functionalized with Bioactive Molecules: Biomedical Applications. Olmedo, I. **Guerrero, A.R.**; Araya, E. and Kogan, M.J.

International Conference Presentations:

1. Surface-Enhanced Raman Scattering of Hydroxyproline in Gold Colloids. **Guerrero, A. R.**; Aroca, R. F. XXII International Conference on Raman Spectroscopy, 2010, Boston (MA), United States. Poster presentation.
Included in: *Proceedings of the XXII International Conference on Raman Spectroscopy*; Champion, P. M., Ziegler, L. D., Eds. 2010; Vol. 1267, p 922.
2. Surface-Enhanced Raman Scattering of the CLPFFD-NH₂ peptide and two isomers. **Guerrero, A.R.**; Kogan, M. J.; Aroca, R. F. 14th European Conference on the Spectroscopy of Biomolecules, 2011, Coimbra, Portugal. Short oral presentation.
3. Plasmon-Enhanced Raman/Fluorescence Ratio with Shell-Isolated Silver Nanoparticles. **Guerrero, A. R.**; Zhang, Y.; Aroca, R. F. 7th International Symposium on Advanced Materials and Nanostructures. 2012, Sorocaba, Brazil. Poster presentation.
4. Plasmon-Enhanced Fluorescence of CdTe Quantum Dots with Shell-Isolated Nanoparticles. **Guerrero, A. R.**; Ramírez-Maureira, M.; Osorio-Román, I. O.; Goulet, P.

J. G. and Aroca, R. F. 96th Canadian Chemistry Conference and Exhibition. 2013, Québec, QC, Canada. Poster presentation.

Other Presentations:

- **Guerrero, A. R.;** Jarosz, A.; Aroca, R. F. Surface-Enhanced Raman Scattering of Amino Acids. Chemistry at the Mall 2009, Devonshire Mall, Windsor. Poster presentation.
- **Guerrero, A. R.;** Mohan, H.; Teo, G. Y.; Zhang, Y.; Aroca, R. F. SHINEF: Shell-Isolated Nanoparticle-Enhanced Fluorescence. Chemistry at the Mall 2012, Devonshire Mall, Windsor. Poster presentation.

Awards

- *Best Pharmacy student of the Chilean universities*, awarded by the College of Pharmacists of Chile on November 27, 2006.
- *Best Pharmacy student at the University of Chile*, awarded by the Faculty of Chemical and Pharmaceutical Sciences of the University of Chile on January 24, 2007.
- Tuition scholarship based on grades at the University of Windsor (2008-2013).
- Recipient of a *3M Canada Bursary Award* for first year graduate students in 2009.
- *Outstanding Graduate Student – Award for Excellence in Research, Scholarship and Creative Activity*, awarded by the University of Windsor on February 6, 2012.